PFC/RR-83-5 DOE/ET-51013-68

High Field Tokamaks With DD-DT Operation and Reduced Tritium Breeding Requirements

E. Bobrov, L. Bromberg, D.R. Cohn,
N. Diatchenko, R.J. LeClaire, J.E. Meyer
and J.E.C. Williams

Plasma Fusion Center
Massachusetts Institute of Technology
Cambridge, MA 02139

High Field Tokamaks with DD-DT Operation and Reduced Tritium Breeding Requirements

E. Bobrov, L. Bromberg, D.R. Cohn, N. Diatchenko,

R.J. LeClaire, J.E. Meyer and J.E.C. Williams

Plasma Fusion Center

Massachusetts Institute of Technology

Cambridge, MA 02139

High Field Tokamaks with DD-DT Operation and Reduced Tritium Breeding Requirements

E. Bobrov, L. Bromberg, D.R. Cohn, N. Diatchenko,
R.J. LeClaire, J.E. Meyer and J.E.C. Williams

Plasma Fusion Center
Massachusetts Institute of Technology
Cambridge, MA 02139

Table of Contents

LIST OF FIGURES

CHAPTER 2

CHAPTER 3

CHAPTER 4

CHAPTER 5

CHAPTER 7

CHAPTER 8

LIST OF TABLES

CHAPTER 1

CHAPTER 3

CHAPTER 4

CHAPTER 5

CHAPTER 6

CHAPTER 7

CHAPTER 8

INTRODUCTION AND SUMMARY

1.0 Introduction

The potential of the high field tokamak for production of very high values of $n\tau$ and fusion power density makes possible DD-DT operation which can be used to reduce tritium breeding requirements. In DD-DT operation, neutrons from both the D(T,n)He_4 and D(D,n)He_3 reactions are used to produce the tritium. The plasma tritium breeding requirement γ where

$$\gamma = \frac{\text{rate of fused tritons from external source}}{\text{rate of fusion neutron production}}$$

is between zero (DD operation) and one (DT operation). The tritium/deuterium ratio (n_T/n_D) in the plasma is < 1 (DT operation) but greater than that in DD operation where tritium produced by the D(D,p)T reaction is burned ($n_T/n_D \approx 0.003$). A continuous range of tradeoffs between reduced tritium breeding requirements and reduced fusion power density together with increased $n\tau_e$ requirements, is possible[1].

The advantages of DD-DT operation include:

- Insurance of self sufficiency in tritium production
- Increased flexibility of blanket and first wall design due to decreased neutron economy requirements
- High tritium burn-up in the plasma

- Increased availability of neutrons for fissile fuel breeding, tritium production for makeup or startup fuel for DT reactors and synfuel production

In this report we discuss trade-offs between breeding and plasma performance and present illustrative design features for two types of high field tokamaks which use DD-DT operation. One device is a relatively near term machine of moderate size (major radius = 4.8 m, minor radius = 1.2 m). It would serve as an engineering/materials test reactor with self sufficiency in tritium production[2,3]. We refer to this device as an *Advanced Fusion Test Reactor* (*AFTR*) device. An *AFTR* device might also be used to produce tritium for other reactors or to produce fissile fuel.

The second device is a larger machine (major radius = 9.6 m, minor radius = 2.4 m) which would use superconducting magnets. It is a commercial reactor which would produce electricity using blankets which are optimized for considerations other than neutron economy. We refer to this device as an *Advanced Fuel Commercial Reactor* (*AFCR*). *AFCR* might also be used to produce excess tritium. Another possible application is synfuel production.

1.1 Tradeoffs Between Breeding and Plasma Performance Requirements

An important tradeoff between neutronics and plasma performance requirements can be expressed in terms of the dependence of $n\tau_E$ required for ignition upon $1 - \gamma$. We refer to $1 - \gamma$ as the "plasma tritium breeding margin" since it represents the difference between the required breeding ratio for DT plasma operation and that for plasma operation in a DD-DT mode.

Using the empirical scaling $\tau_E \sim na^2$ for the electron energy confinement time, $n\tau_E \sim n^2a^2 \sim \beta^2B^4a^2$ where β is the ratio of plasma pressure to magnetic field pressure, a is the minor radius and B is the magnetic field on axis[4]. Figure 1.1 shows the dependence of $\beta^2B^4a^2$ required for ignition upon $1-\gamma$. $\beta^2B^4a^2$ is given in terms of meter^2-Tesla^4. At each value of $1-\gamma$ the plasma temperature is chosen to give the lowest value of $\beta^2B^4a^2$. Parabolic temperature and density profiles are assumed. For DT operation, $\beta^2B^4a^2 = 1.3$ m^{2}T^4 for a central ion temperature of 12 keV. It is assumed that all of the tritium produced in the D(D,p)T reactions is burned and that none of the He_3 produced in the D(D,n)He_3 reactions is burned.

It can be seen from Figure 1.1 that the $n\tau_E$ requirement for ignition increases strongly with $1 - \gamma$. Thus if most of the advantages of DD-DT operation can be realized at low values of $1 - \gamma$, operation at higher values of $1 - \gamma$ can be disadvantageous.

In DD-DT more than 50% of the neutrons are 14.1 MeV neutrons. When $\gamma = 0$ (DD operation), half ther neutron are 2.45 MeV neutrons produced by the D(D,n)He_3 reaction and half are 14.1 MeV neutrons produced by the D(T,n)He_4

reaction which burns the tritium produced by the D(D,p)T reaction. For $\gamma > 0$, additional 14.1 MeV neutrons are produced by burn up of the tritium which is provided externally. For $1 - \gamma \simeq 0.3$, 70% of the fusion neutrons are 14.1 MeV neutrons. The 14.1 MeV neutrons are more effective than the 2.45 MeV neutrons for the purpose of breeding tritium.

1.2 Advanced Fusion Test Reactor (*AFTR*) Device

The *AFTR* device utilizes water cooled, copper toroidal field (TF) magnets of Bitter construction. The advantages of quasi continuous Bitter plate magnet construction includes:

- Capability of high field operation using presently available technology
- Substantial reduction in resistive power losses due to maximization of conductor area
- Minimization of ripple by flexibility of choice of conductor geometry around a port
- Longer magnet insulation life (stresses are mainly compressive; planar insulators can be used)

Figure 1.2 shows normalized values of the stored energy in the toroidal field *TF* coil, the resistive power for the magnet, the fusion power and the plasma performance as functions of $1-\gamma$ for *AFTR*-type Reactors. A constant neutron wall loading of $P_{wall} = 4$ MW/m^2 is assumed. The size and stored energy increase strongly with increasing value of the plasma tritium breeding margin, $1-\gamma$.

Table 1.1 gives the main parameters of the illustrative *AFTR* device. With a field on axis of 8.5T the resistive power requirement of the TF magnet is 600 MW. The 0.36 m thick inboard blanket should provide sufficient shielding of the magnet insulation to allow for > 3 years of integrated operation. This assumption of insulator lifetime is based upon recent results of irradiated polyimides which indicate that fluences of $10^{24} - 10^{25}$ n/m^2 may be possible[5].

As shown in the table, $1-\gamma$ can be increased at the expense of decreased fusion power and Q_p ($Q_p =$ fusion power/auxilary heating power) for fixed beta, magnetic field and size. A value of $1-\gamma = 0.16$ can be obtained at ignition ($Q_p = \infty$). $1-\gamma = 0.25$ can be obtained with $Q_p = 20$.

Table 1.2 shows operating characteristics of the *AFTR* device at a reduced field of 6.6T. The resistive power requirement of the TF magnet is 350 MW.

Figure 1.3 shows an elevation view of the plate design that would be used in the *AFTR* device.

The *AFTR* device would serve as an engineering/materials test reactor of moderate size which would be self sufficient in tritium production because of its substantial plasma tritium breeding margin and also would produce some electrical power. It might also be used to produce tritium or be used for fissile fuel breeding.

The nonelectrical applications capability of *AFTR* device is illustrated in Table 1.3. Operation at a toroidal field of 6.6T and $1-\gamma = 0.1$ is assumed. A $LiAlO_2$ blanket with a Zr_5Pb_3 multiplier is used. The overall tritium breeding margin (TBM) $= k - \gamma$ where k is the blanket breeding factor; $k = M\eta$ where M is the blanket neutron multiplication factor and η is the blanket breeding efficiency ($\eta =$ no. of tritons/neutron absorbed in the blanket). For $M = 1.2$ and $\eta = 0.9$, $TBM = 0.18$. The number of excess neutrons is given by the product of TBM and the fusion neutron generation rate. The 4.5×10^{19} excess neutrons generated per second could be used to generate 7.2 kg of excess tritium per year at 100% availability.

Figure 1.4 shows R_n/P_{res}, the ratio between the rate of production of excess neutrons R_n and the resistive power needed to drive the reactor P_{res} as a function of $1-\gamma$. It is assumed that the neutron wall loading and the main stresses of the toroidal field system are kept fixed. It can be seen that there are advantages in operating with increasing values of $1-\gamma$, in terms of larger neutron generation rate per unit power dissipated in the magnet system, although the reactor size increases.

If some form of non-inductive current drive were not used on the *AFTR* device, its pulse length would be limited to $\sim$ 100 s by the drive of the ohmic heating transformer.

For $1-\gamma = 0.1$, the ratio of fusion power to TF magnet power would be ~ 1 for a value of average beta of ~ 0.06 and a magnetic field on axis of 6.6 T. Even if power producing blankets were used in *AFTR* device it would still consume a substantial amount of electricity. Hence the capability the *AFTR* device would provide in terms of tritium breeding margin and self sufficiency in tritium production comes at a substantial price. If higher values of β could be achieved the attractiveness of the *AFTR* device would, of course, increase.

1.3 Advanced Fusion Commercial Reactor (*AFCR*) Device

The use of superconducting toroidal field magnets removes the problem of a large resistive power requirement. However, a device with superconducting magnets will be substantially larger (due to increased magnet shielding requirements) and will have significantly higher capital cost. Furthermore, whereas the technology for resistive toroidal field magnets is presently available, a substantial amount of time is necessary to develop reliable large, high field superconducting magnets. Because of the high cost and increased time for implementation, a superconducting DD-DT device would best serve as a demonstration or commercial reactor.

Table 1.4 gives parameters for an illustrative Advanced Fueld Commercial Reactor (*AFCR*) device. The parameters for the *AFCR* device have been extrapolated from the HFCTR design[6].

This *AFCR* device would operate with $1-\gamma = 0.20$ at ignition. The fusion power would be 3100 MW and the neutron wall loading would be 2.2 MW/m^2. Table 1.5 shows the dependence of the fusion power, the wall loading and the plasma Q as functions of the plasma tritium breeding margin $1-\gamma$. Figure 1.5 shows an elevation view of the *AFCR* device.

The *AFCR* device uses niobium tin toroidal field magnets. The field at the magnet is 11.9 T. The superconducting magnets would be in separate dewars and could be individually removed. The tokamak would be completely modularized. Each module would consist of two TF magnets, blanket and shield and first wall.

The TF magnets do not touch each other in the throat of the tokamak.

A bucking cylinder is used to support the inward force. The load from the cold structure in TF magnets would be transferred to the warm structure by G-10 struts. Calculations of the heat leak through the struts indicate that it is sufficiently low.

At $1-\gamma = 0.20$ the plasma is operated at an average temperature of 15 keV. At this temperature the OH transformer has sufficient voltsecond capability to provide pulse lengths ≥ 1 hour.

Figure 1.6 shows normalized values of the stored energy in the toroidal field *TF* coil, the fusion power, the plasma major radius and the plasma performance as functions of $1-\gamma$ for *AFCR* -type Reactors. A constant neutron wall loading of 2.2 MW/m^2 is assumed. The size and fusion power of the reactor increase with increasing value of the plasma tritium breeding margin, $1-\gamma$.

If *AFCR* is operated as an electricity producing reactor, $LiAlO_2$ would be used for the tritium breeding blanket. $LiAlO_2$ has potential safety advantages relative to liquid breeding materials and could be superior to LiO_2 and other solid breeding materials in terms of chemical release, tritium holdup, allowed temperature range for operation, and compatibility with structure and coolant. A major disadvantage of using $LiAlO_2$ in DT reactors (a marginal tritium breeding ratio even with a neutron multiplier) is removed by DD-DT operation with $1-\gamma = 0.20$. Without a neutron multiplier, a $LiAlO_2$ blanket should be self-sufficient in tritium if operated with $1-\gamma = 0.2$.

An additional possibility would be to use a Zr_5Pb_3 multiplier, leading to a large overall tritium breeding margin. With this larger margin the need for a blanket in the inboard region would be removed. Another possibility is to use the substantial overall breeding margin to produce excess tritium which could be used for start up or make up fuel for DT reactors with a blanket breeding ratios less than one. Table 1.6 shows how *AFCR* device could be used to produce excess tritium. 47 kg of excess tritium can be generated per year with 100% availability if the space surrounding the plasma is completely utilized.

Figure 1.7 shows R_n/E_{TF}, the ratio between the rate of production of excess neutrons R_n and the stored energy in the toroidal field magnet E_{TF} as a function of $1 - \gamma$ for *AFCR* type devices.

The substantial tritium breeding margin might also facilitate use of this device for synfuel production, since the absorption of neutrons in high temperature blankets could be accommodated.

1.4 Conclusions

High field tokamaks with average betas of ~ 0.06 and sizes not very much larger than DT reactors can be operated in the DD-DT mode with substantial reductions in tritium breeding requirements. Operation with plasma tritium breeding margins $(1-\gamma)$ in the range of 0.1 to 0.3 could lead to significant advantages in blanket design and to a substantial increase in the availability of neutrons for excess tritium production. The increased availability of neutrons could also be used to increase fissile fuel production and to facilitate synfuel blanket design.

The benefits from operation at high values of $1-\gamma$ (> 0.4) may in general be outweighed by increases in machine size for average betas which are less than 0.06.

An *AFTR* device with resistive magnets could serve as a relatively near term engineering/materials test reactor which would obtain tritium self sufficiency at a relatively early stage in fusion power development. This device might also be used for tritium production.

A device with superconducting magnets, illustrated by the *AFCR* design, could be used for commercial electricity production with substantial tritium breeding margin $(1-\gamma = 0.20)$. The major radius of the *AFCR* device (R = 9.6 m) is not significantly larger than that of contemporary DT reactor designs. Furthermore, the *AFCR* device has the capability of producing pulse lengths $\geq$ 1 hour with the OH transformer. By going to somewhat larger values of major radius it should be possible to obtain substantially longer pulses. The *AFCR* device design thus illustrates the potential of tokamak as a commercial reactor with reduced blanket requirements and very long pulse lengths.

REFERENCES

1. Greenspan, E., Blue, T. and Miley, G.H., *Proceedings of the Fourth Topical Meeting on the Technology of Controlled Nuclear Fusion*, King of Prussia, Pa. (1981).

2. Cohn, D.R., Bromberg, L., Williams, J.E.C., Becker, H., LeClaire, R. and Yang, T., *Proceedings of the Third Technical Committee Meeting and Workshop on Fusion Reactor Design and Technology*, Tokyo, Japan, October (1981).

3. Bromberg, L., Cohn, D.R., Williams, J.E.C., Becker, H., LeClaire, R. and Yang, T., *Proceedings of 9th Symposium on Engineering Problems of Fusion Research*, Chicago, Illinois, October, 1981.

4. Cohn, D.R., Parker, R.R. and Jassby, D.L., Nucl. Fusion **16** (1976) 31; Jassby, D.L., Cohn, D.R. and Parker, R.R., Nucl. Fusion **16** (1976) 1045.

5. Becker, H., MIT Plasma Fusion Center, private communication

4. Cohn, D.R., Schultz, J.H., et al., *High Field Compact Tokamak Reactor (HFCTR) Conceptual Design*, MIT Plasma Fusion Center Research Report RR-79-2 (January 1979)

TABLE 1.1
MAIN PARAMETERS OF ADVANCED FUSION TEST REACTOR (*AFTR*) DEVICE
FULL PERFORMANCE

Major radius (m)		4.8		
Minor radius (m)		1.2		
Elongation (b/a)		1.5		
Average beta		0.062		
Magnetic field at plasma axis (T)		8.5		
$\beta^2 B^4 a^2$ ($\mathrm{m}^2\ \mathrm{T}^4$)		28		
Power requirement of resistive TF magnet (MW)		600		
Inboard blanket/shield thickness (m)		0.36		
Outboard blanket/shield thickness (m)		0.66		
$1-\gamma$	0.07	0.16	0.25	1
Fusion Power (MW)	2840	1200	750	160
Neutron Wall Loading ($\mathrm{MW/m^2}$)	8	4.2	2.7	0.6
Q_p	∞	∞	20	1

TABLE 1.2

PERFORMANCE OF ADVANCED FUSION TEST REACTOR (*AFTR*) DEVICE

REDUCED FIELD

Magnetic Field at Plasma Axis (T)	6.6		
$\beta^2 B^4 a^2$ (m^2 T^4)	10		
Power Requirement of Resistive TF Magnet (MW)	360		
$1-\gamma$	0.1	0.27	0.58
Fusion Power (MW)	650	260	110
Neutron Wall Loading (MW/m^2)	2.3	0.9	0.4
Q_p	50	3	1

TABLE 1.3

TRITIUM PRODUCTION IN ADVANCED FUSION TEST REACTOR (*AFTR*) DEVICE

(LITHIUM ALUMINATE BLANKET WITH Zr_5Pb_3 MULTIPLIER)

Magnetic Field at Plasma Axis (T)	6.6
Power Requirement of Resistive TF Magnet (MW)	360
$1-\gamma$	0.1
Fusion Power (MW)	650
M	1.2
η	0.9
k	1.08
Tritium Breeding Margin (k - γ)	0.18
Excess Neutrons (n/s)	4.5×10^{19}
Net Tritium Production (100% Availability) (kg/yr)	7.2

TABLE 1.4

MAIN PARAMETERS OF ADVANCED FUEL COMMERCIAL REACTOR (*AFCR*) DEVICE

Major Radius (m)	9.6
Minor Radius (m)	2.4
Magnetic Field at Plasma Axis (T)	7.0
Plasma Elongation	1.5
Magnetic Field at TF Magnet (T)	11.9
Superconductor	Nb_3Sn
Average Beta	0.063
$\beta^2 B^4 a^2$ (m^2 T^4)	55.5

TABLE 1.5

DD-DT TRADEOFFS FOR ADVANCED FUEL COMMERCIAL REACTOR ($AFCR$) DEVICE

$1 - \gamma$	Fusion Power (GW)	Neutron Wall Loading (MW/M^2)	Q_p
0.0 (DT)	40.7	29.1	∞
0.10	5.9	4.3	∞
0.20	3.1	2.2	∞
0.35	1.8	1.3	10.0
0.75	0.72	0.5	2.0
1 (DD)	0.50	0.36	1.25

TABLE 1.6

TRITIUM PRODUCTION IN ADVANCED FUEL COMMERCIAL REACTOR (*AFCR*) DEVICE (LITHIUM ALUMINATE BLANKET WITH Zr_5Pb_3 MULTIPLIER)

Fusion Power (MW)	3100
M	1.2
η	0.9
k	1.08
Tritium Breeding Margin ($k - \gamma$)	0.28
Excess Neutrons (n/s)	3.1×10^{20}
Excess Tritium Generation (at 100% Availability) (kg/yr)	47

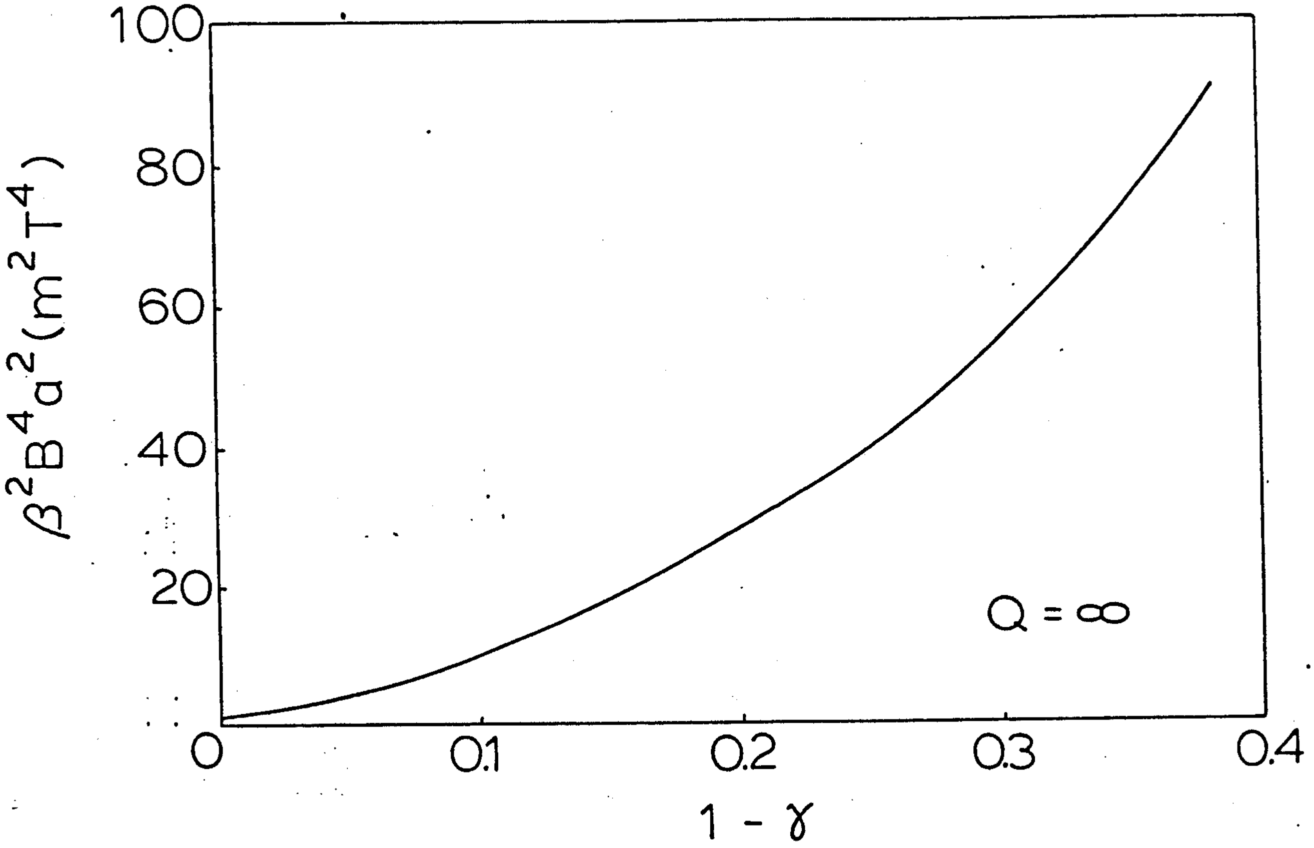

Figure 1.1 Plasma Performance Parameter $P = \beta^2 a^2 B^4$ at Ignition as a Function of the Plasma Tritium Breeding Margin, $1 - \gamma$. Using the empirical scaling $\tau_e \sim na^2$ for the electron energy confinement time, $n\tau_e \sim \beta^2 B^4 a^2$.

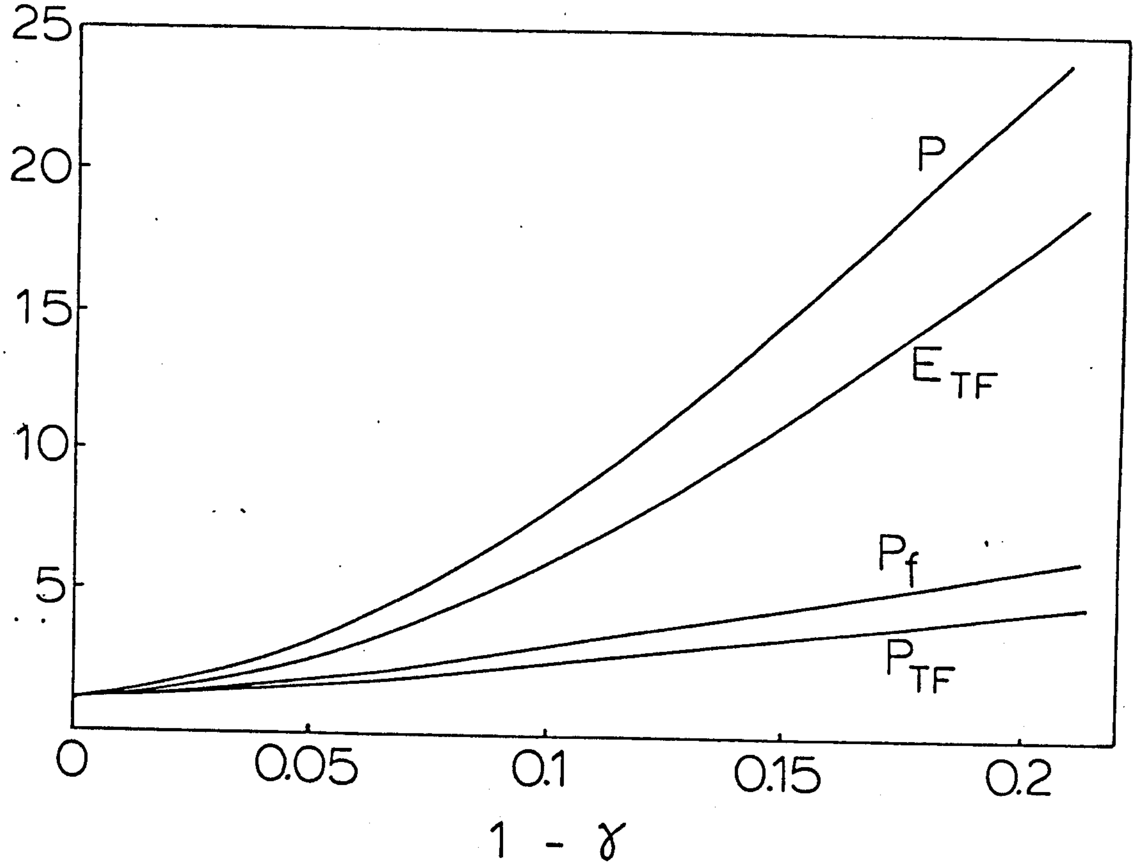

Figure 1.2 Trade-offs for *AFTR* devices. Dependence upon $1 - \gamma$ of normalized values of plasma performance $P = \beta^2 a^2 B^4$; stored energy in TF magnet, E_{TF}; resistive power requirement of TF magnet, P_{res}; and fusion power P_f. A constant neutron wall loading of 4 MW/m^2 is assumed.

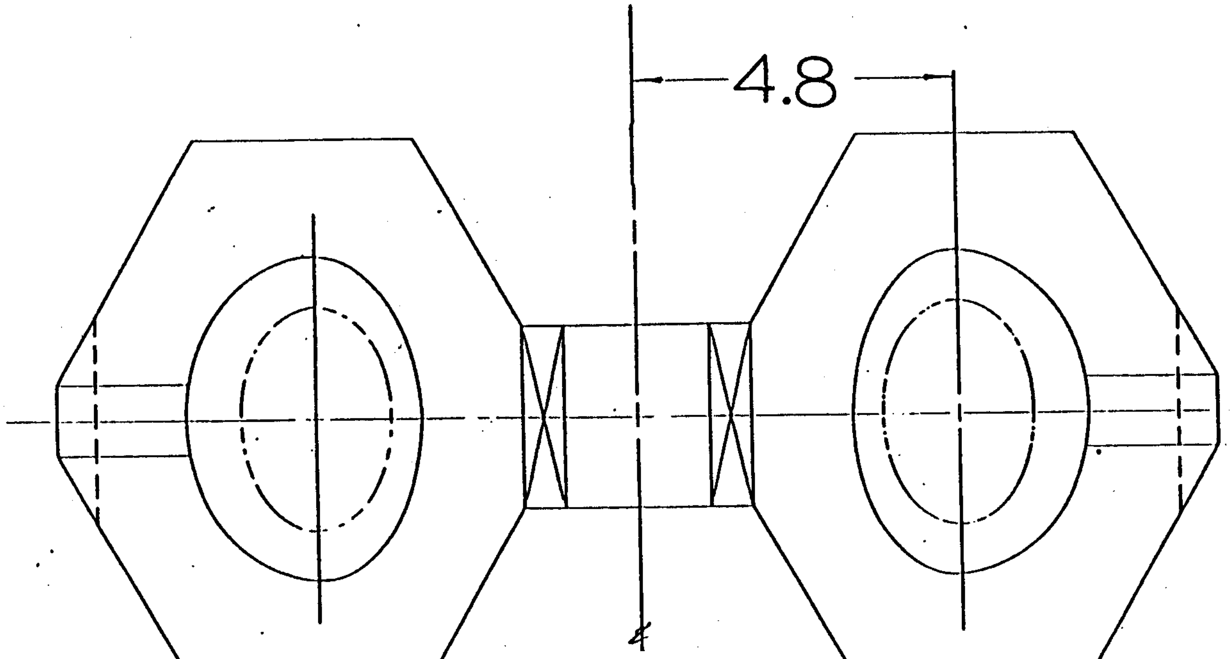

Figure 1.3 Elevation view of *AFTR* device

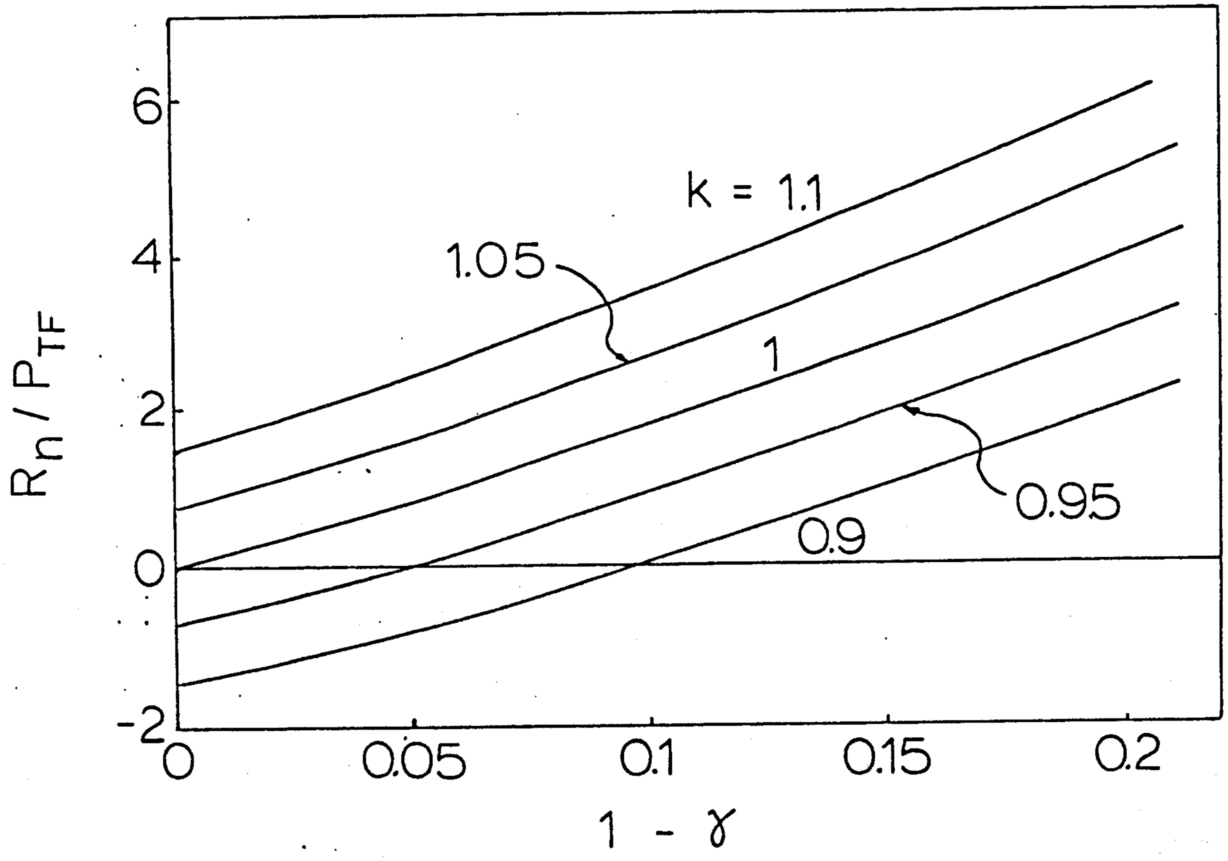

Figure 1.4 Ratio between Excess Neutron Generation Rate and Resistive Power Dissipated in TF Coil as Function of $1-\gamma$ for *AFTR* type devices. k is the Effective Tritium Breeding Ratio.

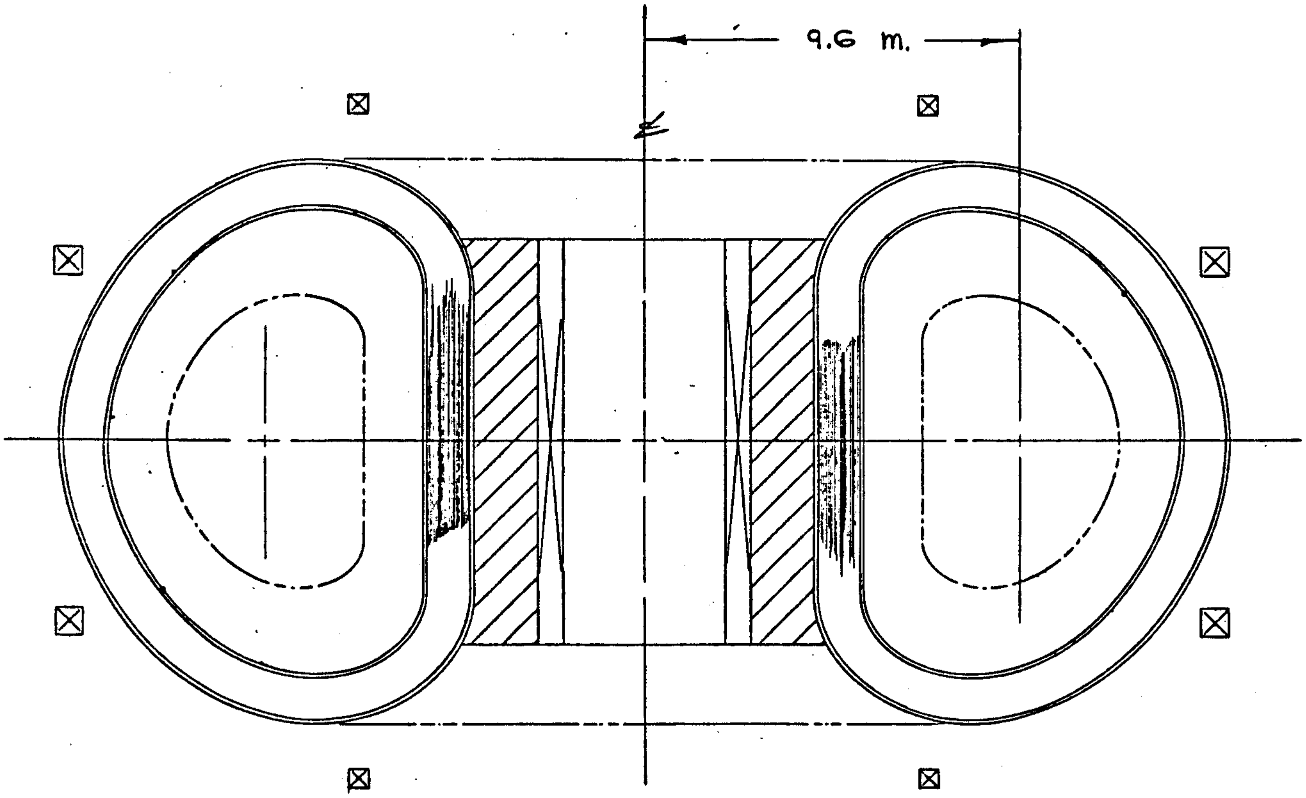

Figure 1.5 Elevation View of *AFCR* Device.

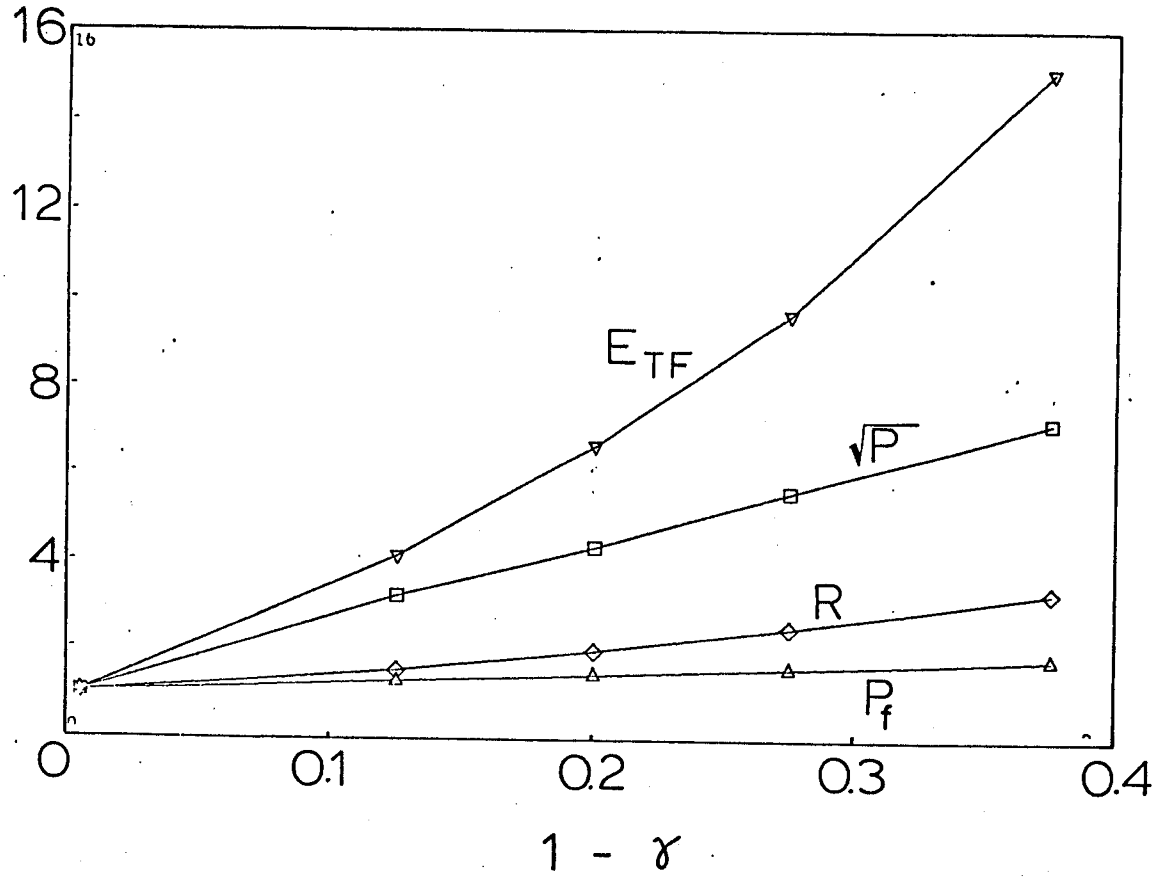

Figure 1.6 Trade-offs for *AFCR* devices. Dependence upon $1 - \gamma$ of normalized values of plasma performance $P = \beta^2 a^2 B^4$; stored energy in TF magnet, E_{TF}; major radius, R; and fusion power P_f. A constant neutron wall loading of 2.2 MW/m^2 is assumed.

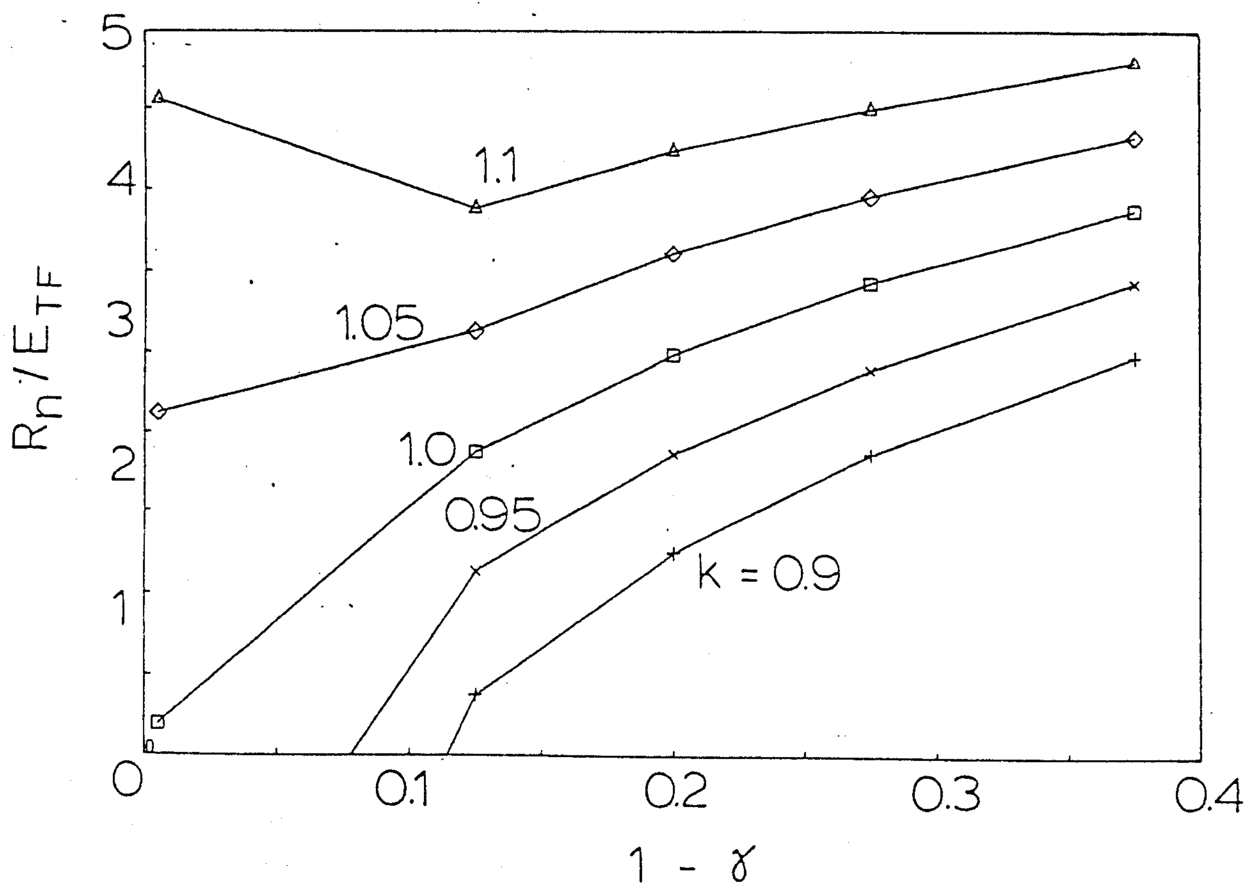

Figure 1.7 Ratio between Excess Neutron Generation Rate and Stored Energy in the Toroidal Field Magnet as Function of $1 - \gamma$ for *AFCR* type devices. k is the Effective Tritium Breeding Ratio.

2 DD-DT OPERATION

DD-DT operation refers to the fuel cycle which lies between the deuterium-tritium (DT) and semi-catalyzed deuterium (SCD) cycles in terms of the amount of external tritium required [1,2]. The DT cycle is at one extreme of the range of operation involving the DD and DT reactions, requiring all of the tritium burnt in the plasma to be supplied externally. This cycle has the smallest plasma requirements in terms of $n\tau$ where n is the plasma density and τ the energy confinement time, operating temperature, plasma pressure at ignition and also achieves the largest fusion power density. In SCD operation, the tritium to deuterium ratio, n_t/n_d, is determined by the balance of tritium production from the D(D,p)T reaction and consumption by the D(T,n)He_4 reaction; where the He_3 produced in the reaction D(D,n)He_3 is assumed to leave the plasma before it is burned. Thus, no external tritium need be supplied in SCD operation.

Although the DT fuel cycle is considered to be the first that will be utilized in commercial fusion applications, the stringent tritium breeding requirement sufficiently complicates design in terms of blankets, safety, and maintenance, to at least partially offset the advantages of improved power density and confinement characteristics compared to SCD. SCD, at the other end of the spectrum, appears attractive from the point of view of the lack of a tritium breeding requirement, at the price of a significantly reduced power density, increased ignition requirements, and higher required operating temperature — on the order of 50 keV [2]. The essence of the DD-DT option is to operate between these two bounds, supplying a fraction of the tritium needed in the DT cycle but with a higher power density and easier confinement than that available from SCD.

In the DD-DT cycle, some tritium is supplied to the plasma externally so that n_t/n_d is greater than the equilibrium value in SCD but is less than one. This amount of tritium is determined by the paramater γ, representing the ratio of tritium from the external source to the number of DT and DD fusion neutrons. Thus, gamma ranges from 1 for DT operation to 0 for SCD operation.

This range of trade-offs available from DD-DT operation between plasma performance and tritium breeding can be significant in the development of fusion systems for a number of reasons:

- DD-DT operation could help to insure that the first generation of fusion reactors are self sufficient in tritium production.
- Since the requirements on neutron economy are reduced, the design of the blanket/shield can be more readily optimized to satisfy criteria such as safety, low activation, low tritium inventory, ease of maintenance, and reduced size.
- DD-DT operation could be used to produce make-up fuel for fusion reactors that have a tritium breeding ratio less than one.
- Low values of n_t/n_d result in an increased tritium burn-up fraction.
- The availability of neutrons for non-electrical applications such as fissile fuel breeding and synfuel production can be significantly increased. It may be possible to obtain very high thermal support ratios for

fissile fuel breeding applications. (Thermal support ratio is the power produced by the supported fission reactors minus fusion reactor power consumption, all divided by the fusion reactor thermal power production.)

In this chapter, the plasma properties required for operation in DD-DT mode are described. In section 2.2, the optimum temprature for operation in DD-DT mode is obtain. Both fusion power density and ignition criteria are considered.

In section 2.3, the plasma requirements for operation in DD-DT mode are studied as a function of $1-\gamma$, that is the plasma tritium breeding margin. In the first section, the plasma performance P is held constant and the fusion power P_f and wall loading P_{wall} are allowed to vary. This corresponds fixing a machine and allowing to vary the fusion power as the fuel mixture is varied. In section 2.3.2, the parameter $P_{wall} \times a$ is kept fixed, and the required plasma performance (which is related, for a given β scaling, to the machine parameters) is allowed to vary. This corresponds in practice to varying the machine dimensions. A more complete study where the wall loading is kept fixed requires information about the machine dimensions and is delayed until chapters 4 and 7.

Finally, in section 2.4 the advantages of usin DD-DT for neutron applications are described.

2.1 Parametric Analysis

In order to make an assessment of the DD-DT fuel cycle, a parametric survey was performed for operating temperature, performance (defined as $\beta^2 a^2 B^4$), and various system powers, versus the range of plasma tritium breeding ratio γ between 0 (SCD) and 1 (DT). Values of gamma were calculated on the basis of a given ratio of tritium to deuterium concentration, n_t/n_d, using the following balance equation for the relative reaction rates:

$$\frac{1}{2}{n_d}^2\langle\sigma_{dd}v\rangle_p + \gamma\left(\frac{{n_d}^2}{2}\langle\sigma_{dd}v\rangle_n + n_d n_t\langle\sigma_{dt}v\rangle\right) = n_d n_t\langle\sigma_{dt}v\rangle \qquad (1)$$

which describes the equilibrium tritium balance where $\langle\sigma_{dt}v\rangle$ is the reaction parameter averaged over the velocity distribution for the DT reaction and $\langle\sigma_{dd}v\rangle_p$ and $\langle\sigma_{dd}v\rangle_n$ are the associated reaction parameters for the DD tritium branch and DD proton branch, respectively. γ represents the overall external tritium requirement per neutron reaction

$$\gamma = \frac{\text{rate of fused tritons from external source}}{\text{rate of fusion neutron production}}$$

Equation (1) is the equilibrium condition for tritons in the plasma. The left hand side represents the source of tritons and the right hand side represents the burn-up rate of the tritons. Then

$$\gamma = \frac{\frac{n_t}{n_d}\langle\sigma_{dt}v\rangle - \frac{1}{2}\langle\sigma_{dd}v\rangle_p}{\frac{1}{2}\langle\sigma_{dd}v\rangle_n + \frac{n_t}{n_d}\langle\sigma_{dt}v\rangle}$$

Therefore, the value of γ is determined by the ratio n_t/n_d and the plasma temperature.

At equilibrium, the electron and ion temperature are derived from electron energy and ion balance equations,

$$\frac{1}{2}\frac{dn_eT_{io}}{dt} = -\frac{1}{2}\frac{n_iT_{io}}{\tau_i} - \frac{3}{5}\frac{n_e(T_{io}-T_e)}{\tau_{ei}} + W_i \tag{2}$$

and

$$\frac{1}{2}\frac{dn_eT_e}{dt} = -\frac{1}{2}\frac{n_eT_e}{\tau_e} + \frac{3}{5}\frac{n_e(T_{io}-T_e)}{\tau_{ei}} + W_e - P_{br} - P_{cycl} \tag{3}$$

where T_e and T_{io} are the electron and ion temperatures, τ_e and τ_i are the electron and ion energy confinement times, n_e is the electron density and $n_i = n_t + n_d$. Parabolic electron and ion density and temperature profiles have been assumed. W_e and W_i represent the electron and ion heating rates by the charged fusion products. W_i and W_e are calculated using the results of reference [3]. P_{cycl} represents the energy losses due to cyclotron emission.

It is assumed that the energy confinement time for the different ions is the same, and that the different ion species are at the same temperature.

It is assumed that τ_e is determined by the empirical scaling law [4]

$$\tau_e = 1.9 \times 10^{-21} n_e a^2$$

where τ_e is in s, n_e is in m^{-3} and a is the plasma minor radius in m. For the ions it is assumed that neoclassical transport governs their behavior. If this is the case, then for most of the parameter space of interest in this report $\tau_i >> \tau_e$ and the main ion energy loss channel is through energy transfer with colder electrons [5].

The region of interest, determined by γ (or alternatively by n_t/n_d), is further characterized in terms of the fusion power density and the plasma performance, $P = \beta^2 B^4 a^2$. Assuming empirical scaling for the electron energy confinement time, the performance parameter is written as:

$$P = \beta^2 a^2 B^4 \approx (n_e a)^2 \left(T_e + T_{io} \frac{n_i}{n_e} + \overline{E_{fp} n_{fp}} \right)^2$$
$$\approx (n_e \tau_e) \left(T_e + T_{io} \frac{n_i}{n_e} + \overline{E_{fp} n_{fp}} \right)^2$$

where β is the ratio of plasma pressure to magnetic field on axis pressure and B is the magnetic toroidal field. Note that the performance parameter is proportional to the $n\tau$ product and a function of the temperature. This proportionality holds for INTOR scaling. For other scalings, however, the proportionality may not hold. P, on the other hand, is a good figure of merit for machine sizing. This will be described in the next chapter.

The fusion power density can be written as:

$$P_f \sim \sum_{species} r n_k n_m \langle \sigma v \rangle_{k,m} E_{k,m}$$
$$\approx \frac{\beta^2 B^4}{\left(T_{io} + \frac{T_e n_e}{n_i} + \frac{\overline{E_{fp} n_{fp}}}{n_i} \right)^2} \sum_{species} r p_k p_m \langle \sigma v \rangle E_{km} \simeq \frac{P}{a^2} f(T, \gamma)$$

where $\langle \sigma v \rangle_{k,m}$ is the reaction parameter for the species k, m. E_{km} is the energy released per fusion reaction and $\overline{E_{fp} n_{fp}}$ is the contribution of the fast fusion products to the plasma preassure. $r = 0.5$ for like species ($k = m$) and $r = 1$ for unlike species ($k \neq m$).

$f(T,\gamma)$ is a function of the plasma temperature and of the plasma composition (which is related to γ). $f(T,\gamma)$ is a weak function of temperature, as $\frac{\langle\sigma v\rangle}{T_{io}^2} \approx T_{io}^{\alpha}$, with $\alpha \sim 0$ for DT and $\alpha \sim 1$ for DD. By introducing a specific machine geometry, thermal fusion power and wall loading are also written in terms of performance as:

$$P_{th} \sim PRf(T,\gamma)$$

and

$$P_{wall} \sim \frac{P}{a} f(T,\gamma)$$

Therefore, the parameters $P_{wall} \times a$ and P_{th}/R depend only on the parameter P, the temperature and the ion composition. This holds true irrespective of the scaling law assumed for the electron energy confinement. Therefore P is clearly related to fusion power and wall loading.

In summary, we are interested in a parametric survey of operating temperature, performance, and fusion power in the range of gammas for DD-DT operation from $\gamma = 1$ (DT) to $\gamma = 0$ (SCD). A performance parameter can be defined proportional to the fusion system powers, and for Alcator scaling, to the $n\tau$ product.

2.2 Operating temperature

The first step in the analysis was to determine the optimum ion temperature at which to operate the DD-DT cycle. This was accomplished by varying performance P and fusion power/R (fusion power divided by major radius) versus $1-\gamma$ for fixed temperature. Throughout the analysis the "tritium breeding margin", $TBM = 1 - \gamma$, was used to identify the particular DD-DT regime of interest. This quantity represents the fraction of excess neutrons available for uses other than tritium breeding, assuming the bred tritium is perfectly recirculated, and that the effective tritium breeding ratio of the blanket k is 1.

Figure 2.2.1 shows the plasma performance versus tritium breeding margin for temperatures ranging from 10 to 30 keV. Each constant temperature curve represents the performance required to achieve a range of breeding margins at ignition at that temperature. Thus, it is desirable to operate at the temperature that corresponds to the lowest required performances in the breeding margin range of interest. Note that between breeding margins of 0 and 0.3, this temperature is approximately $20 - 25$ keV. For breeding margins greater than $1 - \gamma > 0.3$, optimum temperatures increase to 30 keV.

Figure 2.2.2 shows the function $f(T,\gamma)$ vs. the tritium breeding margin $1-\gamma$. $f(T,\gamma) \approx P_{wall}/P$, or equivalently, $f(T,\gamma) \sim P_f R/P$. At low values of $1-\gamma$ $f(T,\gamma)$ has a weak dependence on temperature, but at the higher values of $1-\gamma$, $f(T,\gamma)$ is almost independent of T_{io}. The optimum temperature is that that minimizes P at ignition (figure 2.2.1). Temperatures of 20 keV and greater offer breeding margins in the range of interest with ignited plasma (assuming the *INTOR* empirical scaling law) [4,5]. Due to limitations in extrapolating present scaling laws to the larger temperatures and sizes required in this type of reactors, it is more important to use, as much as possible, the fusion power and wall loading constraints, and leave the ignition requirement as a secondary consideration.

The value of $\frac{P_f/R}{P}$ is maximized at $T_{io} \sim 10 - 15$ keV for $1 - \gamma \sim 0$ (DT operation). At higher values of $1 - \gamma$ the optimum temperature increases. The optimum temperature for SCD operation occurs at $T_{io} \sim 40$ keV.

A similar analysis was performed for driven operation at $Q = 5$. Figure 2.2.3 is the resulting figure for performance versus tritium breeding margin. As in the ignited case, the constant temperature curve at 20 keV requires the minimum performance for the range of breeding margins of interest ($\gamma < 0.35$). In fact, the range over which this is the case extends to breeding margins of 0.5, due to the lower performances required for driven operation.

On the basis of this analysis, 20 keV was chosen as the reference temperature for further analysis for both ignited and driven operation.

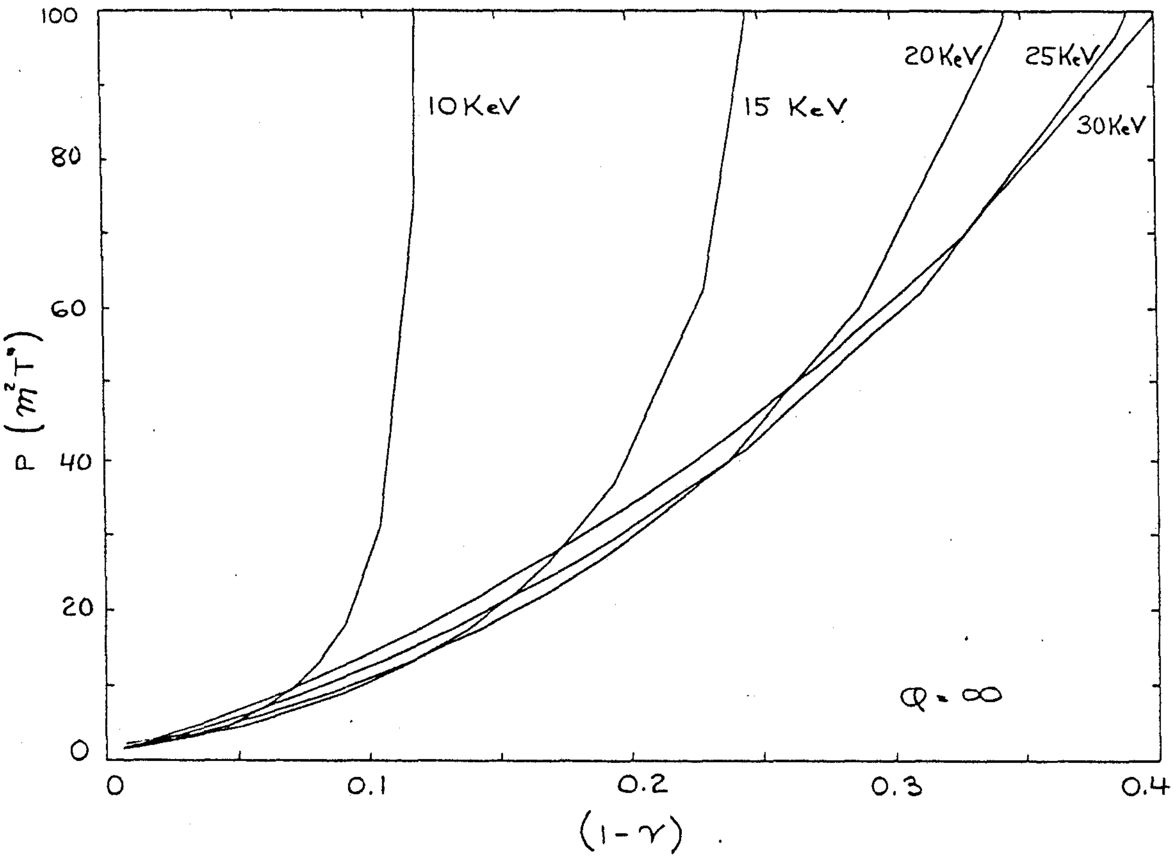

Figure 2.2.1 Performance at Fixed Central Ion Temperature (Ignited Using Empirical Scaling Law for the Electrons)

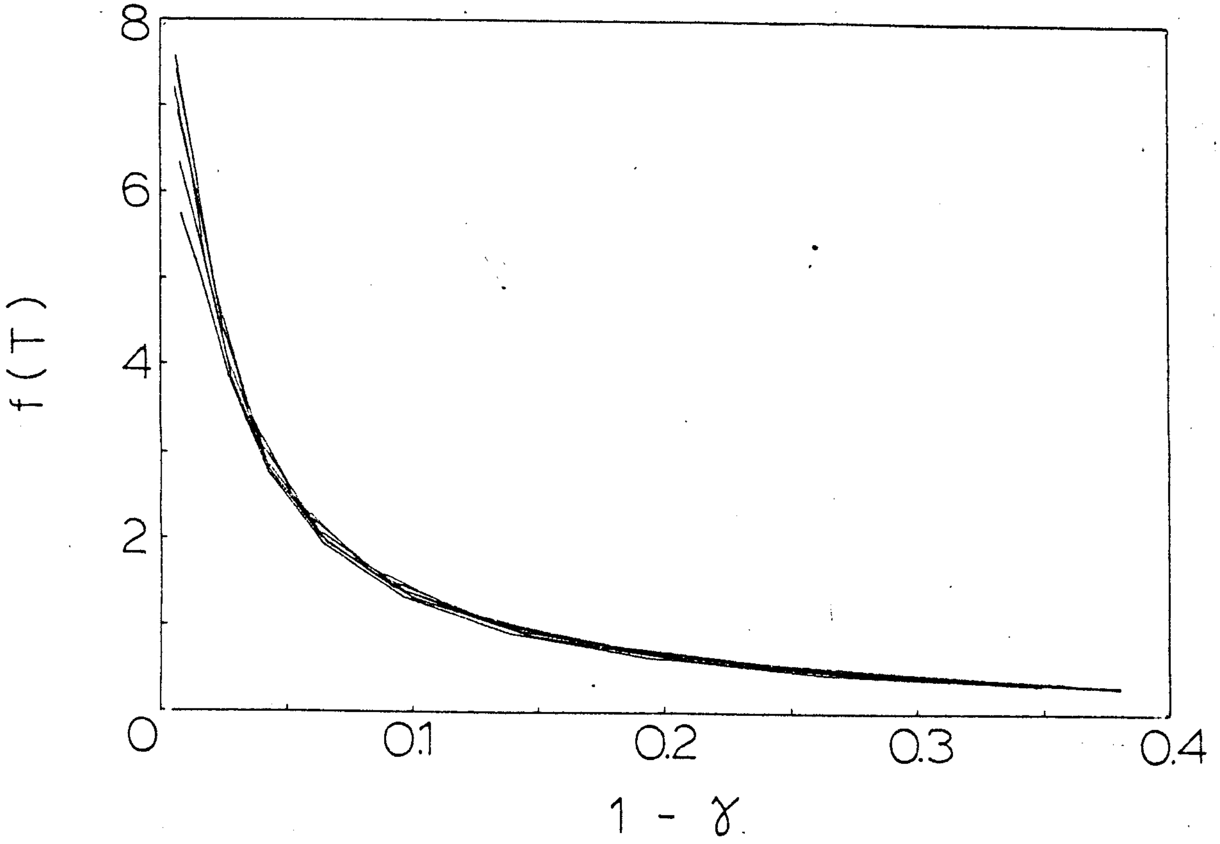

Figure 2.2.2 Fusion Power Normalized to Major Radius for Constant Temperature (Ignited Using Empirical Scaling Law for the Electrons)

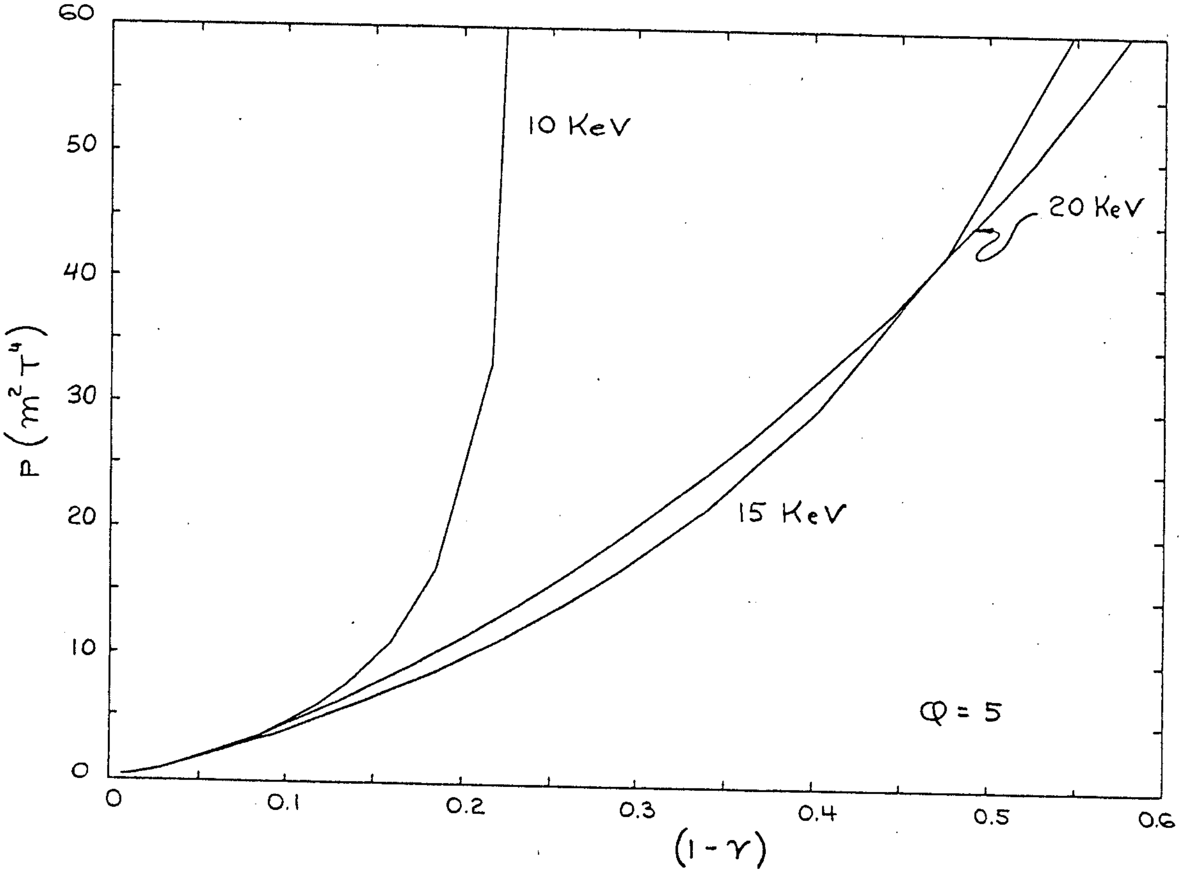

Figure 2.2.3 Performance at Fixed Central Ion Temperature for $Q = 5$.

2.3.1 Trade-offs For Fixed Performance

Operation with the DD-DT cycle has two major consequences. A decrease in the tritium required externally, and a decrease in the fusion power density relative to DT. Both of these issues must be addressed in a consistent manner in order for this mode of operation to be evaluated and possible regimes of operation identified. In this section, the fusion power density tradeoffs will be examined with the question of increased availability of neutrons being dealt with in a later section.

For constant temperature, the breeding margin possible is a direct function of the achievable performance. Figure 2.3.1 is a plot of performance versus breeding margin for the ignited case at $T_{io} = 20$ keV. Note, as suggested in the results of the previous section, that the needed performance for a given value of $1 - \gamma$ increases rapidly past a tritium breeding margin of 0.1. Curves of fusion power versus breeding margin for fixed P have been selected to analyze the trade-offs since performance can be expressed both in terms of fusion power density and specific machine design requirements (β, a and B^2). For example, if P were not held fixed, it would be possible to choose an operating regime based on fusion power trends that corresponds to a performance parameter beyond that possible in a given reactor. The wall loading on the other hand, is allowed to vary. In Section 2.1.3, the wall loading is held fixed and P is allowed to vary. Therefore, $P =$ constant relates to fixed machine size, while $P_{wall} =$ constant allows for varying machine dimensions.

Curves were generated for fixed perfomances of $P = 15$, 30, and 50 m^2 T^4 and for the geometries corresponding to the *AFTR* device ($R = 4.8$ m,

$a = 1.2$ m) and the *AFCR* superconducting version ($R = 9.6$ m, $a = 2.4$ m). Performance was held fixed by varying plasma Q (fusion power/auxilliary heating power) for subignited operation and increasing artificially the electron loss channel for the overignited cases. Throughout this analysis, curves with breeding margin as the abscissa will be used. It will be usefull to divide the curves into three segments:

Segment 1: $0.0 < 1 - \gamma < 0.1$
Segment 2: $0.1 < 1 - \gamma < 0.3$
Segment 3: $0.3 < 1 - \gamma < 1.0$

Figure 2.3.2 shows the fusion power density as a function of $1 - \gamma$ for the case $P = 30$ m^2 T^4 and $T_{io} = 20$ keV. Figure 2.3.3 shows the Q ratio between the fusion power to required auxiliary heating power as a function of $1 - \gamma$ for the same case as Figure 2.3.2. Figure 2.3.3 assumes empirical scaling for the electron energy confinement.

Some observations can be made regarding possible operating regimes with analysis of figures 2.3.2 and 2.3.3. In segment 1, the fusion power density decreases very rapidly, dropping by a factor of 6. For breeding margins in segment 2, fusion power density decreases more moderately, dropping by about 50 percent per 10 percent increase in breeding margin. In segment 3, a 10 percent increase in breeding margin brings only a 10 percent drop in fusion power density. For $P = 30$ m^2 T^4, $Q \sim \infty$ for $\gamma > 0.8$.

Such low tritium breeding margins brings up the question of how much margin is desired in terms of the increased availability of neutron and decreased breeding requirements. This will be dealt with in the Section 2.4. For the first half of segment 2 (Figure 2.3.2), the plasma remains ignited and the fusion power density decreases moderately. The remainder of segment two, $0.2 < 1-\gamma < 0.3$ has plasma Q dropping sharply. Finally, for segment 3, the fusion power density and plasma Q decreases gradually.

The cases corresponding to performances of 15 and 50 m^2T^4 exhibit the same trends as noted above. The major impact of increasing performance is an increase in the magnitude of the fusion power density and an increase in the range of breeding margins that are ignited. A plot of fusion power density P_f for P=50 m^2 T^4 (Figure 2.3.4) shows that the boundaries separating the segments described earlier occur in roughly the same spots. The net effect, then, is a widening of the breeding margin range in which the plasma is ignited.

Having identified these possible ranges of operation, based on the fusion power tradeoff, it remains to determine the tradeoff between an increase in available neutrons and decreasing fusion power density. This is done in Section 2.4.

2.3.2 Parametrics for Constant Wall Loading

In the previous section, P and the ignition criteria are held constant and the plasma composition is allowed to vary. As P is related to the machine parameters for a given β scaling with aspect ratio, ($P = \beta^2 a^2 B^4 \sim a^4 B^4/R^2$), keeping P fixed is equivalent to keeping the machine dimensions fixed. The fusion power and neutron wall loading, on the other hand, are decreasing rapidly with increasing values of $1 - \gamma$. From the reactor application point of view, however, it may be more important to keep the wall loading fixed; in this case, however, the machine dimensions are varying, and the scoping study has to allow for changes in machine parameters. In this section the tradeoffs between plasma physics requirements and plasma tritium breeding margin are performed for fixed $P_{wall} \times a$. In chapters 4 and 7 the wall loading P_{wall} is kept constant.

As derived in Section 2.1, $P_{wall} \sim P_f f(T,\gamma)/a$. Therefore, the product $P_{wall} \times a$ depends only on the plasma performance P, and on the plasma temperature and ion composition (that is, γ). The product $P_{wall} \times a$ is held constant in the parametric analysis described in this section.

It should be noted that the neutron wall loading P_{wall} is an important parameter in terms of the first wall, blanket and economics of the machine. The plasma performance P, on the other hand, is more relavant to ignition (for empirical or similar scaling laws) and machine requirements (and, therefore, cost).

The analysis is carried simularly as that in Section 2.3.1 with the difference that the plasma performance P is not held fixed. The value of γ is determined, and then the value of plasma Q that results in a given wall loading are calculated. There are cases in which the plasma would have to be overignited. In this case, a loss mechanism is introduced in the electron balance equation. It should be noted that in most cases the addition of the electron loss term does not alter the electron-ion temperature separation. This separation is determined from the ion energy balance, and thus it is not affected by electron loss. The plasma $n_e\tau_e$, however, is determined from the electron energy balance, and thus is affected by additional electron losses. It is assumed that the additional electron loss does not affect the other parameters as would be the case for radiative losses from high-Z impurities.

Figure 2.3.5 shows $n_e\tau_e$ as a function of the tritium breeding margin $1-\gamma$ for constant values of $P_{wall} \times a$. The ion temperature is assumed to be $T_{io} \sim 25$ keV, and is kept constant as $1-\gamma$ is varied. For $0 < \gamma < 0.4$, the optimum temperature of operation is $T_{io} \sim 20-25$ keV.

$n\tau_e$ increases strongly with $1-\gamma$. Thus, for a tritium breeding margin of $1-\gamma = 0.2$ and for $P_{wall} \times a = 4$ MW/m, the $n_e\tau_e$ required is a factor of 6 larger than the $n_e\tau_e$ required for DT operation at the same value of $P_{wall} \times a$. The scaling of $n_e\tau_e$ with $1-\gamma$ is approximately linear. It can be seen that because $n_e\tau_e \sim n^2$ (for INTOR scaling) and $P_f \sim n^2$, then $P_f \sim n\tau_e$ for constant value of γ.

Figure 2.3.6 shows P as a function of $1-\gamma$ for the cases of figure 2.3.5. It can be seen that in order to keep the wall loading constant, it is necessary to increase P as the regime of operation gets close to SCD due to reduction in specific power dimensions P_f/β^2B^2 as the operating regime approaches SCD. The curves for

P and $n_e\tau_e$ show the same general trends because the ion temperature is held constant.

Figure 2.3.7 shows Q as a function of $1-\gamma$ for the same cases as Figure 2.3.5. Empirical electron scaling law is assumed in Figure 2.3.7. The values of Q decreases with increasing values of the tritium breeding margin. For the case of $P_{wall} \times a = 4$ MW/m^2, the plasma is ignited for $1-\gamma < 0.25$. As seen in the previous section, there is a minimum value of P required for ignition. For low values of $P_{wall} \times a$, $P \sim P_{wall} \times a/f(T,\gamma)$ is lower than the minumum required for ignition. This conclusion holds true also for DT operation (the plasma Q is highest for this case: $\gamma = 1$ in figure 2.3.7). That is, for the empirical electron scaling law, the ignition requirement (at the optimal temperature) can be exressed as

$$(P_{wall} \times a)_{ignition} = 2.6\mathrm{MW/m}$$

Figure 2.3.8 shows the minimum value of $P_{wall} \times a$ for ignition at the optimum temperature as a function of $1-\gamma$. As $1-\gamma$ increases, the value of P required for ignition increases along with the value of $P_{wall} \times a$. For ignition with $1-\gamma = 0.2$, $P_{wall} \times a \sim 4$ MW/m.

The range of operation with constant wall loading is wide with the use of DD-DT. However, there are increased requirements (both in terms of decreased Q and/or increased plasma performance) as the operating point moves away from DT. The increased requirements result in larger machine sizes and increased cost. Chapters 4 and 7 deal with the changes in machine sizes for a resistive machine (*AFTR*) and a superconducting machine (*AFCR*) as the fuel mixture is changed for fixed wall loadings.

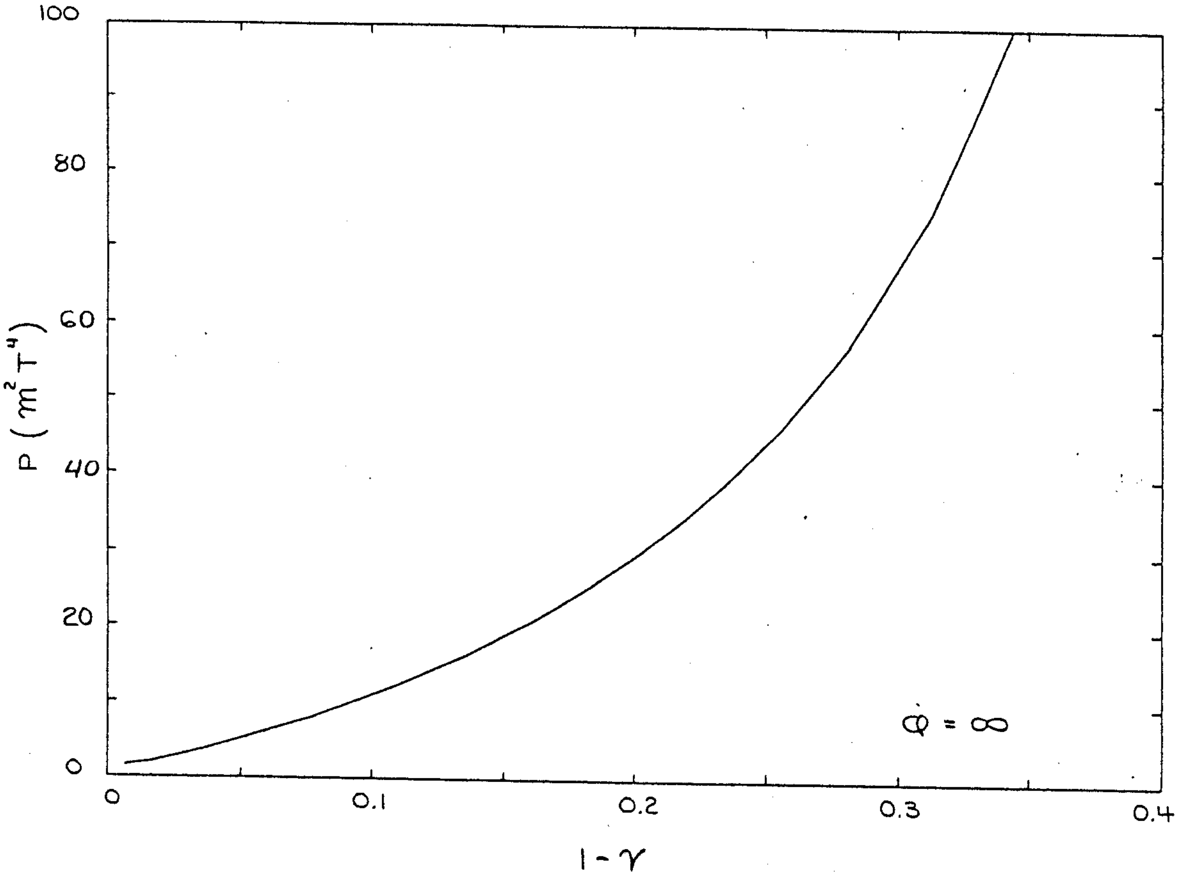

Figure 2.3.1 Performance vs Tritium Breeding Margin, Base Operation (Ignited, T_{io} = 20 keV).

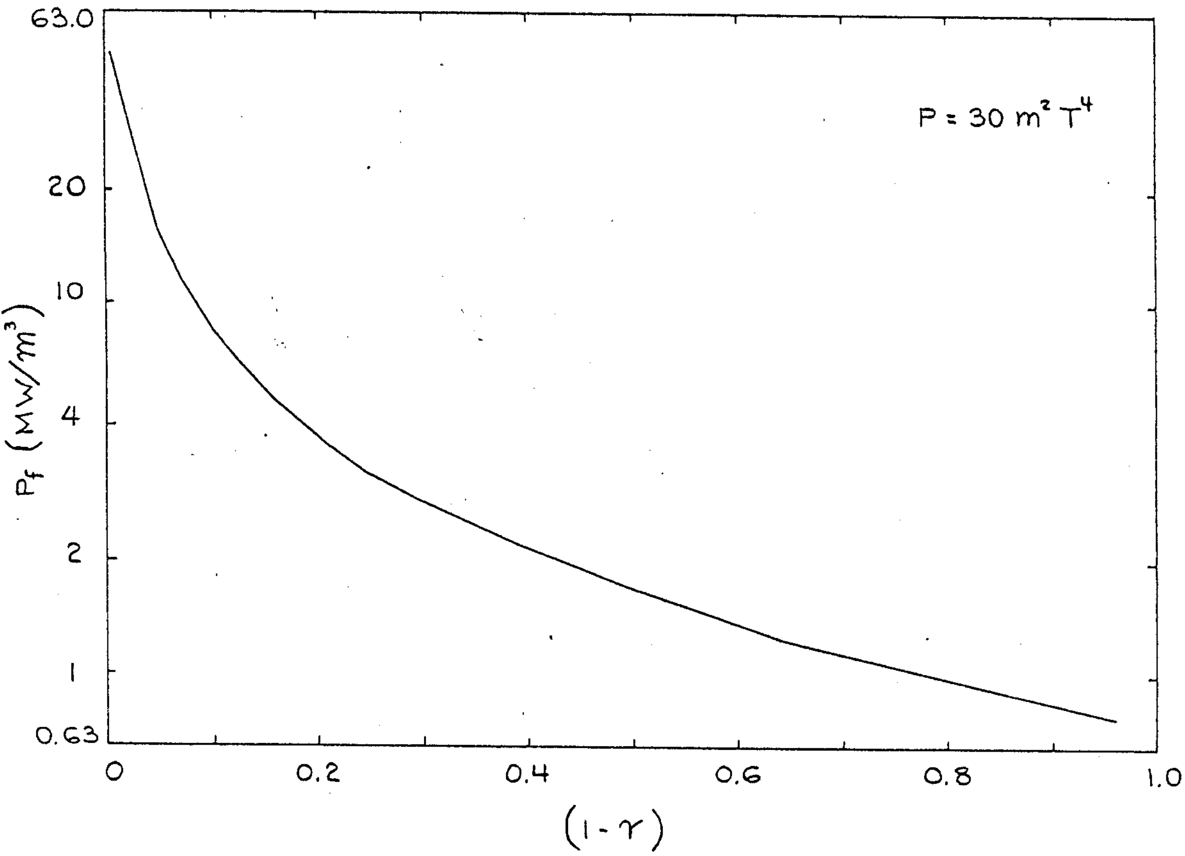

Figure 2.3.2 Fusion Power Density vs Tritium Breeding Margin ($P = 30$ m^2 T^4, $T_{io} = 20$ keV).

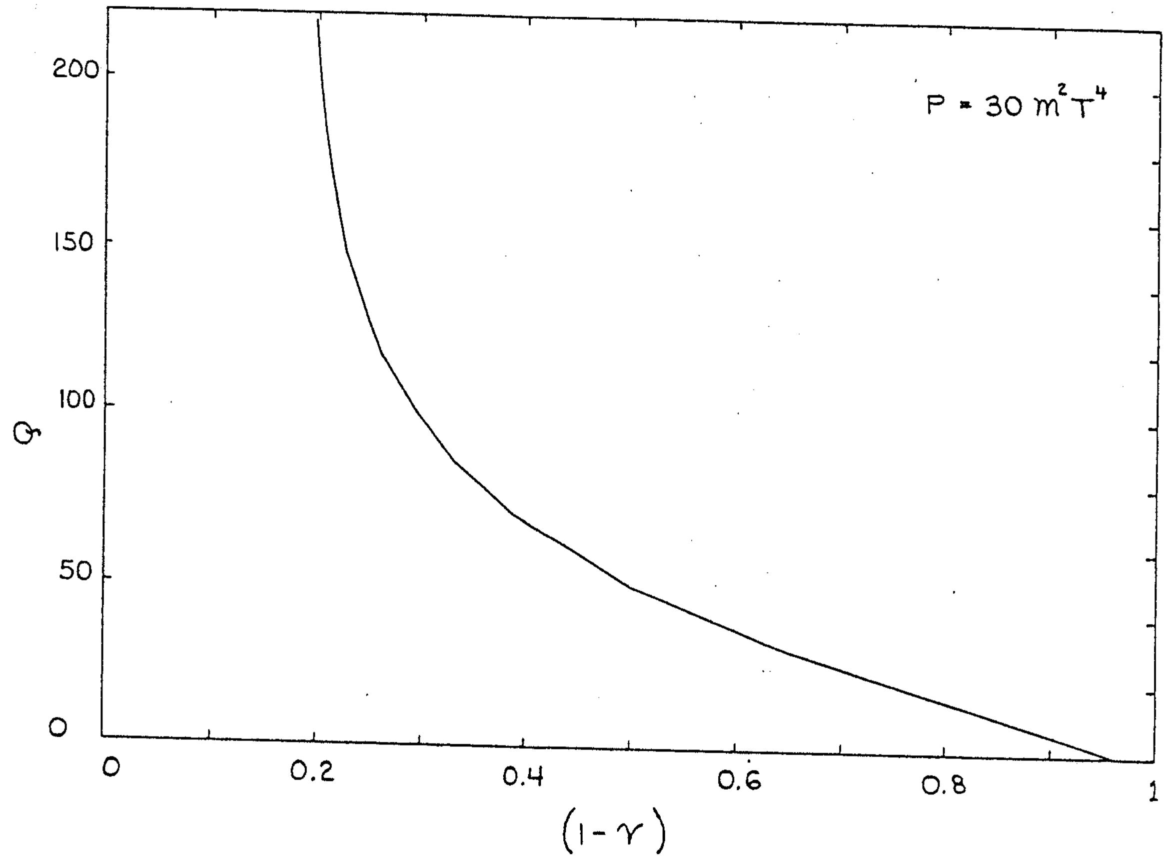

Figure 2.3.3 Q, Ratio of Fusion Power Density to Auxiliary Heating Power vs Tritium Breeding Margin, Base Operation ($P = 30\ \mathrm{m}^2\mathrm{T}^4$, $T_{io} = 20$ keV).

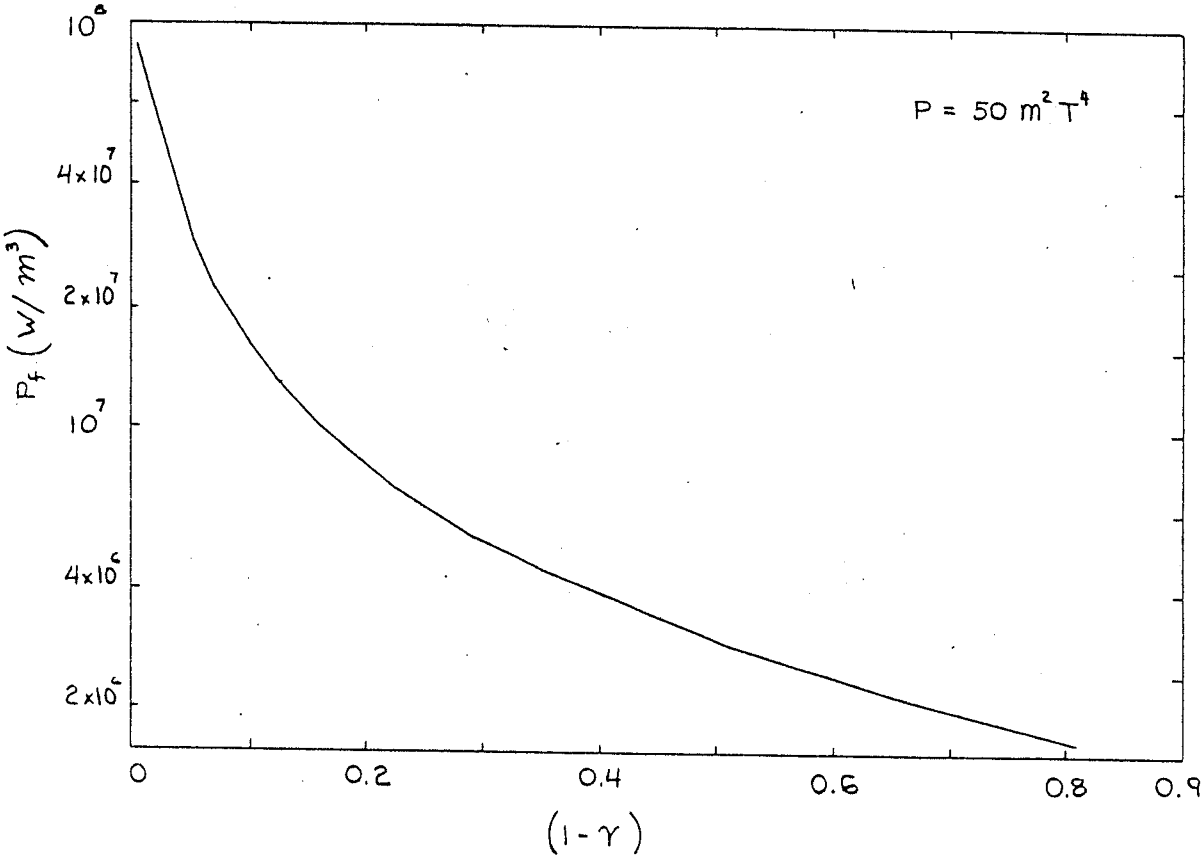

Figure 2.3.4 Fusion Power Density vs Tritium Breeding Margin ($P = 50$ m^2 T^4, $T_{io} = 20$ keV).

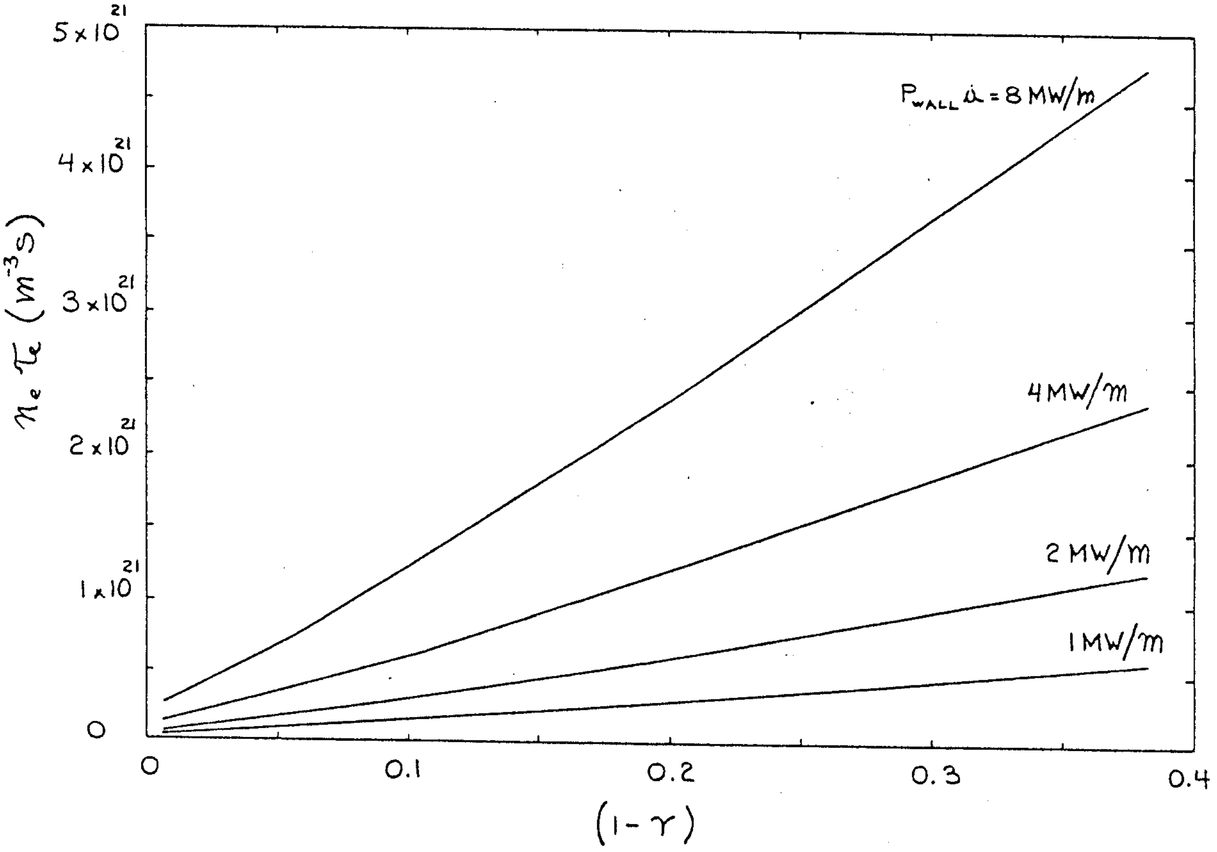

Figure 2.3.5 $n\tau_e$ for Constant $P_{wall} \times a$ Products vs Tritium Breeding Margin ($T_{io} = 25$ keV).

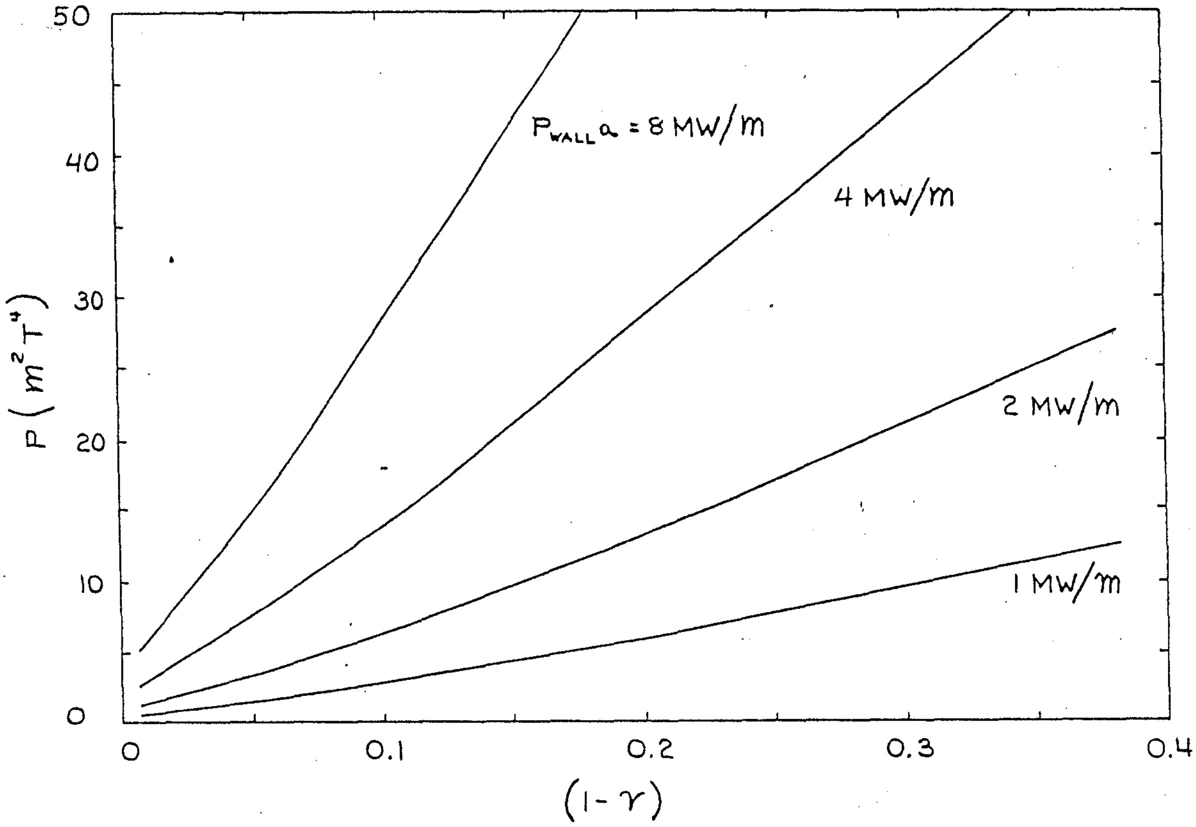

Figure 2.3.6 Plasma Performance P for Constant $P_{wall} \times a$ Products vs Tritium Breeding Margin ($T_{io} = 25$ keV).

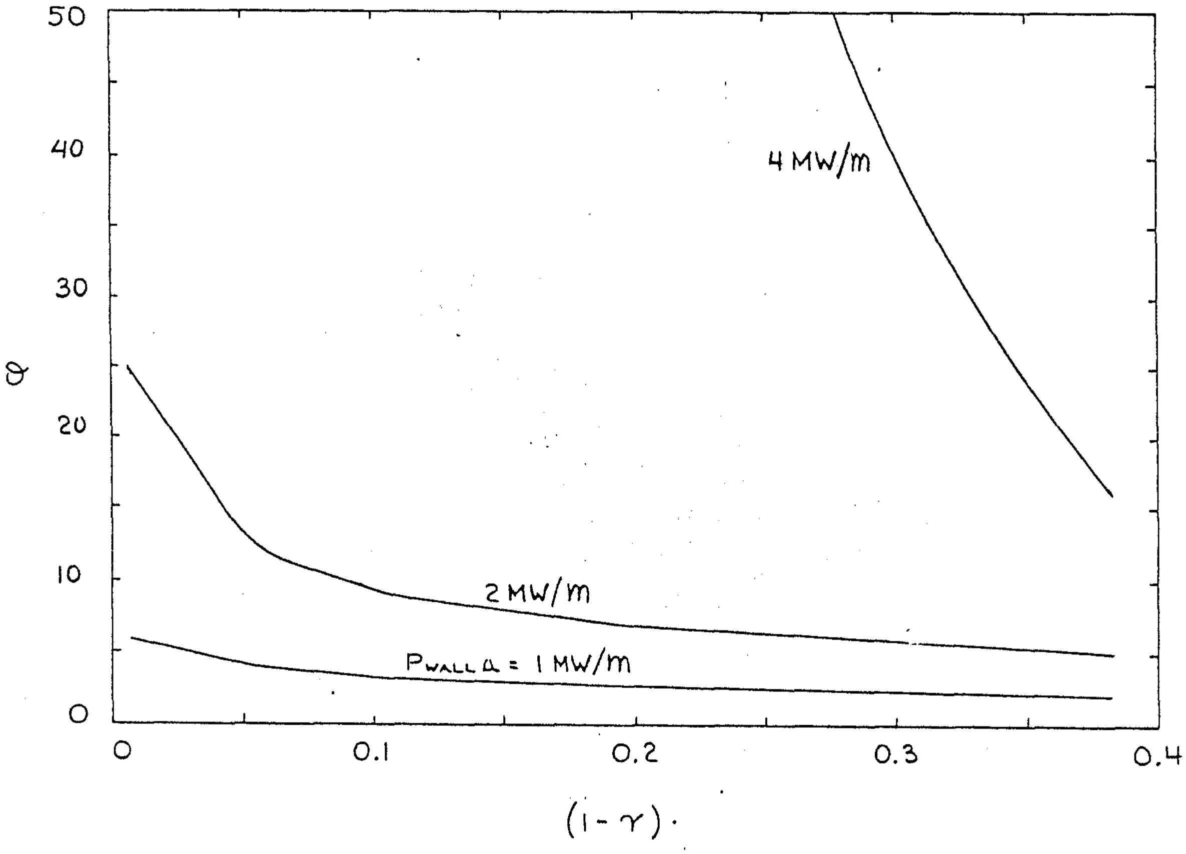

Figure 2.3.7 Ratio of Fusion Power to Auxiliary Heating Power Q for Constant $P_{wall} \times a$ Products vs Tritium Breeding Margin ($T_{io} = 25$ keV).

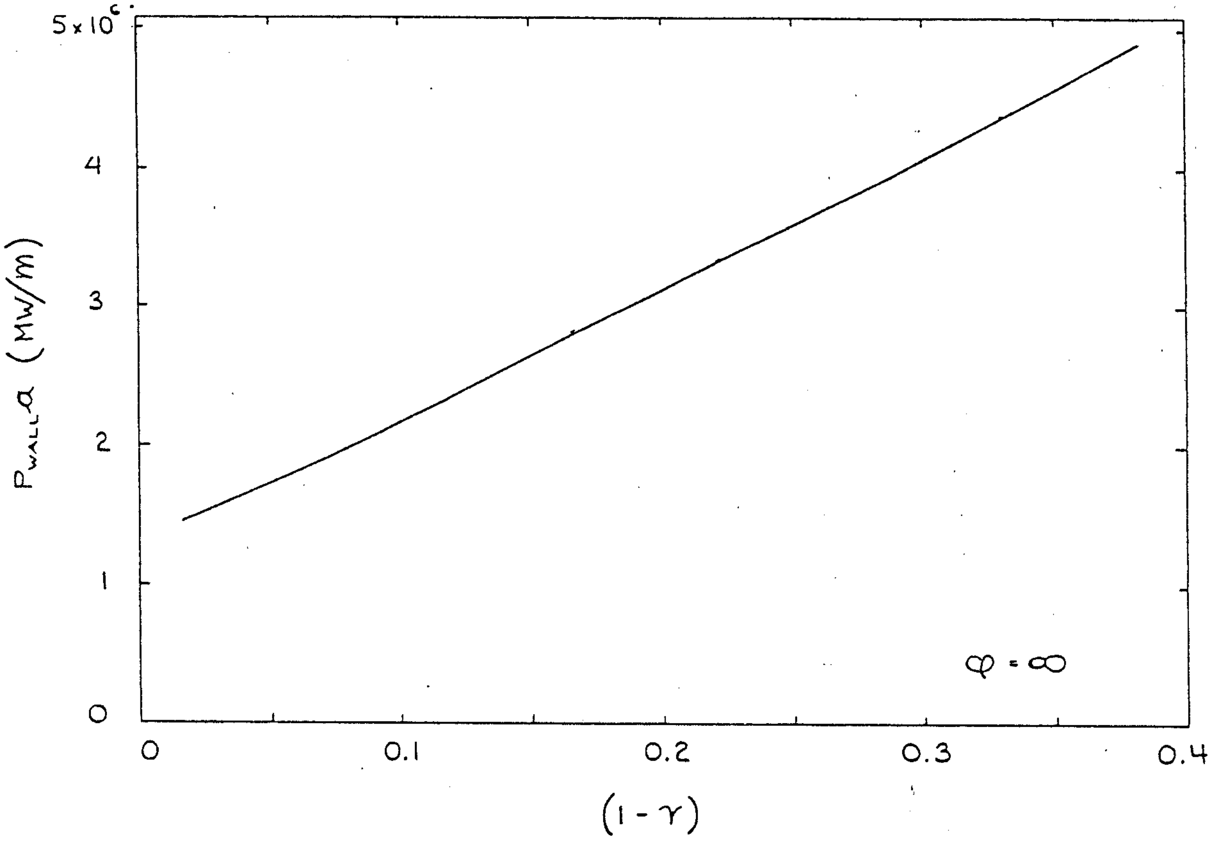

Figure 2.3.8 $P_{wall} \times a$ Product for Ignited Operation

2.4 Neutron Availability

Calculations were performed to determine the number of excess neutrons made available by operating in the regime with $\gamma < 1$. The benefit gained in a particular DD-DT region due to an increase in available neutrons must outweigh any penalties associated with the loss in fusion power density.

First, it will simplify the subsequent analysis to express the reaction rates in terms of γ. Let the DT, DD proton branch, and DD neutron branch reaction rates be specified by $R_{DT}, R_{DD,p}$ and $R_{DD,n}$ respectively. The DD proton branch, although not directly producing a neutron, produces energetic tritons. These tritons fuse with the deuterium background, yielding a 14 MeV neutron. The plasma tritium breeding is then:

$$\gamma = \frac{R_{DT} - R_{DD,p}}{R_{DT} + R_{DD,n}}$$

But, with $R_{DD,P} \approx R_{DD,n}$,

$$\gamma = \frac{R_{DT} - R_{DD,n}}{R_{DT} + R_{DD,n}}$$

or

$$R_{DD,n} = \frac{1-\gamma}{1+\gamma} R_{DT}$$

Using this expression we can find a simple expression for the fraction of 2.45 MeV (DD neutron branch) neutrons produced,

$$f_{2.45} \approx \frac{R_{DD,n}}{R_{DT} + R_{DD,n}}$$

then

$$f_{2.45} = \frac{1}{2}(1 - \gamma)$$

Thus, even at the far end of the DD-DT spectrum ($\gamma = 0, 1 - \gamma = 1$), half of the neutrons generated are still DT.

The total number of neutron production rate multiplied by the tritium breeding margin, designated "available excess neutrons", is plotted versus breeding margin in figure 2.4.1 for $P = 30$ m^2 T^4 and for an effective tritium breeding in the blanket of $k = 1.0$. Available excess neutrons is an indication of how many neutrons are available for uses other than to breed the tritium needed to sustain the plasma — assuming no loss of neutrons or tritium and no neutron multiplication. Note that the number of available neutrons increases rapidly in segment 1. Throughout segment 2 and up to a gamma of 0.4 in segment 3, there is a slight increase in available neutrons with little of no gain after $1 - \gamma \geq 0.4$.

This behavior is essentially what one would expect since the neutrons per second directly translate to fusion power, which is decreasing rapidly in this region and more gradually beyond. Some deviation from this behavior might be expected due to the fact that the average energy per fusion neutron in the plasma is decreasing for increasing breeding margin due to the larger DD component. However, in figure 2.4.2, the fraction of neutron power from the DT component is plotted versus breeding margin and this shows that even for $1 - \gamma \approx 0.85$, 88% of the neutron power is still derived from the DT component. Thus, there seems to be questionable gain in terms of the increased availability of neutrons past a breeding margin of 0.3 to 0.4 for $k = 1$ and with the assumptions for Figure 2.4.1.

The possible use of the DD-DT cycle for blankets with marginal tritium breeding ratios is illustrated next. First, note that the rate tritons are burned is R_{DT}. The rate at which externally supplied tritium is burnt in the plasma is $R_{DT} - R_{DD,P}$ while the rate at which fusion neutrons are produced is $R_T = (R_{DT} + R_{DD,n})$. Now the production rate for tritons is kR_T where k is the number of tritons in the blanket per fusion neutron generated in the plasma. Therefore, a quantity "Net Tritium Production Rate" (NTR) can be defined as;

$$NTR = (R_T + R_T)k - (R_{DT} - R_{DD,n}) =$$

$$= (k - \gamma)R_T$$

This quantity represents the rate of production of excess tritons made available for purposes other than fueling the DD-DT plasma, taking into account the tritium breeding ratio of the plant blanket system. NTR is plotted in figure 2.4.3. The case shown corresponds to $P = 30$ m^2 T^4 and shows several curves, each representing the net available neutrons for a given value of k. Note that for $k = 1$, the expression for NTR reduces to $(1 - \gamma)R_T$ and the corresponding curve in figure 2.4.3 corresponds to figure 2.4.1. As expected, for tritium breeding ratios k less than one, operation in DD-DT mode increases the effective breeding ratio and eventually produces an excess number of neutrons. For example, for a blanket with a $k = 0.9$, DD-DT can make the blanket self sufficient in tritium while operating at $1 - \gamma \geq 0.1$. From Table 2. we note that the penalty paid is a factor of six drop in the fusion power density.

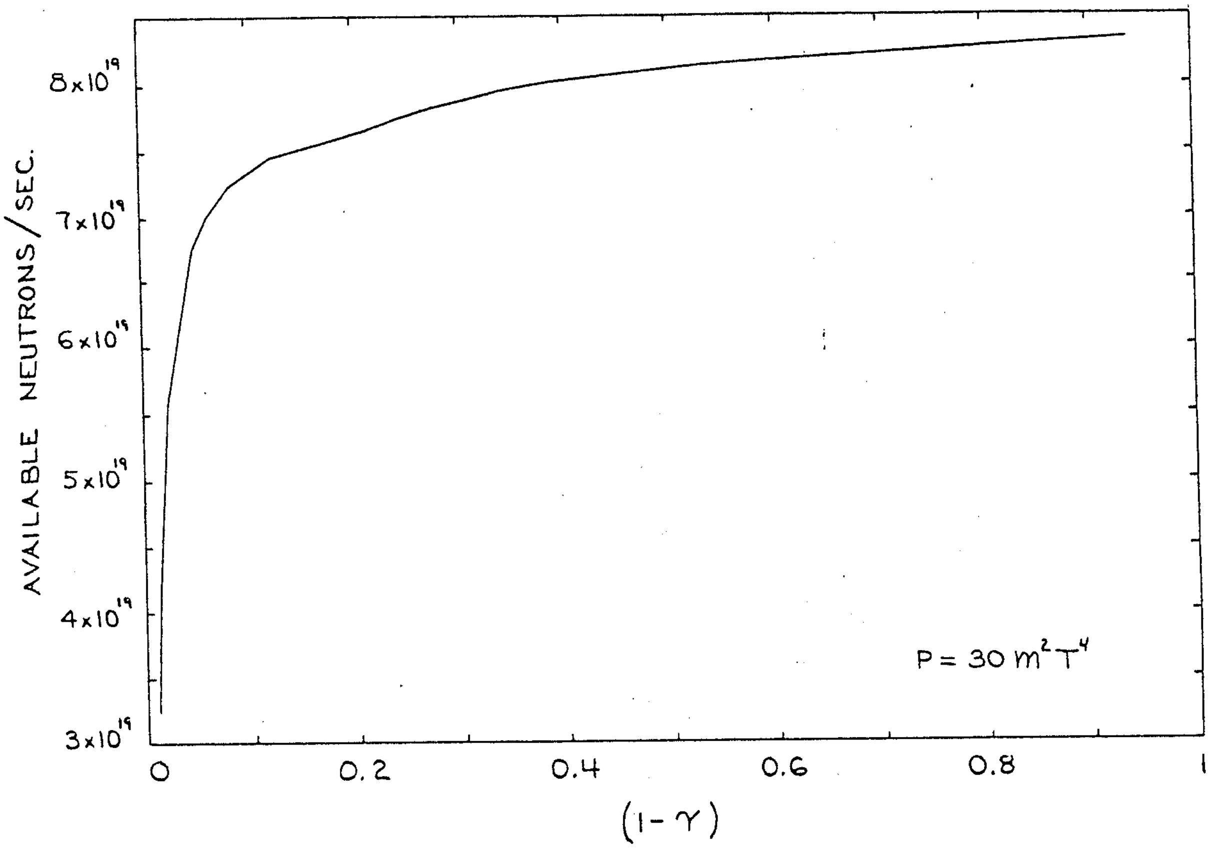

Figure 2.4.1 Available Neutrons versus Breeding Margin
(P = 30, T = 20 keV)

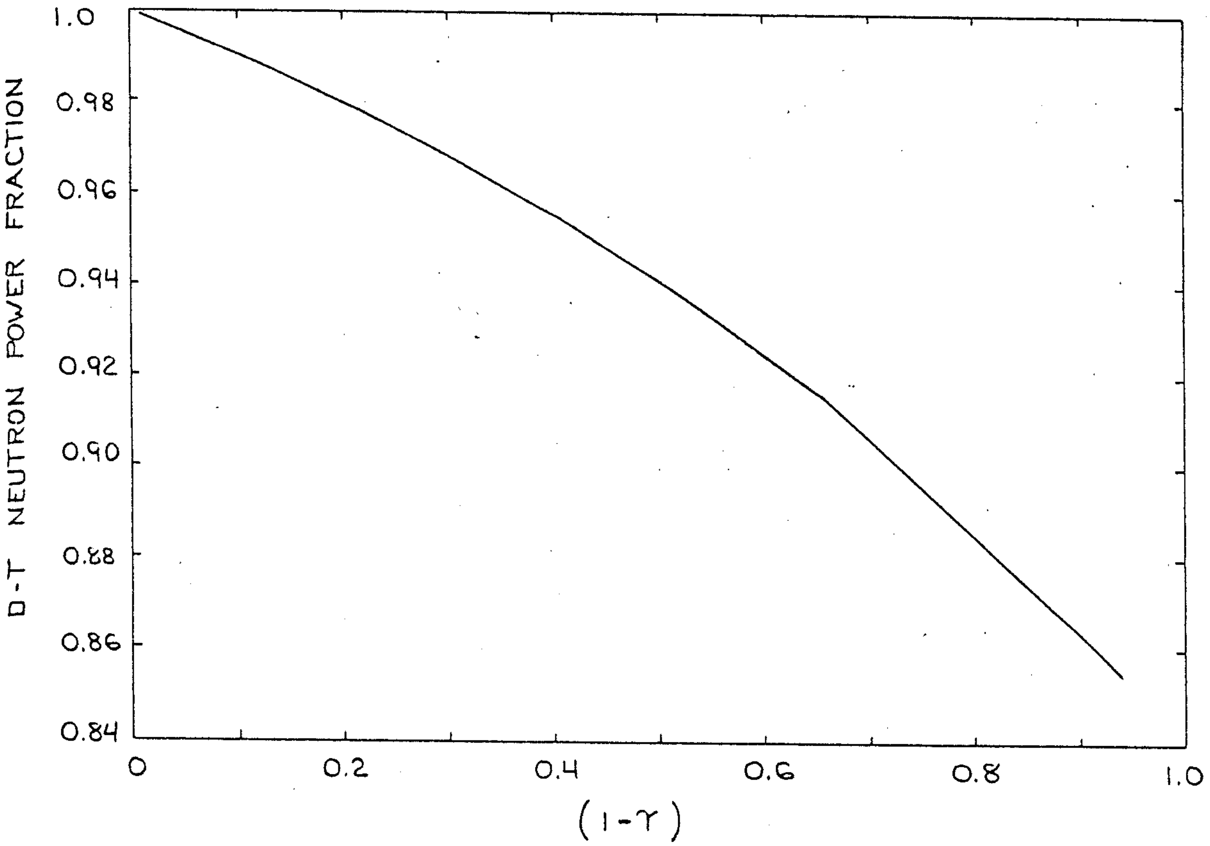

Figure 2.4.2 Fraction of Neutron Power Due to DT Reactions versus Tritium Breeding Margin ($P = 30$ m^{2}T^4, $T_{io} =$ 20 keV).

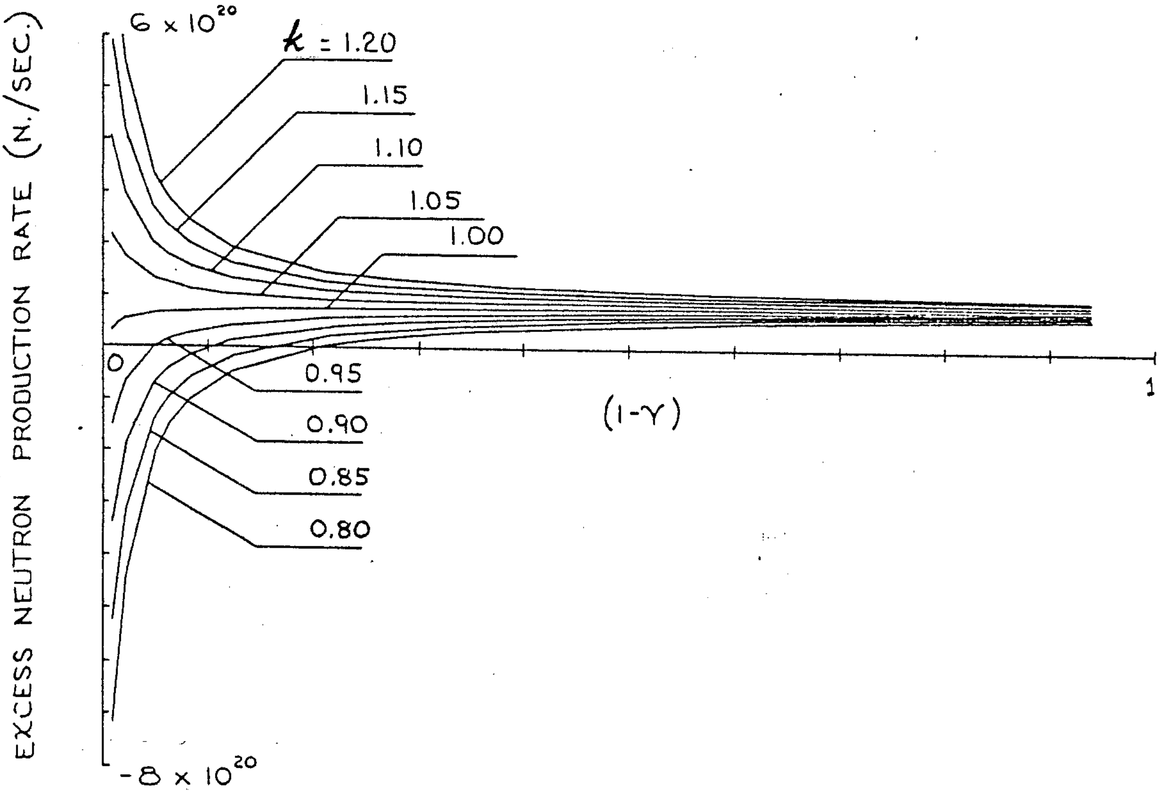

Figure 2.4.3 Net Neutron Production Rate for Fixed Values of k (effecttive tritium breeding ratio in the blanket) versus Tritium Breeding Margin ($P = 30$ m^{2}T^4, $T_{io} = 20$ keV).

References

[1] GREENSPAN, E., BLUE, T. AND MILEY, G.H., in *Proceedings of the Fourth Topical Meeting on the Technology of Controlled Nuclear Fusion*, King of Prussia, Pa. (1981).

[2] COHN, D.R., BROMBERG, L., WILLIAMS, J.E.C., BECKER, H., LECLAIRE, R. and YANG, T., in *Proceedings of the Third Technical Committee Meeting and Workshop on Fusion Reactor Design and Technology*, Tokyo, Japan, October (1981).

[3] SIGMAR, D.J., JOYCE, G., Nucl Fusion **11** (1971) 447

[4] **INTOR**, International Tokamak Reactor, Phase One, Report of the International Tokamak Reactor Workshop help in Seven Sessions in Vienna dusing 1980 and 1981, International Atomic Energy Agency (1982)

[5] BROMBERG, L, COHN, D.R., FISHER, J., Nucl Fusion **19** (1979) 1359

[6] SCHULTZ, J.S., BROMBERG, L., COHN, D.R., Nucl Fusion **20** (1980) 703

3 MODEL OF RESISTIVE MAGNET

In this chapter, the assumptions used in the parametric code are discussed. Section 3.1 discusses the engineering assumptions for the magnet systems. The toroidal field coils are analyzed in terms of stress levels, electrical power requirements and cooling.

In section 3.2 the plasma assumptions are analyzed. The plasma requirements developed in the previous sections (such as γ, P, $\beta a B^2$) are incorporated into a machine sizing code.

Finally in Section 3.3 the assumption with respect to the neutronics of the blanket and shield and the insulator are analyzed. The influence of the blanket and shield region on the magnet are discussed. Detailed neutronic calculations have not been performed on these machines, but previously reported results provide information of use in assessment.

Throughout this chapter it is assumed that the magnet is built with *BITTER* coils that surround most of the plasma, as in the *ALCATOR* machines [1] and in *ZEPHYR* [2]. However, the requirements and parameters derived are in most cases directly applicable to other types of magnet structures.

The parametric scans as function of the engineering, neutronics and plasma requirements are presented in next chapter. Although the purpose of a sizing code is to evaluate the cost of different alternatives, the code only presents scaling of the different factors that enter into the cost. Due to large unknowns in estimating the cost, we think that this is an attractive alternative to the approach that looks at just one parameter that may (or may not) be related to the true cost.

3.1 Magnet Requirements

In this section the toroidal (Section 3.1.1) and poloidal (section 3.1.2) field systems are analyzed. The discussions of the toroidal field coil are specific to Bitter magnets. However, most of the discussion is relevant to alternate resistive magnet systems.

It is estimated that, although not the largest element of the cost, the poloidal field system is important in calculating the cost of the total system. Therefore, a simple model for the poloidal field system (one that does not require running an equilibrium calculation for each case) is necessary. The simple model was obtained by doing a numerical fit to a large number of runs of the equilibrium field code. The fit is then used to analyze the main characteristics of the poloidal field system. Although not as precise or as general as the equilibrium field code (the main characteristics of the geometry are assumed), the numerical fit is a powerful tool. The procedure is described in Section 3.1.2.

3.1.1 Toroidal Field Magnet

The requirements of the toroidal field magnet imposed by plasma considerations are probably the largest driver of the cost of the total machine, as many of the systems scale with the characteristics of the *TF* magnet (such as the power supplies, the stored energy and the shielding). In this section the stresses in the magnet, the power supply requirements (both steady state power requirements and energy stored in the magnet) and the heating in the *TF* coils are discussed.

In a Bitter type configuration, there are several stresses that dominate the design. These are the tensile stresses (that is, the principal stress of the magnet) in the throat, the circumferential (or hoop) stress in the throat due to the wedging action of the magnet, the bending stresses in the horizontal legs, and the shearing stresses in the outer leg of the magnet (those resisting the action of the overturning moments due to the interaction between the *TF* current and the equilibirum fields).

The throat principal stresses determine the maximum field at which the machine can operate. The only way to increase the loading capacity of the throat (without changing the composition of the throat) is by making the machine larger. The bending stresses of the horizontal leg can be decreased by increasing the machine height, and therefore are not limiting. The shearing stresses in the outer legs of the magnet determine the size and concentration of the keys used to control the torsional forces. In order to reduce the requirements on the keys, the thickness of the outer leg of the magnet can be increased. However, because this region carries most of the material in the machine, the weight of the reactor is strongly dependent on this thickness.

Assuming that the tensile stresses in the throat of the magnet are uniform (this is approximately true for the *ALCATOR* C [1] and *ZEPHYR* [2]), the average tensile stresses in this region are given approximately by

$$\sigma_{TF} = \frac{\frac{3}{2\pi} M_T - \frac{1}{\pi}\frac{R_o^3 - R_b^3}{R_o^2 - R_b^2} F_T}{R_a^3 - R_i^3 - \frac{R_o^3 - R_b^3}{R_o^2 - R_b^2}(R_a^2 - R_i^2)} \qquad 3.1.1$$

where F_T and M_T are respectively the total upward force and the moment due to the magnetic field. F_T is given by

$$F_T = \frac{\pi B_T^2 R^2}{\mu_o}\left(\ln\left(\frac{R_b}{R_a}\right) + \frac{1}{4}\left(1 - \frac{R_i}{R_a}\right)^2 + \left(1 - \frac{1}{3}\frac{R_i}{R_a}\right)\frac{R_i}{R_a}\right) \qquad (3.1.2)$$

and M_T is given by

$$M_T = \frac{\pi B_T^2 R^2}{\mu_o}\left(R_b - R_a + (R_a - R_i)\left(\frac{1}{5}\left(1 - \frac{R_i}{R_a}\right)^2 + \frac{1}{2}\frac{R_i}{R_a}\left(1 - \frac{R_i}{R_a}\right) + \frac{1}{3}\left(\frac{R_i}{R_a}\right)^2\right)\right) \qquad (3.1.3)$$

R_o and R_i are the outer and inner major radii of the toroidal field coil. B_T is the toroidal field at the location of the plasma major radius R. R_a and R_b are given by

$$R_a = R - a - \delta_i$$

and

$$R_b = R + a + \delta_o$$

where R and a are the major and minor radii of the plasma. δ_i relates to the plasma-*TF* coil distance in the inner side of the torus. This distance includes the plasma scrape-off distance, the thickness of the first wall, the support structure of the first wall and the inboard blanket/shield thickness. Similarly, δ_o refers to the plasma-*TF* coil distance in the outer side of the torus. It is assumed that the vertical distance between the plasma and the horizontal legs of the toroidal field coils is given by δ_T (See Figure 3.1.1).

In deriving equation (3.1.1) It has been assumed that the magnetic field increases linearly in the throat of the magnet and that the forces generated in the outer limb of the magnet are small (the results change by $\sim 3\%$ when they are included). Also, the horizontal magnetic forces and the moments on the midplane of the machine were ignored. It is not clear how to include these forces and moments analytically. This is due to the fact that the model for the toroidal field coil is indeterminate. However, it is estimated from calculations using shell theory and from finite element calculations that the effect of the couple caused by these forces is a net increase of the tensile stresses in the throat of the magnet of $\sim 30\%$.

The *BITTER* geometry does not have a bucking cylinder that supports the centering forces. The centering forces on the *TF* coil result in face pressure on the individual plates, resulting in hoop stresses. The compressive stresses in the throat resulting from these forces are important. They add to the total and von Mises stresses, and in some cases, can be larger than the tensile stresses in the throat. The face pressure σ_c is calculated assuming that the throat of the magnet behaves as a thick cylinder. The circumferential streses are given by:

$$\sigma_c = \frac{F_\theta}{R_a - R_i}$$

where F_θ is given by

$$F_\theta = \frac{\mu_o I_{TF}^2}{2\pi^2}\left(\frac{R_a^3 - R_i^3}{3} - R_i^2(R_a - R_i)\right)\left(\frac{1}{(R_a^2 - R_i^2)^2}\right) \tag{3.1.4}$$

I_{TF} is the current in the toroidal field coils,

$$I_{TF} = \frac{2\pi R B_T}{\mu_o}$$

It has been assumed that the current density in the throat of the magnet is uniform and that the throat of the magnet behaves like a thick cylinder. Results from finite element calculations agree with calculations using equation 3.2.2.

A shell method has been used to calculate the stresses in some of the cases. The results from the code can be summarized as follows:

- The average tensile stresses in the throat of the magnet can be accurately described by $1.3 \times \sigma_{TF}$.
- There can be significant bending in the throat of the magnet. This bending has to be calculated using the shell model.
- The circumferential compressive stresses (or hoop stresses) in the throat of the magnet can be accurately described by σ_c.

The bending stresses in the horizontal legs are determined by calculating the bending moments in the horizontal legs of the magnet and then calculating the corresponding bending stress using elementary theory if beams. Using this approach it is found that the bending stresses are relatively flat in the thin section of the horizontal legs. The height of the magnet that results in a maximum bending stress of 70 MPa (10 kpsi) is then determined. Because the corner regions are ignored, this method of calculating the bending results in an overestimate of the stresses by about $\sim$ 50%. However, the factor by which the bending stresses are overestimated is about constant over a wide range of parameter space. Furthermore, in order to decrease the resistive losses, it is necessary to increase the height of the machine beyond what is strictly necessary to restrain the applied forces. Increasing the width of the horizontal legs of the magnet has a significant effect in decreasing the resistive power losses.

There is an additional source of concern in *BITTER* magnets. That is, the out of plane forces, usually called "overturning". These forces are the equivalent of putting the magnet under torsional loads. In *BITTER* magnets, the out of plane forces are resisted by shear in the outside section of the *TF* coil. This shear can be carried in different regions. In the case of *ZEPHYR* [2] and *ALCATOR* [1], the shear occurs between the plates of the toroidal field magnet. The plates are joined by bonding, by keying, or by the friction resulting from the wedging force from either the toroidal field action or from a girth band around the machine. The resulting structure resembles that of a cylinder subject to torsion loads.

The out of plane forces are generated by the interaction between the equilibrium field and the toroidal current in the toroidal field magnet. The acting torque is calculated by simplifying the magnet geometry representing it as elliptical sectors, as shown in Figure 3.1.2. The TF current density is assumed uniform in sectors that are normal to the inner wall of the *TF* coil. The equilibrium field is calculated from the equilibrium field coil locations and currents.

The method for determining the coil locations and coil currents is described below in the poloidal field section. The torque is then determined by

$$T_R = \int (\mathbf{j} \times \mathbf{B}_{poloid}) R dV$$

where $\mathbf{j}$ is the current density in the TF coil, $\mathbf{B}_{poloid}$ is the poloidal field (in the direction normal to the toroidal direction), and R is the major radius. The integral is over the volume of the TF coil, approximated by the shape shown in Figure 3.1.2. The shearing force in the outer leg of the TF coil necessary to prevent the torsion is then given by

$$\tau_R = \frac{T_R}{2\pi (R_o - t_{out}/2)^2 t_{out}}$$

Here t_{out} refers to the radial width of the outer leg of the TF field coil at the midplane. Finite element calculations indicate that the value of τ_R calculated using the above formula underestimates the peak shearing stresses. Approximate agreement is obtained when τ_R calculated using the above formula is multiplied by a factor of 3.5

The stored energy and resistive powers in the toroidal field and poloidal field magnets are calculated. The power supply requirement for the TF magnet scales with the resistive power of the machine. The stored energy in the TF magnet is related through the Virial theorem to the amount of material required. The stored energy and resistive energy in the poloidal field coils mandate the power and energy handling capability of the poloidal field power supplies.

In order to calculate the stored energy in the toroidal field, the energies in the bore of the magnet and in the conductor of the TF coil are calculated separately. The energy in the bore of the toroidal field coil is calculated by integrating the toroidal field, with a $1/R$ dependence, over the volume of the bore. To calculate the energy stored in the conductor, the geometry of Figure 3.1.2 is used. The volume of the coil is divided in several poloidal sectors. The stored energy in each sector is calculated from the current density, and the integration is performed radially. Then the sectors are added together. The spatial distribution of the current density has a small effect on the total energy stored in the *TF* coil, and is assumed uniform. In typical *BITTER* magnets, the energy in the conductor of the *TF* coil is 20-40% of the energy stored in the toroidal bore of the magnet.

The resistive power of the *TF* coil is calculated assuming the geometry shown in Figure 3.1.2. The current density is the same as the one used to calculate the energy in the conductor and the torques. It is assumed that 10% of the cross-sectional area of the throat is used for cooling and insulation and that the rest is conductor. In the outer leg of the *TF* coil, a larger fraction is allowed for structure material. Steel wedges are placed between copper coils, and therefore the conductor filling fraction is decreased. It is assumed that the copper filling fraction at the outermost location is 60%. The steel wedges start at a major radius equal to the plasma major radius. The conductor used is copper, cooled with water.

3.1.2. Poloidal Field System

The requirements for the poloidal field system are determined from plasma physics calculations performed in section 3.2.2. The equilibrium field interacts with the toroidal field magnet producing out-of plane forces. The field is calculated from known coil locations and coil currents. The EF coil currents and locations depend on the current density in the EF coils. This is due to the presence of the *TF* coil which excludes the coils from certain regions in space. The EF coil currents, on the other hand, increase with distance to the plasma. Therefore, changing the current density in the EF coils affects the centroid of the current, and this in turn affects the coil currents.

The stresses in the equilibrium field coils are small compared with the other stresses in the system, and are not dealt with in the parametric code. The stresses are not a driving term in the vertical field system because the resistive power consumed in this system would be very large if the coils were to be determined by a high-stress assumption.

The energy in the poloidal field systems is calculated from the location and currents of the equilibrium field coils. The coil locations and coil currents are determined as indicated in section 3.2.2. The energy is important because the peak power requirements in the equilibrium field power supplies is determined by the energy swing during startup. Tradeoffs in the vertical field system (coil location, stored energy, peak reactive power, and resistive power during burn) are performed in chapter 4.

The *OH* system is analyzed. The contribution to the current drive from the vertical field system can be obtained by integrating the equilibrium field on the midplane of the machine. The integration is performed from the center of the machine to the plasma axis. Not all the flux contributes to the plasma current and a correction factor less than one is used to determine the contribution to the inductive drive from the equilibrium field system. In this report it is assumed that 0.8 of the flux between the main axis of the machine and the plasma axis contributes to the current inductive drive.

The available space for the *OH* transformer is determined by the *TF* coil. The *OH* transformer has to provide the difference between the flux drive required by the plasma and the flux provided by the vertical field system.

Once the flux requirements of the *OH* field system have been estimated, then the stresses, power dissipation and stored energy in the *OH* system can be calculated. It is assumed that the *OH* transformer is partially double swung (from full field in the core of the *OH* transformer to half-peak field in the opposite direction). The stresses are calculated assuming that the *OH* transformer behaves like a cylinder with free floating shells. Then the stress is given by

$$\sigma_{OH} = \frac{0.5B_{OH}^2(R_{OH,o}(R_{OH,o}^2 - R_{OH,i}^2) - 0.33(R_{OH,o}^3 - R_{OH,i}^3))}{\mu_o f(R_{OH,o} - R_{OH,i})^3}$$

where f is the filling fraction of conductor/structure in the *OH* tranformer, B_{OH} is the peak field in the *OH* transformer, and $R_{OH,o}$ and $R_{OH,i}$ are the outer and inner radii of the *OH* transformer, respectively (see Figure 3.1.1).

B_{OH} is determined from the flux swing required from the *OH* transformer,

$$B_{OH} = \frac{\phi_{OH}}{\pi R_{OH,i}^2}(1 + \frac{2R_{OH,i} - 3R_{OH,o} + R_{OH,o}^2 R_{OH,o}/R_{OH,i}^2}{3(R_{OH,o} - R_{OH,i})})$$

Here ϕ_{OH} is the flux required for the *OH* tranformer.

The power handling requirements during startup dominate the power handling requirements of the power supplies for the *OH* transformer. The energy stored in the *OH* field is an estimate for the peak inductive power requirements.

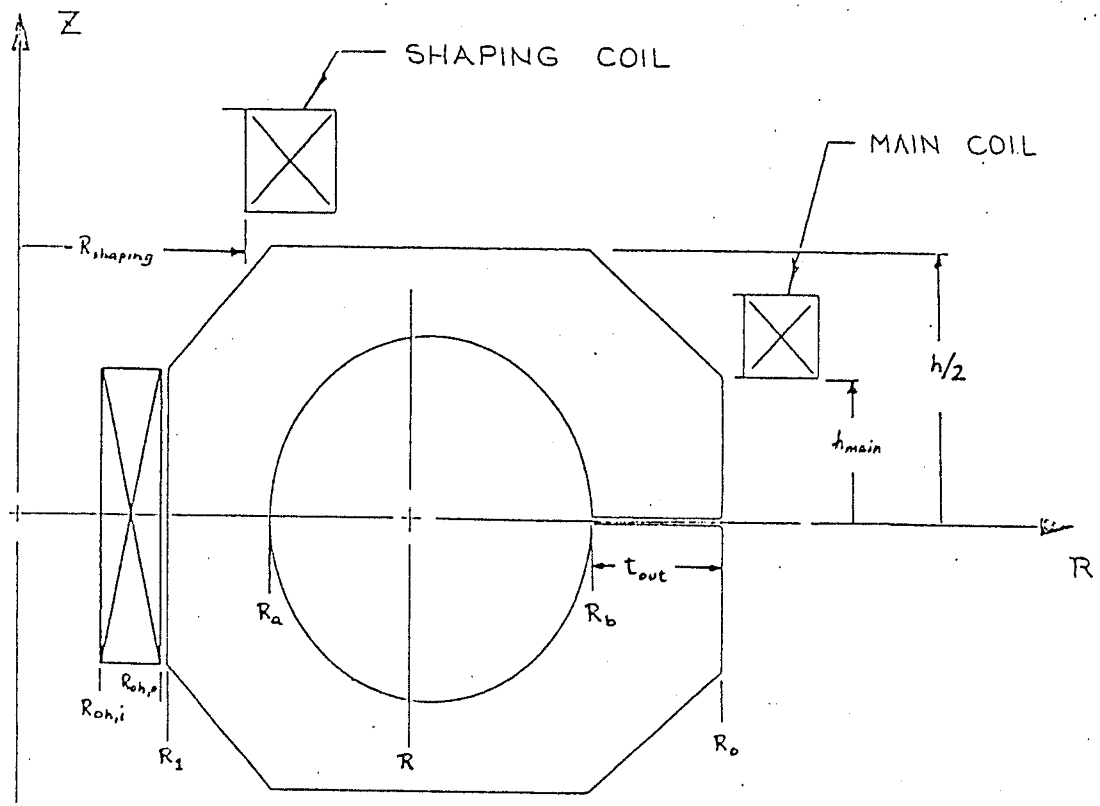

Figure 3.1.1 Definition of Geometric Parameters

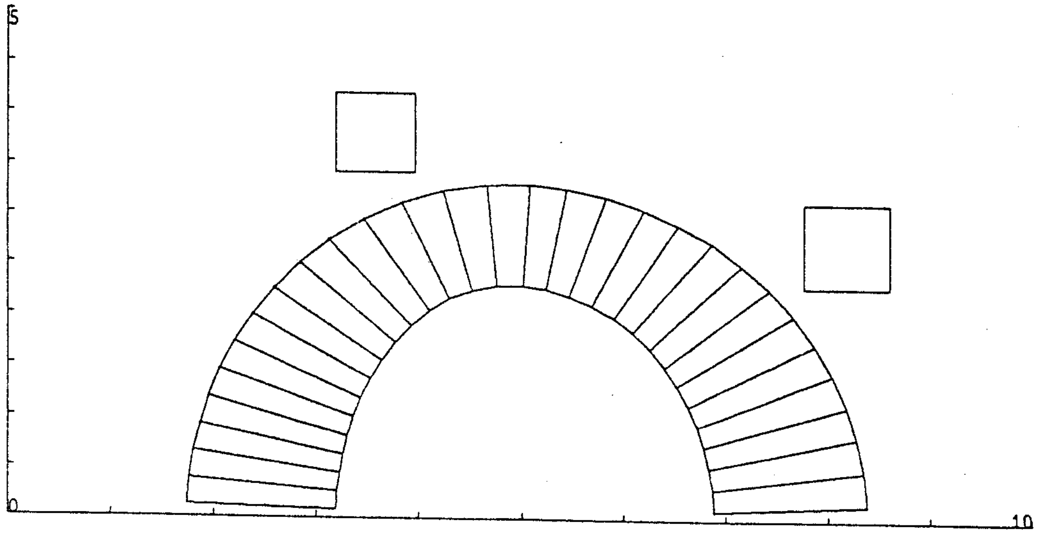

Figure 3.1.2 Simplified Geometry of *AFTR* Device

3.2 Plasma Characteristics

In this section, the plasma physics relevant to the machine are described. The plasma requirements in terms of $\beta a B_T^2$, γ and P are given in chapter 2. Section 3.2.1 describes the plasma characteristics and the underlaying plasma physics assumptions. Section 3.2.2 describes a novel method for determining the poloidal field requirements.

3.2.1 Plasma Scaling

The plasma β is defined as

$$\beta = \frac{\int \frac{3}{2}(n_i k T_i + n_e k T_e) dV}{B_T^2 / 2\mu_o}$$

where B_T is the toroidal magnetic field at the plasma major radius (geometrical axis), the integral is performed over the plasma volume, n_i and n_e are the ion and electron densities and T_i and T_e are the ion and electron temperature, respectively.

It is assumed that the maximum achievable toroidal beta β scales as

$$\beta = 1.05 \frac{\kappa}{A q^2}$$

where A is the aspect ratio, q is the safety factor at the limiter radius, and $\kappa = b/a$ is the elongation. Although experimental determination of this scaling has yet to be proven, MHD balloning-mode theory predicts this scaling.

Low values of q are desireable because of the large leverage that q has on β. Although $q \leq 2$ has been achieved in some machines, the regime $q \geq 2$ is more reachable. Therefore, it is assumed that $q = 2.5$ for the illustrative design point.

In terms of the elongation, the poloidal field system becomes complex as the elongation increases, not only because the currents are increasing with elongation (see next section), but because the plasma becomes more unstable against vertical instability. This requires larger power supplies with faster response time to control the disturbances. An elongation of $S = 1.5$ has been choosen for the illustrative design.

As mentioned in Chapter 2, the energy confinement time is determined by *ALCATOR* empirical scaling [3]

$$(\tau_e)_{emp} = 0.5(\tau_E)_{emp} = 3.8 \times 10^{-21} n\, a^2$$

where n is the average electron density in m^{-3}, a is the minor radius in m and τ_e is in s. The factor of 0.5 in this equation is due to the fact that $(\tau_E)_{emp}$ is defined as the global energy confinement time, even though most of the heat flux is due to the electrons. It is assumed that the ion energy confinement time, τ_i is given by neoclassical theory. In this case τ_i is generally much greater than τ_e. The *ALCATOR*-empirical scaling law implies that the minor radius required for a given value of P is

$$a_{ign} \sim \frac{1}{n} \sim \frac{\sqrt{P}}{\beta B_T^2}$$

The heating power required for ignition is determined from the empirical scaling law. It is assumed, however, that the plasma composition is near DT, so that the alpha energy from the DT reactions help the plasma heating early in the startup, thus reducing the required heating power. The tritium fraction would then be lowered by allowing it to burn or by pumping it out. Note that the fraction of tritium need not be 50% for the plasma reactivity close to that of DT. A $10-90$ D-T plasma has $\sim$ 40% of the reactivity of a $50-50$ DT plasma. With the empirical scaling law, the heating power scales as $P_{aux} \sim \kappa R$.

The machine allows for significant access through ports located at the outer leg of the *TF* coil, and for some rather small vertical access in the horizontal legs. As the access area for *BITTER* scales as $A_{port} \sim a\kappa R_o$ (R_o is the outer radius of the *TF* coil, a is the plasma minor radius and κ is the elongation), then the heating power density P_{den} is

$$P_{den} = \frac{P_{aux}}{A_{port}} \sim \frac{R}{R_o a} \sim \frac{1}{a}.$$

$R_o/R \sim$ constant when the aspect ratio is varied for fixed plasma and engineering requirements Therefore, from an access point of view, large minor radius (low aspect ratios) are desirable.

In a tritium-rich start-up, the densities required for ignition are not different from those for DT machines. Consequently, the heating mechanism used for DT plasmas would be sufficient. However, if a tritium-lean startup is desired, then higher plasma densities are required. This would probably rule out neutral beams based on positive ions. This may also rule out some methods of heating using *RF* .

The neutron wall loading P_{wall} is defined as

$$P_{wall} = \frac{P_{neutrons}}{A_{plasma}}$$

where $P_{neutron}$ is the fusion power carried by the neutrons and A_{plasma} is the plasma surface. There is a difference between P_{wall} and the first wall average neutron loading due to shape considerations of the first wall and to finite scrape off distance between the plasma and the first wall.

In these designs, it is assumed that a pump limiter is used to provide impurity and ash control. The *BITTER* magnet is compact, and the possibility of a divertor in the machine has neither been analyzed nor ruled out.

The burn pulse is ultimately determined by the flux swing limitations of the *OH* transformer. The flux swing requirements are determined by the inductive and resistive volt seconds for the plasma. The inductive volt-seconds required are calculated using the results from section 3.2.2.

The resistive flux swing requirements are calculated assuming that the plasma is relatively free of impurities ($Z_{eff} = 1.3$) and including finite aspect ratio corrections. High temperature operation results in longer burn times because of reduced plasma resistivity. However, higher temperatures result in more stringent ripple requirements. The operating electron temperature is assumed to be $T_{eo} = 20$ keV.

The burn pulse length in the base case is $\tau_{burn} = 100$ s. Longer burn times can be achieved by either increasing the stresses in the *OH* transformer or by going to a larger *OH* transformer. The tradeoffs between machine size and burn pulse length are indicated in chapter 4.

3.2.2 Equilibrium Field Calculations

In this section a method for estimating poloidal field requirements is described. The usual procedure to calculate poloidal field requirements requires the use of sofisticated codes that solve the plasma equilibrium [4]. In one scheme of sizing the equilibrium field, a fixed boundary solution is obtained, and then coil currents in specified location are estimated to reproduce the fields in the boundary. Then a free boundary solution is calculated. The procedure is straight forward but time consuming, and only a very limited number of cases can be analyzed.

An alternative to this method is that of running a relatively small number of cases that span most of the parameter space in which we are interested, and then perform a numerical fit to the results.

It has been assumed that the parameters in the poloidal field system depend on the following parameters:

R	(major radius of plasma)
B_T	(toroidal field at R)
$A = R/a$	(plasma aspect ratio)
$\kappa = b/a$	(elongation)
q	(plasma safety factor)
$\beta_p \sim \dfrac{\beta A q^2}{\kappa}$	(poloidal beta)
$\dfrac{R_j}{R}$	(normalized major radius of poloidal field j^{th} coil)
$\dfrac{Z_j}{a\kappa}$	(normalized height of poloidal field j^{th} coil)

Here Z_j is the height above the midplane of the j^{th} coil, and R_j is the major radius location of the j^{th} coil. q is the safety factor of the machine, defined as

$$q = \frac{2\pi}{\iota}$$

where ι is the rotational transform of the plasma.

The dependence on plasma pressure should be on β_p, not on β. For values of $\beta_p < A$ and for $A \geq 2$, β_p scales as

$$\beta_p \sim \beta A q^2 / \kappa$$

Through $\beta A q^2/\kappa$, the parameters in the vertical field system depend on β_p.

The functional dependence on the coil currents is assumed to be

$$I_j = I_j(R, B_T, A, \kappa, q, \frac{\beta A q^2}{\kappa}, \frac{R_i}{R}, \ldots, \frac{R_n}{R}, \frac{Z_1}{a\kappa}, \ldots, \frac{Z_n}{a\kappa})$$

where I_j is the current in the j^{th} poloidal field coil. There are n coil pairs.

Similarly, the plasma current can be expressed as

$$I_p = I_j(R, B_T, A, \kappa, q, \frac{\beta A q^2}{\kappa})$$

The contribution of the vertical field system to the inductive drive of the plasma can be described by

$$\phi_{EF} = \phi_{EF}(R, B_T, A, \kappa, q, \frac{\beta A q^2}{\kappa})$$

In the calculations that have been performed with the full equilibrium calculations, it is found that two set of coils gave enough flexibility to produce the desired equilibrium. Therefore, we have limited the analyzsis to two sets of coils, located symmetrically about the midplane. The coil approximate location is shown in Figure 3.1.1. Coil set 1 is the main equilibrium field coil pair (dipole field), while coil set 2 is the shaping coil pair (quadrupole field).

The numerical calculations with the equilibrium field code have been performed by varying one of the variables at a time, and then finding a numerical fit to the solution. It was assumed that

$$I_j = f_1(R) f_2(B_T) f_3(A) f_4(\kappa) f_5(q) f_6\left(\frac{\beta A q^2}{\kappa}\right) f_7\left(\frac{R_i}{R}\right) f_8\left(\frac{R_2}{R}\right) f_9\left(\frac{Z_1}{a\kappa}\right) f_{10}\left(\frac{Z_2}{a\kappa}\right),$$

that is, the function is separable on the variables. For a limited variation in parameter space this form of the fit is mathematically justifiable.

The numerical fits for the current in the main equilibrium field coil I_1 is given by

$$\begin{aligned} I_1 = & 5.59 \times 10^6 \left(\frac{R}{3.03}\right)\left(\frac{B}{6.7}\right) \times \\ & \left(\frac{A}{3.36}\right)^{-1.48+0.095(A-3.36)} \left(\frac{q}{3.18}\right)^{-0.88(1.+0.2(q-3.1))} \times \\ & \left(\frac{\kappa}{1.5}\right)^{2.0} \left(\frac{c_\beta q^2/\kappa}{0.2(3.18)^2/1.5}\right)^{0.34} \times \\ & \left(\frac{R_i}{R_{1,base}}\right)^{0.9} \left(\frac{Z_1}{Z_{1,base}}\right)^{0.7} \left(\frac{R_2}{R_{2,base}}\right)^{0.5} \left(\frac{Z_2}{Z_{2,base}}\right)^{0.25} \end{aligned}$$

and for the current in the shaping field coil I_2,

$$
\begin{aligned}
I_2 = & -3.39 \times 10^6 \left(\frac{R}{3.03}\right)\left(\frac{B_T}{6.7}\right) \times \\
& \left(\frac{A}{3.36}\right)^{-1.88+0.13(A-3.36)} \left(\frac{q}{3.18}\right)^{-0.4(1.0+0.3(q-3.1))} \\
& \left(-0.54 + 1.56(\kappa/1.5)^4\right)\left(\frac{c_\beta q^2/\kappa}{0.2(3.18)^2/1.5}\right)^{0.08} \times \\
& \left(\frac{Z_1}{Z_{1,base}}\right)^{0.8}\left(\frac{Z_2}{Z_{2,base}}\right)^{2.25}
\end{aligned}
$$

I_1 refers to the current in the main equilibrium field coils (the dipole coils) and I_2 refers to the current in the shaping coils (the quadruple coils).

Here it has been assumed that

$$\beta = c_\beta / A,$$

and that

$$
\begin{aligned}
Z_{1,base} &= 1.85 \frac{a\kappa}{1.35}, \\
Z_{2,base} &= 3.53 \frac{a\kappa}{1.35}, \\
R_{1,base} &= 6.72 \frac{R}{3.03}, \\
R_{2,base} &= 3.30 \frac{R}{3.03}.
\end{aligned}
$$

The plasma current is approximately given by

$$I_p = 6.59 \times 10^6 \left(\frac{R}{3.03}\right)\left(\frac{B_T}{6.7}\right)\left(\frac{A}{3.36}\right)^{-2.1}\left(\frac{q}{3.2}\right)\left(\frac{\kappa}{1.5}\right)^{1.15}\left(\frac{c_\beta q^2/\kappa}{0.2(3.2)^2/1.5}\right)^{0.17}$$

The contribution due to the vertical field system to the inductive drive of the plasma is calculated using the locations of the coils and their currents, and then integrating the field on the midplane from the major axis of the machine to the plasma axis. The numerical fit for the inductive volt seconds from the vertical field system is approximately given by

$$\begin{aligned}\phi_{EF} = 0.8 \times 18.\left(1. + 1.43\left(\frac{1.5}{3.3 \times 3.2^2}\right)\left(\frac{c_\beta q^2}{\kappa} - \frac{.2 \times 3.2^2}{1.5}\right)\right) \times \\ \exp\big(0.28(1. + (\kappa - 1.5))(\kappa - 1.5)\big)\left(\frac{A}{3.36}\right)^{-1.69} \times \\ \left(\frac{q}{3.2}\right)^{-1.16(1.+.25(q-3.2))} \times \left(\frac{B_T}{6.7}\right) \times \left(\frac{R}{3.03}\right)^{1.9}\end{aligned}$$

The specific numbers that appear in the fit correspond to the numbers of the base case that has been used in the calculations with the equilibrium field code. The linear dimensions are in m, B_T is in T, I_j is in A and ϕ_{EF} is in T m^2.

The position of the coils are determined by the location of the *TF* field coil, with a clearance distance between the toroidal field coil and the poloidal field coils and by the dimension of the poloidal field coils. The current density in the poloidal field coils determines the coil dimension, which in turn determines the location of the coils and their current. This procedure is repeated until the coil locations and currents are self consistently determined. The procedure is very simple, and fast sizings of the equilibrium field system can be obtained in this manner. Although the number of coil sets has been limited to two, this is not a fundamental limitation, and the procedure can be altered to increase the number of coils. However, the main characteristics of the system have to remain constant (the method probably can not be expanded to encompass both divertor and divertorless cases, for example).

In the parameters of the next chapter, it is assumed that $R_{shaping} = R_a$, $h_{main} = \kappa a + 0.5$ m. The clearance between the TF coil and the EF coils is assumed to be 0.10m.

3.3 Neutronics

At least three considerations are important for good fusion reactor neutronics design. First, the breeding of tritium in the blanket must be large enough for reactor fuel self-sufficiency. Second, the neutron damage to blanket components, to magnets, and to other equipment must be compatible with design lifetimes. Finally, as a corollary to the other two items, the neutronics treatment must be adequate for special regions adjacent to beam heating ducts, limiters, etc. (to assure that appropriate local adjustments to breeding and neutron damage are adopted).

In the *AFTR* studies, we have not performed neutronics calculations. We have however, examined neutronics results reported for STARFIRE [5] and have compared pertinent reactor features.

3.3.1 Breeding

We have concentrated on the STARFIRE results for a blanket module with the following composition:

- The first wall is Be-coated austenitic stainless steel
- The neutron multiplier region is zirconium lead (Zr_5 Pb_3)
- The second wall is austentic stainless steel
- The tritium breeder is 60% effective density lithium aluminate ($LiAlO_2$) with the lithium enriched to 60% Li_6 (with a fine grain size and bimodal pore distribution)

- The reflector is graphite

- The coolant in all regions is pressurized water

- The sweep gas for on-line tritium removal is helium

The thickness of each blanket region is given in Table 3.3.1. Other information relating STARFIRE parameters to those of *AFTR* is supplied in Table 3.3.2

Some features in Table 3.3.2 imply that the *AFTR* breeding ratio may be higher than that of STARFIRE:

- The duct and inner blanket area percentage is lower, giving a greater percentage of the high breeding outer blanket

- The *AFTR* aspect ratio is higher, resulting in more neutrons going to the outer blanket

Other features in Table 3.3.2 imply that the *AFTR* breeding ratio may be lower than that of STARFIRE or that the direction is uncertain:

- The neutron wall loadings (and surface heat deposition rates) are significantly higher, requiring more space for cooling components

- The *AFTR* elliptical plasma has high power density regions closer to the inner blankets

- Some of the effects mentioned (i.e. inner blanket area and plasma centering) may be modified if the *AFTR* plasma evolves from elliptical shape to D-shape during detailed design work.

It is not clear whether the k value for *AFTR* is smaller or larger than the 1.04 given for STARFIRE. It is also not clear whether the k value of 1.04 is sufficiently large for the DT case ($\gamma = 1$). Allowances are required for calculation uncertainties, for losses during tritium recovery from the blanket, and for tritium losses during fueling and plasma rejuvenation. However, it seems quite likely that the *AFTR* value for k will be sufficiently large for DD-DT operation ($\gamma = 0.93$).

3.3.2 Neutronic Damage

The neutron damage to the insulation of the magnet coils within the inner blanket in *AFTR* must be kept acceptably low. There is evidence that [6] essentially no damage will occur for a fast neutron (> 0.1 MeV) fluence, N_F, which satifies:

$$N_F \leq 10^{24} \mathrm{n/m}^2$$

It is likely that damage will be acceptably small for at least a decade higher fluence:

$$N_F \leq 10^{25} \mathrm{n/m}^2$$

The *AFTR* inner blanket has no shield between the blanket and the toroidal field coil to protect the magnet insulation.

3.3.3 Special Region Effects

No special region calculations have been completed to assure that local breeding and local neutron damage are adequately treated. The problems in these *AFTR* regions seem generally similar to those in STARFIRE. The shielding associated with neutron streaming may require special care in *AFTR* since no bulk shielding is employed. Special region problems do not appear to be unduly difficult.

Table 3.3.1

Blanket Region Thickness (mm)

	STARFIRE	*STARFIRE*	*AFTR*	*AFTR*
Region	Outer	Inner	Outer	Inner
First Wall	10	10	10	10
Multiplier	50	50	50	50
Second wall	10	10	10	10
Breeder	460	280	440	290
Reflector	150	0	150	0
Total	680	350	660	360

Table 3.3.2

Breeding-Related Information

	STARFIRE	*AFTR*	Line
Radius Cavity CL (m)	7.00	4.82	(1)
Radius Inner First Wall (m)	4.81	3.48	(2)
Difference (m)	2.19	1.34	(3)=(1)-(2)
Aspect Ratio	3.20	3.60	(4)=(1)/(3)
First Wall Area (m^2)	773	332	(5)
% Outer Blanket	77.5	82.3	(6)=100-(7)-(8)
% Inner Blanket	18.7	10.5	(7)
% Ducts, Etc.	3.8	7.2	(8)
ID Breeding Ratio Outer	1.21	1.20	(9)
ID Breeding Ratio Inner	1.15	1.16	(10)
k (3D Breeding Ratio)	1.04	-	(11)
Neutron Wall Loading (MW/m^2)	3.6	$6.9^{\dagger}$	(12)
Fusion Power (MW)	3480	2910	(13)
Blkt Life (full power years)	4.5	2.3	(14)

† P_{wall} is defined as neutron power over plasma surface. The number here corresponds to actual average neutron loading on the first wall.

Notes

(a) These values are based on a multiple straight line representation of the actual first wall position.

(b) An elliptical representation of the *AFTR* plasma, allowing 0.14 m for scrape off, has an area of 288 m^2 (hence $8.0\ MW/m^2 \times 288 \div 332 = 6.9\ MW/m^2$).

(c) The 3D breeding ratio (line 11) was calculated by STARFIRE personnel. No simple extrapolation method was found for *AFTR* .

(d) Blanket life (line (14)) is based on equal exposures, $16.2\ MW \cdot y/m^2$.

References

[1] MONTGOMERY, D.B., The ALCATOR Project, Francis Bitter Mational Magnet Laboratory NML Report (September 1974); WEGGEL, C., HAMBURGER, W., MONTGOMERY, B., PIERCE, N. in *Proceedings of the Seventh Symposium on Engineering Problems of Fusion Research*, Knoxville, Tn (1977)

[2] WILLIAMS, J.E.C., BECKER, H.D., BOBROV, E.S., BROMBERG, L., COHN, D.R., DAVIN, J.M. and EREZ, E., MIT Plasma Fusion Center Report PFC/RR-81-24(1981)

[3] COHN, D.R., R. R. PARKER and D. L. JASSBY, Nucl Fusion **16** (1976) 31; JASSBY, D.L., D. R. COHN and R. R. PARKER, Nucl Fusion **16** (1976) 1045

[4] J.A. Holmes, Y-K. M. Peng, and S.J. Lynch, "Evolution of flux-conseving tokamak equilibria with preprogrammd cross sections," Jour Comput Phys, 36, 35-54, 1980

[5] BAKER, C. *et al.*, "STARFIRE-Commercial Tokamak Fusion Power Plant Study," Argonne National Laboratory Report ANL/FPP-80-1 (1980)

[6] BECKER, H., MIT Plasma Fusion Center, private communication (1982)

4 SCOPING STUDIES: INTRODUCTION

In this chapter, a scoping study is performed. The code described in the previous section is utilized. Variations discussed are with respect to the fuel mixture (*i.e.*, $1-\gamma$, the allowable stresses, pulse length, aspect ratio and the plasma-*TF* coil distance both in the inboard side and outboard side). The code is not a cost code, and the output is not a single number indicating cost but a series of numbers that should enter into the cost equation. There is a number of tradeoffs performed in selecting the base case.

In section 4.1, a scoping study is performed as a function of $1-\gamma$. The implications of operating in DD-DT fuel mixtures on the reactor size is analyzed. As stated before, a single number describing the cost is hard to derive.

In section 4.2, the influence of the blanket and shield size on the reactor is analyzed using the parametric code. The tradeoffs between reduced blanket thickness and reduced tritium breeding requirements due to DD-DT operation are discussed.

Section 4.3 presents the results of the parametric variations for a fixed value of $1-\gamma$. The main engineering and physics constraints are varied to look at their impact on the machine design.

Elongation tradeoffs are discussed in section 4.4. The tradeoffs involving elongation involve better calculations of the stresses in the magnet than what is provided by the simple analysis presented in chapter 3.

Section 4.5 presents an attempt to optimize the toroidal and poloidal field systems around the base case. The plasma is kept approximately constant while the location and current density of the poloidal field coils are varied, and specific parameters of the toroidal field coil are changed.

In chapter 5 a short discussion of the engineering problems of the magnet is given.

4.1 Parametric Analysis - Breeding and Engineering Tradeoffs

In this section, the tradeoffs between the plasma tritium breeding margin and plasma and device parameters is studied.

In order to compare machines that have similar properties, the neutron wall loading is kept constant. The wall loading (related to the neutron wall loading) determines the cooling required for the first wall, heat removal requirements from the plasma region and lifetime of the first wall (if limited by neutron irradiation). As operation with DD-DT fuel mixtures results in large variations of specific fusion power density $P_f/\beta^2 B^4$ as the value of $1-\gamma$ changes, operating at constant wall loading insures that the machines being scoped are comparable.

The main purpose of this machine is that of being an engineering test reactor, self sufficient in tritium production. The objectives of an engineering test reactor would be that of materials testing. In order to achieve this mission, the neutron wall loading has been chosen to be relatively high. In fact, for the scoping studies in this section, the neutron wall loading has been chosen to be $P_{wall} = 8$ MW/m^2. This wall loading corresponds to the neutron power divided to the plasma surface. The average neutron loading of the first wall would be smaller.

However, the *AFTR* device can also achieve the goal of producing tritium for utilization in fusion reactors that are not self sufficient in tritium, or that of breeding fissile material. For these latter applications, the *AFTR* device could be operated at lower wall loadings by operating with values of $1-\gamma$ that are larger than the value required for a materials test reactor (see chapter 2).

Table 4.1.1 shows the assumptions for the scoping study presented in this section. Δ_i and Δ_o represent the thickness of the inboard and outboard blanket/shield region. The electron temperature is 12 keV in DT, which correcponds to the lowest value of $n\tau_{ignition}$, while the peak temperature is increased in DD-DT in accordance with the results in chapter 2.

Table 4.1.2 shows the result from the parametric code as the plasma tritium breeding margin $1-\gamma$ is varied. The neutron wall loading is kept fixed, and the machine is allowed to increase in size to balance the reduced specific fusion power density P_f/β^2B^4 with increasing $1-\gamma$. Table 4.1.2 shows the results of the parametric scan. $1-\gamma$ increases from 0 (DT operation) to 0.21. A is the aspect ratio (chosen to be $A\sim 4$; this choice is justified in section 4.3). R and a are the major and minor plasma radii, B is the magnetic field on the plasma axis, I is the plasma current, P is the plasma performance defined in chapter 2 as $P = \beta^2B^4a^2$, P_f is the fusion power, W_{TF} is the magnet weight, T_R is the applied torque due to the interaction between the toroidal field coil with the vertical field, σ_{hoop} represents the hoop stresses in the throat of the magnet (the centering force present in toroidal magnets is taken in Bitter magnets through wedging), E_{TF} is the energy in the toroidal field system, P_{TF} is the power dissipated in the toroidal field system, $W_{blanket}$ is the weight of the blanket/shield, E_{OH} and P_{OH} are the energy and power dissipated in the ohmic transformer at peak field, and E_{EF}, P_{EF}, W_{EF} and MA_{EF} are the energy, dissipated power, weight and Ampere-turns of the vertical field system.

Also shown in Table 4.1.2 are the fusion power and wall loading assuming that the machines were operated in DT. Operationg at $1-\gamma = 0.21$ results in a net decrease of fusion power by a factor of 10 relative to DT operation. Note, however, that the machine designed for DD-DT operation cannot be run with DT due to the large wall loadings with DT operation. This restriction does not apply if the field in the machine or the plasma β are downgraded.

Figure 4.1.1 shows the normalized stored energy, the normalized resistive power of the TF magnet, the normalized fusion power and the normalized value of required plasma performance as functions of $1-\gamma$ for fixed wall loading. The values of P and E_{TF} required for operating at fixed wall loading increase very fast with increasing $1-\gamma$. The fusion power and the resistive power of the magnet increase slower. There is a large price to pay for operating at large values of $1-\gamma$ at fixed wall loading. Operating at lower values of $1-\gamma$ (~ 0.05) still results in a moderate increase in machine size.

Figure 4.1.2 shows the main parameters of the vertical field system as function of $1-\gamma$. The overall machine size and associated systems increase rapidly with increasing values of $1-\gamma$.

If the main goal of the *AFTR* device is that of tritium self sufficiency, then the value of $1-\gamma$ that results in this tritium self sufficiency should be chosen, as going to larger values of $1-\gamma$ results in larger than necessary machine size.

If the goal is for neutron applications (tritium or fissile breeding, for example), the situation is different. Figures 4.1.3 through 4.1.5 show the ratios of the excess neutron production to the resistive power dissipation, the stored energy in the toroidal field coil and the weight of the toroidal field coil as functions of $1-\gamma$ for constant wall loading (for the designs in Table 4.1.2). The excess neutron generation rate $R_n$is defined as

$$R_n \sim 3.6 \times 10^{20}(k - \gamma)P_f$$

where R_n is in neutrons per s, k is the effective breeding ratio of the blanket and P_f is the fusion power in GW. The generation of excess neutrons becomes more efficient (as defined by R_n/E_{TF}, R_n/P_{res} and R_n/W_{TF}) with increasing value of $1 - \gamma$ for $k \leq 1.1$ For $k > 1.1$, the ratio R_n/E_{TF} decreases with increasing $1 - \gamma$.

Although the unit size is increasing, the rate of production of excess neutrons increases faster than the unit size, resulting in more efficient excess neutron generation.

Table 4.1.1

Constraints for Scoping Study

P_{wall} (MW/m^2)	8
A	4
σ_{TF} (MPa)	150
$c_\beta = \beta_T \times A$	0.25
q	2.5
$\kappa = b/a$	1.5
T_{eo} (keV) DT	12
DD-DT	20
burn pulse lengths (s)	100
σ_{OH}(MPa)	150
Δ_i(m)	0.36
Δ_o(m)	0.66

Table 4.1.2

Parametric Scan of Device vs $1-\gamma$

$P_{wall} = 8$ MW/m^2, $\sigma_{TF} = 150$ MPa

$1-\gamma$	0.	0.035	0.068	0.12	0.21
A	4.09	3.98	4.07	4.05	4.07
R (m)	3.27	3.98	4.89	6.28	8.27
a (m)	0.8	1.0	1.2	1.55	2.03
B (T)	7.09	7.61	8.5	9.21	9.97
I (MA)	6.13	8.47	11.1	15.6	22.0
P (m^2 T^4)	6.05	13.2	28.4	65.9	154.
P_f (GJ)	1.26	1.93	2.84	4.7	8.1
DT equivalent operation					
P_{wall} (MW/m^2)	8.0	14.0	25.0	45.0	80.0
P_f (GJ)	1.26	3.37	8.86	26.5	81.2
σ_{hoop} (MPa)	0.125	0.136	0.149	0.163	0.179
W_{TF} (Gg)	2.71	4.13	6.49	11.7	23.3
T_R(GN m)	0.91	1.75	3.65	8.25	2.00
E_{TF} (GJ)	4.62	8,68	17.5	38.8	92.7
P_{TF} (MW)	307.	417.	610.	928.	1463.
$W_{blanket}$ (Gg)	0.0825	0.118	0.167	0.264	0.438
E_{OH} (GJ)	0.774	1.21	1.96	3.52	6.6
P_{OH} (MW)	55.0	52.9	55.2	56.5	58.1
E_{EF} (GJ)	0.934	1.55	2.7	5.33	11.4
P_{EF} (GW)	0.156	0.213	0.298	0.454	0.73
W_{EF} (Gg)	0.312	0.428	0.599	0.915	1.47
MA_{EF} (MA)	21.7	24.5	27.9	33.6	41.6

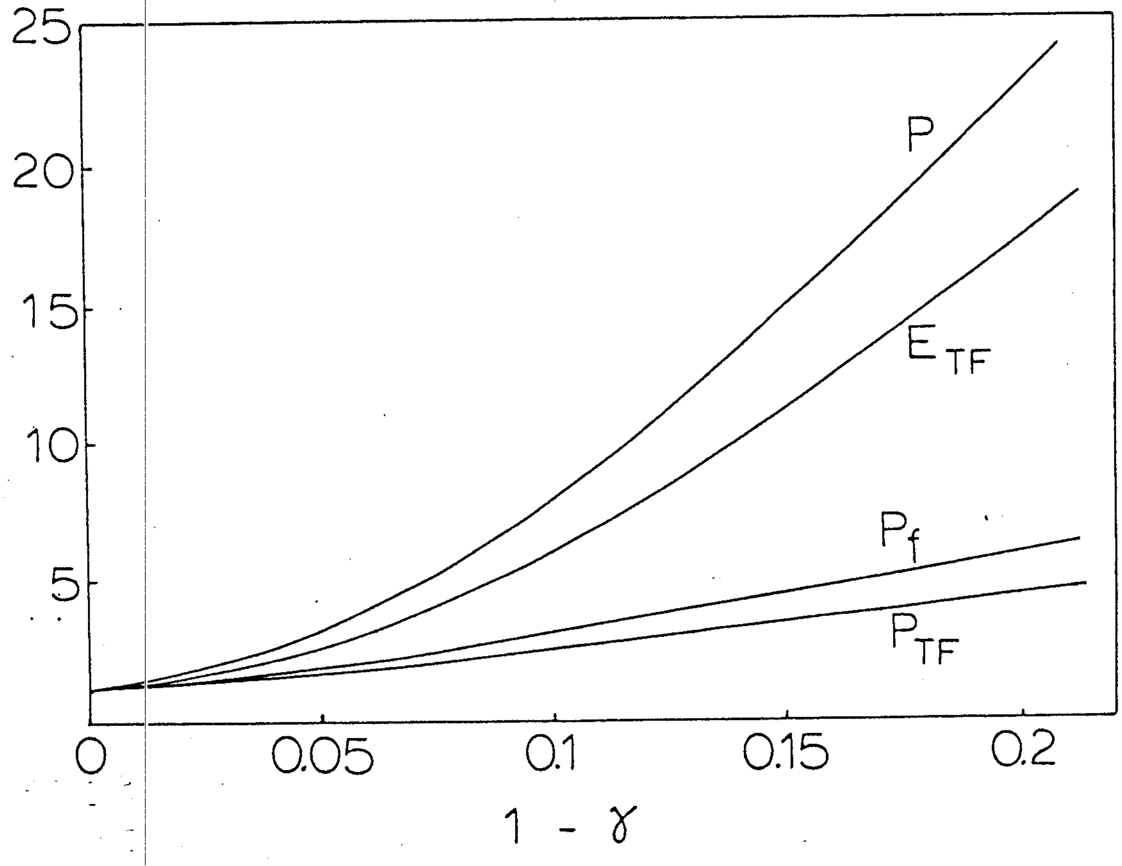

Figure 4.1.1 Normalized Values of P_{TF}, P_f, E_{TF} and P as Functions of $1-\gamma$ for $P_{wall} = 8$ MW/m^2.

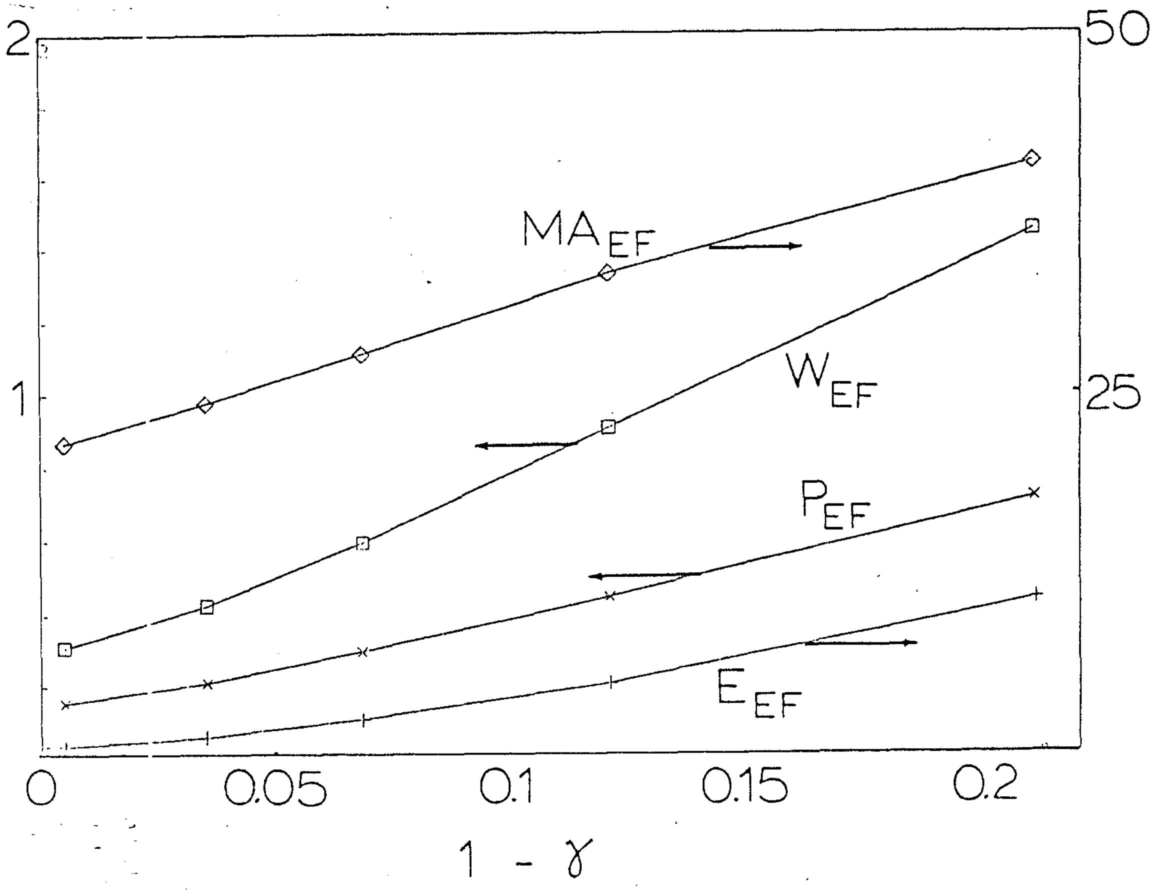

Figure 4.1.2 Normalized Values of E_{EF}, P_{EF}, W_{EF} and MA_{EF} as Functions of $1-\gamma$ for $P_{wall} = 8$ MW/m^2.

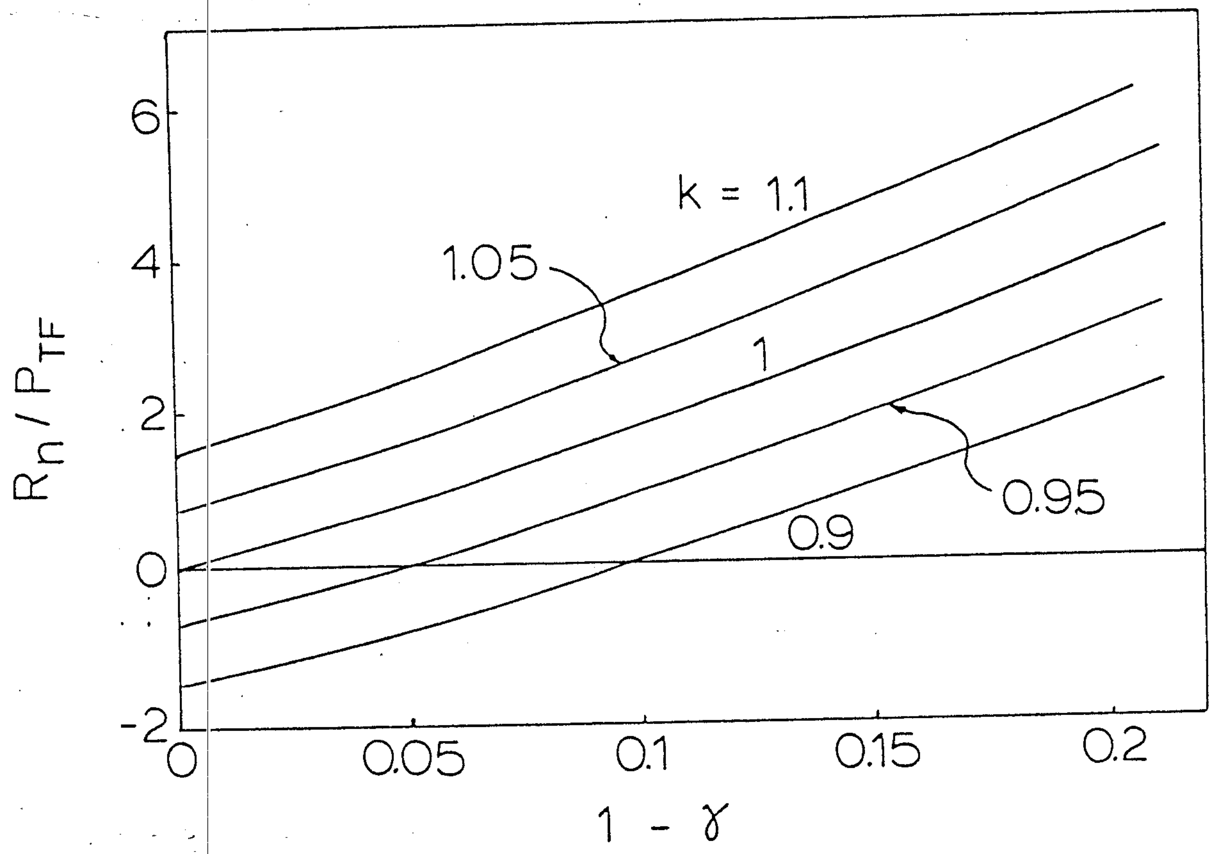

Figure 4.1.3 Ratio of Generation Rate of Excess Neutrons and Resistive Power in TF Coil as Function of $1 - \gamma$ for $P_{wall} = 8$ MW/m^2. (arbitrary units)

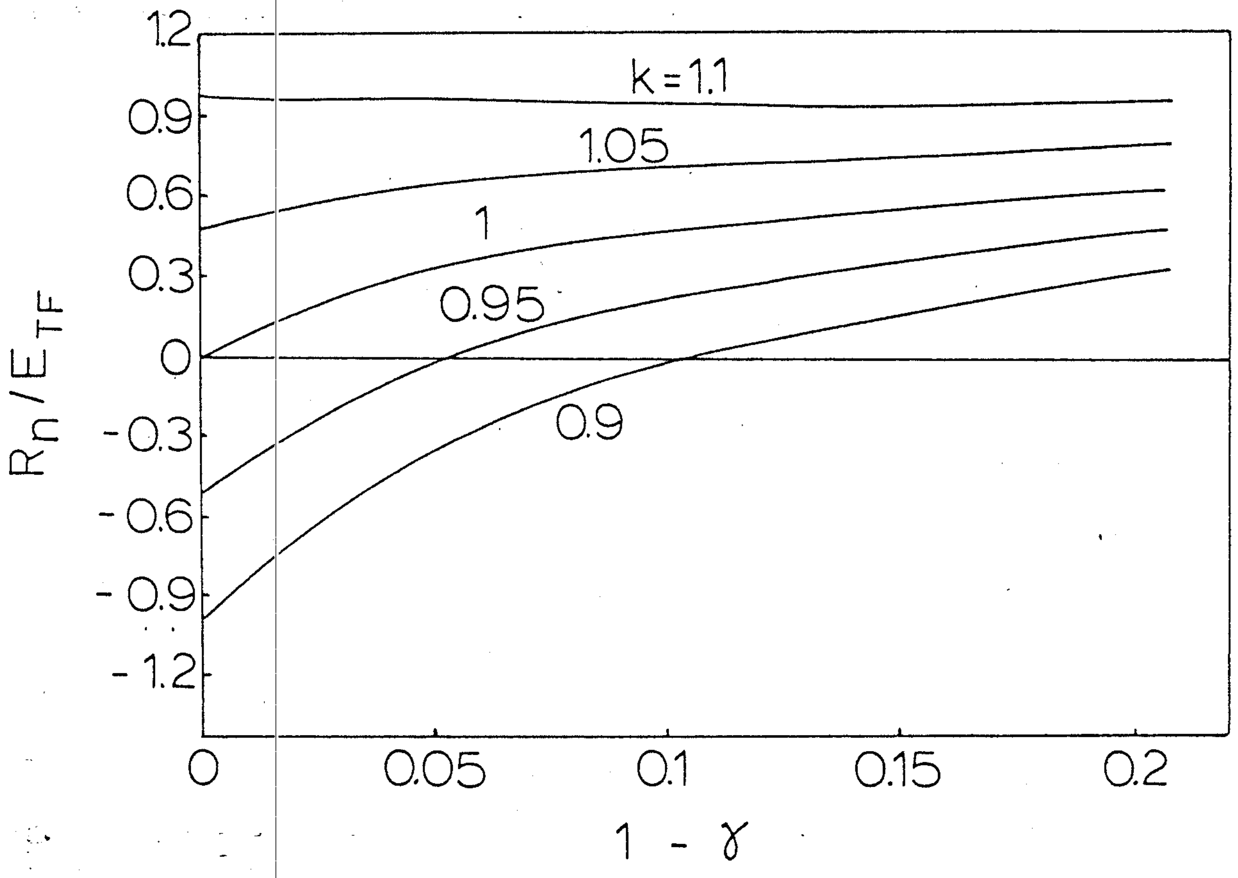

Figure 4.1.4 Ratio of Generation Rate of Excess Neutrons and Stored Energy in TF Coil as Function of $1 - \gamma$ for $P_{wall} = 8$ MW/m^2. (arbitrary units)

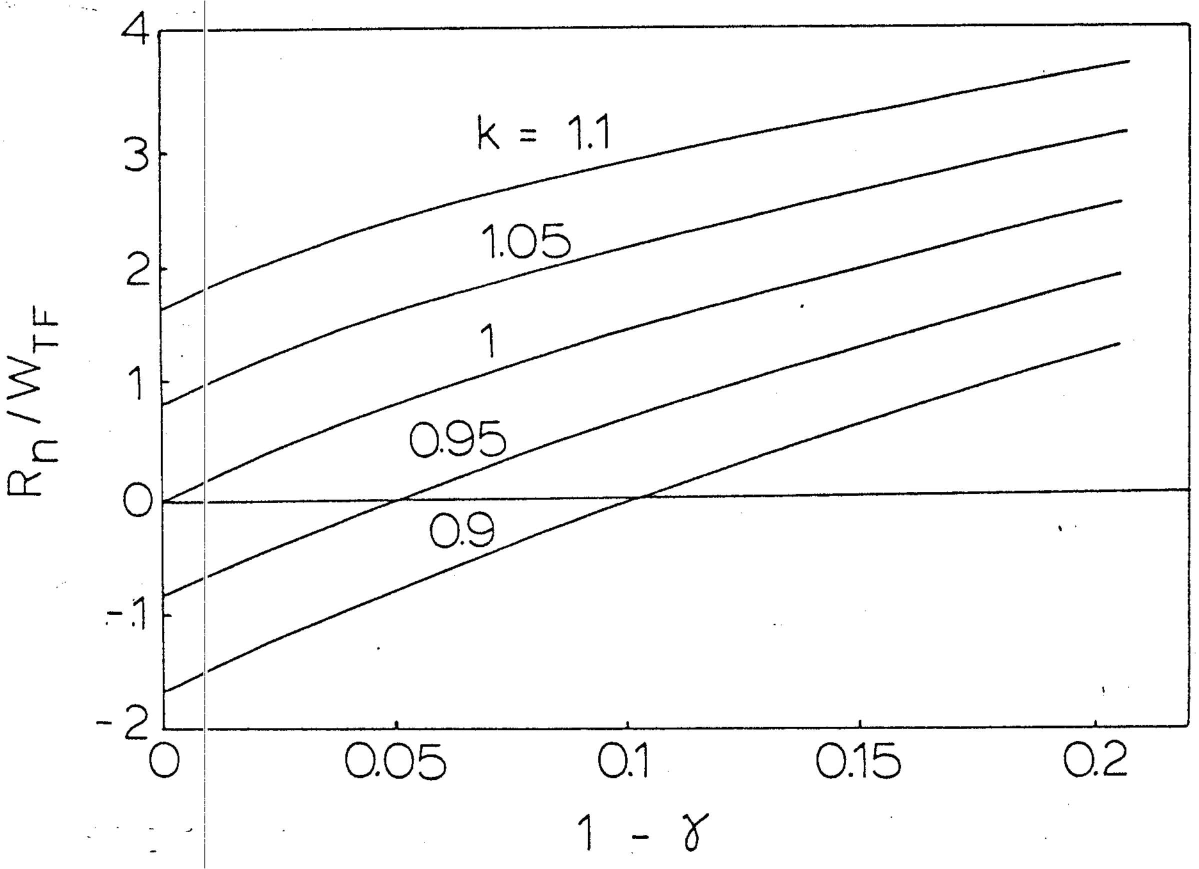

igure 4.1.5 Ratio of Generation Rate of Excess Neutrons and Weight of TF Coil as Function of $1-\gamma$ for $P_{wall}=8$ MW/m^2. (arbitrary units)

4.2 Scoping of the Effect of Blanket/Shield on Reactor Size

In this section the effect of the blanket/shield on the reactor is studied.

The effect of the blanket size on the tritium breeding ratio is outside the scope of this report. The effect of varying the thicknesses of the blanket region, the first wall, the multiplier and the reflector on the tritium breeding is hard to estimate. An attempt to reach a model for the tritium breeding ratio as a function of some of the parameters that describe the blanket/shield region was unsuccessful. However, some comments can be made in the tradeoff between blanket size (which determines the tritium breeding) and the plasma tritium breeding margin $1 - \gamma$.

Table 4.2.1 shows the parametric scan for a resistive tokamak with fixed wall loading of $P_{wall} == 8$ MW/m^2 ($\gamma = 0.93$), and $\sigma_{TF} = 150$ MPa as a function of the thickness of the blanket thickness in the inboard side of the tokamak Δ_i. The scrape off, first wall, second wall and multiplier region is ~ 0.21 m. The thickness of the blanket/shield region is varying in Table 4.2.1 from 0.19 to 0.39. As Δ_i is decreased from the base case of $\Delta_i = 0.29$ m to $\Delta_i = 0.19$ m, the net result in the machine size is a $\sim$ 10% reduction in major radius and resistive power and $\sim$ 25% decrease in fusion power, weight of toroidal field magnet and stored energy. Increasing Δ_i to $\Delta_i = 0.39$ m has approximately the opposite effect.

On the other hand, reduction of Δ_i has a fairly large effect on the tritium breeding ratio. In a cylindrical one dimensional calculation, assuming STARFIRE blanket [1] with 60% solid density, the tritium breeding ratios are $k =$

1.090, 1.134 and 1.165 for $\Delta_i = 0.19$, 0.29 and 0.39 m, respectively.

Table 4.2.2 shows the results of varying the thickness of the outer blanket region (including reflector), Δ_o. The influence of Δ_o on the design are very small.

Similarly, Table 4.2.3 shows the machine designs when Δ_{top}, the thickness of the blanket at the location that corresponds to a major radius equal to the location of the plasma major radius, is varied. There are very small perturbations on the main machine parameters.

The parameters in Tables 4.2.1-4.2.3 have been calculated assuming $P_{wall} = 8$ MW/m^2 with $\gamma = 0.93$. The tritium breeding characteristics of the machine are changing as the thickness of the blanket at different locations is varying.

From Tables 4.2.1-4.2.3, is can be concluded that only the thickness of the inboard blanket has a relatively strong effect on the machine size. The question of whether it is advantageous to reduce the size of the inner blanket by operating in DD-DT mode is addresed.

For calculational purposes, assume that about 15% of the tritium, breeding occurs in the inboard side of the blanket. Also assume that the size of the inboard blanket does not affect significantly the breeding done elsewhere. Then if the size of the blanket is reduced by 0.10 m, the net tritium breeding is reduced by $0.15 \times (1.134 - 1.090) = 0.0066$. For *AFTR* type devices, reduction of the size of the blanket by 0.10 m results in a reduction in major radius of 0.44 m, or $\sim 10\%$ (Table 4.2.1).

In order to bring the tritium breeding back up to where it was before, it is necessary to increase the plasma tritium breeding ratio by the same number. From Table 4.1.2,

$$\frac{\Delta\gamma/\gamma}{\Delta R/R} \sim 2.8$$

In order to increase the plasma tritium breeding margin by 0.0066, the major radius has to increase by approximately

$$\Delta R \sim \frac{1}{2.8}\frac{\Delta\gamma}{\gamma}R \sim 0.20\text{m}$$

Therefore, it is advantageous to decrease the breeding in the throat of the magnet, as the increase due to larger required γ is smaller than the decrease of the magnet due to decreased distance between the plasma and the toroidal field coil. This result is due to the relatively minor contribution to the total breeding from the inner blanket. However, reducing the size of the inboard blanket would have implications for the lifetime of the insulation of the magnet. The implications are beyond the scope of this work.

Table 4.2.1

Parametric Scans vs. Thickness of Inboard Blanket/shield, Δ_i

$P_{wall} = 8$ MW/m^2 ($\gamma = 0.93$), $\sigma_{TF} = 150$ MPa

Δ_i(m)	0.19	0.29	0.39
A	4.05	4.07	4.06
R (m)	4.45	4.89	5.28
a (m)	1.1	1.2	1.3
B (T)	8.66	8.5	8.32
I (MA)	10.4	11.1	11.8
P (m^2 T^4)	26.0	28.4	30.7
P_f (GW)	2.37	2.84	3.33
σ_{hoop}	0.148	0.149	0.148
T_R(GN m)	3.03	3.65	4.31
W_{TF}(Gg)	5.23	6.49	7.86
E_{TF}(GJ)	13.6	17.5	21.7
P_{TF}(MW)	550	610	664
$W_{blanket}$(Gg)	0.12	0.167	0.223
E_{OH}(GJ)	1.73	1.96	2.26
P_{OH}(MW)	57.6	55.2	56.1
E_{EF}(GJ)	2.28	2.73	3.22
P_{EF}(GW)	0.223	0.253	0.284
W_{EF}(Gg)	0.649	0.733	0.82
MA_{EF}(MA-turn)	26.4	28.2	30.1

Table 4.2.2

Parametric Scans vs. Thickness of Outboard Blanket/Shiled, Δ_o

$P_{wall} = 8$ MW/m^2 ($\gamma = 0.93$), $\sigma_{TF} = 150$ MPa

Δ_o (m)	0.39	0.59	0.79
A	4.0	4.07	4.0
R (m)	4.8	4.89	5.0
a (m)	1.2	1.2	1.25
B (T)	8.44	8.5	8.34
I (MA)	11.2	11.1	11.5
P (m^2 T^4)	28.5	28.4	29.5
P_f (GW)	2.80	2.84	3.02
σ_{hoop}(MPa)	0.152	0.149	0.144
T_R(GN m)	3.16	3.65	4.17
W_{TF}(Gg)	5.92	6.49	7.33
E_{TF}(GJ)	16.3	17.5	18.8
P_{TF}(MW)	606	610	614
$W_{blanket}$(Gg)	0.135	0.167	0.209
E_{OH}(GJ)	1.96	1.96	2.11
P_{OH}(MW)	56.4	55.2	57.3
E_{EF}(GJ)	2.48	2.7	2.99
P_{EF}(GW)	0.283	0.298	0.318
W_{EF}(Gg)	0.567	0.599	0.641
MA_{EF}(MA-turn)	27.4	27.9	28.7

Table 4.2.3

Parametric Scan vs. Thickness of blanket

at Location of the Plasma Major Radius, Δ_{top}

$P_{wall} = 8$ MW/m^2 $(\gamma = 0.93)$, $\sigma_{TF} = 150$ MPa

Δ_{top} (m)	0.14	0.29	0.43
T_R(GN m)	3.65	3.65	3.65
W_{TF} (Gg)	6.31	6.5	6.7
E_{TF} (GJ)	11.2	11.9	12.7
P_{TF} (MW)	587.	610.	628.
$W_{blanket}$ (Gg)	0.14	0.167	0.195
E_{OH} (GJ)	1.94	1.94	1.94
P_{OH} (MW)	54.1	54.1	54.1
E_{EF} (GJ)	2.51	2.7	2.9
P_{EF} (GW)	0.284	0.298	0.313
W_{EF} (Gg)	0.573	0.6	0.626
MA_{EF} (MA)	26.4	27.9	29.3

4.3 Parametric Analysis for Constant $\gamma = 0.93$

In this section, parametric scans are performed to illustrate the different tradeoffs. The assumptions in the parametric code are shown in Table 4.3.1.

The stresses in the throat of the magnet are $\sigma_{TF} = 150$ MPa. The stresses in the ohmic heating central transformer are $\sigma_{OH} = 140$ MPa, with the OH transformer at the end of the burn pulse biased half way in the opposite direction than prior to initiation. The burn pulse length of the base case is assumed to be 100 seconds, limited by the OH transformer, with a peak electron temperature of 20 keV.

The plasma elongation has been chosen to be $\kappa = b/a = 1.5$ and the plasma safety factor $q = 2.5$ at the plasma edge and $q = 0.9 - 1$ at the plasma center. The plasma triangularity resulting from the poloidal field system is $0.05 \leq \delta \leq 0.2$.

The parameters of the equilibrium field system are calculated using the method described in section 3.3. The same parameters that optimize the vertical field system are assumed (section 4.5.2).

The distance between the toroidal field coil and the plasma in the midplane in the throat of the magnet, δ_i is assumed to be $\delta_i = 0.50$ m. This allows for 0.36 m of blanket, shield, first wall and multiplier space plus 0.14 m for scrape-off region . On the outboard side of the plasma, the distance between the plasma and the toroidal field coil is $\delta_o = 0.80$ m. The larger distance allows for ~ 0.66 m of blanket/shield modules located between the toroidal field coil and the first wall.

In this section, the tradeoffs between the different parameters of the machine engineering and plasma physics are done keeping the neutron wall loading and $1 - \gamma$ constant. This is to keep the nuclear characteristics of the machines constant (with constant thickness of the blanket/shield region and with constant wall loading, the nuclear properties of the machine should remain constant).

Keeping the wall loading constant means that the plasma performance P has to vary. This is because a single parameter, either P_{wall} or P, plus the aspect ratio A determines the design parameters. The fact that P is varying implies that for fixed γ and for fixed wall loading P_{wall} the plasma $Q = P_{fusion}/P_{heating}$ is varying (or, if the plasma is overignited, the amount of biasing required for thermal equilibrium according to the empirical scaling law described in chapters 2 and 3). However, due to the unknowns in the scaling of energy confinement for plasmas of this size and operating at these temperatures, keeping the wall loading fixed is a better base for the parametric scans than the plasma performance parameter P. Although P is varying, γ and P_{wall} do not vary.

The lifetime of the magnet is determined by the survivability of the insulation in the inboard side of the magnet. The allowable fast neutron fluence (section 3.3.2) is 10^{24} to 10^{25} n/m^2 [2]. The fast neutron flux at the inner edge of the inner blanket is required for an estimate of magnet lifetime. That flux has not yet been determined.

Table 4.3.2 shows the results of the parametric scan vs. aspect ratio. The tensile stresses in the throat of the magnet are kept constant and the neutron wall loading is also kept constant. This table therefore shows the possible variations in machine characteristics for fixed engineering and nuclear properties. The aspect ratio for the machine is varied between $A \sim 6$ to $A \sim 3$. The magnetic field on the plasma axis varies between 11.5 and 7 T. If the designs in Table 4.3.2 where run in DT, the neutron wall loading would be $P_{wall} = 25$ MW/m^2. For $\gamma = 0.93$ the corresponding wall loading would be 8 MW/m^2 and for $\gamma = 0.8$ the corresponding wall loading would be $P_{wall} = 2.8$ MW/m^2. In Table 4.3.2, I is the plasma current, W_{TF} is the weight of the TF coil, P_{TF} is the resistive power of the TF coil, E_{TF} is the stored energy in the EF coil, P_{EF} is the resistive power of the EF coils, E_{EF} is the stored energy in the EF coils, MA_{EF} is the Ampere turns of the EF coils and W_{EF} is the weight of the EF coils. T_R is the torque due to the interaction between the poloidal field and the current in the TF coil. P_f is the total fusion power determined for $\gamma = 0.93$.

The fixed wall loading and fixed constant stresses result in varying values of the plasma performance P. Thus the machines in Table 4.3.2 (and in subsequent tables) do not have constant margins of performance. For fixed wall loading, the performance P increases with decreasing field (or increasing minor radius). From Table 4.3.2, the plasma performance P for a fixed wall loading is decreasing with increasing aspect ratio A. The reason for this is that the wall loading is determined by

$$P_{wall} \sim \frac{n^2 R a^2}{R a} \sim \frac{n^2 a^2}{a} \sim \frac{\beta^2 a^2 B^4}{a} \sim \frac{P}{a}$$

Therefore, for smaller minor radius a, (larger aspect ratio), the plasma performance P has decreased. The fusion power decreases with increasing aspect ratio, as

$$P_f \sim n^2 R a^2 \sim (P) R$$

and the major radius R remains approximately constant while P decreases.

The plasma major radius remains approximately constant because of the constraint on the stresses in the throat of the magnet: as the aspect ratio increases with approximately fixed plasma major radius, the throat cross sectional area increases sufficiently (due to smaller minor radius) to balance the increased loads due to the increased magnetic field necessary to keep P_{wall} constant.

The major radius is minimized at $a \sim 1$ m. The stored energy in the magnet is also minimized for $a \sim 1$ m.

The weight of the magnet W_{TF} increases monotonically with decreasing aspect ratio. The resistive power decreases with aspect ratio for $A \geq 4$ and remains approximately constant for $A \leq 4$. The EF system characteristics (weight, stored energy, resistance power and Ampere turns) remain approximately constant over the range $A \geq 3.5$, but the requirements increase for aspect ratios lower than $A \sim 3.5$. The optimum aspect ratio results, therefore, from a tradeoff between the weight of the magnet and the resistive power dissipation. An aspect ratio of $A = 4$ has been chosen as a compromise between minimum resistive power dissipation and slowly increasing weight of the magnet.

The choice of aspect ratio is reached in order to minimize the operation costs and capital cost of the plant. With $Q_{TF} \sim 3 - 4$ (Q_{TF} = Fusion power/electricity required for driving the magnet systems), it is unlikely that this type of device would be a commercial machine for selling fusion power. (The applications of this type of device are as a materials test reactor or as supplier of tritium for other DT reactors.) It is possible, however, to obtain larger values of Q_{TF} by operating at even lower aspect ratios. For $A = 3.3$, for example,

$Q_{TF} = 4.5$ (as opposed to $Q_{TF} = 3$ at $A = 4$). However, the capital expense of the machine with $A = 3.3$ is significantly larger than the base case $A = 4$ (weight of TF increases by a factor of 1.35, stored energy up by a factor of 1.13 while the resistive power remains approximately constant due to increased requirements in the EF system).

The nuclear characteristics of the machine designs, shown in Table 4.3.2 are approximately constant, as the neutron wall loading and the radial builds of the shield and/or blankets have been kept fixed.

Tables 4.3.3 and 4.3.4 show the results from the parametric scans for different values of P_{wall} than Table 4.3.2. Table 4.3.3 is for $P_{wall} = 4.8$ MW/m^2 for $\gamma = 0.93$ and Table 4.3.4 is for $P_{wall} = 11.2$ MW/m^2 for $\gamma = 0.93$. Again, most of the parameters describing the system are approximately constant for $5 \leq A \leq 3.5$ with the exception of the plasma performance P, the fusion power P_f, the weight of the magnet W_{TF} and the resistive power R_{TF}. P_f, P and P_{TF} are optimized with decreasing aspect ratio, while W_{TF} is optimized with $A \simeq 5$. Again $A \simeq 4$ is a compromise between minimum weight, minimum resistive power, and increasing P and P_f aspect ratio for varying wall loadings is $A \simeq 4$.

Table 4.3.5 shows the results from the parametric scan with A = 4 and varying wall loadings. This table indicates the increase in machine size with increasing wall loading. For a factor of 1.6 increase in wall loading (12.8 MW/m^2 vs. 8 MW/m^2 for $\gamma = 0.93$ the weight of the machine increases by a factor of ~ 1.75. The stored energy increases by a factor of 2 and the resistive power increases by a factor of 1.4.

Alternatively, the machines in Table 4.3.5 can be considered as machines with constant wall loading and varying γ. This is shown in Table 4.3.5.b. The value of γ can be varied to alter the specific fusion power density $P_f/\beta^2 B^4$ and keep the wall loading fixed. The value of the tritium breeding ratio $1-\gamma$ over the range of these parametric scan varies from $1-\gamma = 0.035$ for the smallest machine (R = 4.03m, P_{TF} = 437MW, E_{TF} = 9.3 GJ) to $1-\gamma = 0.11$ for the largest machine (R = 6.1m, P_{TF} = 830 MW, E_{TF} = 34.2 GJ). There is a very large increase in machine size with moderate increases of $1-\gamma$. This is due to the fact, shown in Chapter 2, that the fusion power density decreases very fast with increasing $1-\gamma$. It should be noted that the neutronic or breeding characteristics of the designs in Table 4.3.5.b are not comparable, as the blanket/shield thickness and P_{wall} are kept constant while γ is allowed to vary. In Section 4.2 the inner blanket would be decreased in size to indicate the relaxed requirements in tritium breeding.

Table 4.3.6 shows the machine design as the burn-time is allowed to vary. It is assumed that the current drive is provided by an OH transformer. The wall loading is P_{wall} = 8 MW/m^2 for $\gamma = 0.93$. There are small effects on the machine size when the requirements for an OH transformer capable of up to 100 s of burn plus all inductive requirements. The OH transformer starts to be affected by the resistive volts seconds for a burn-pulse of $\sim 10^3$ s and the reactor itself increases substantially in size for 10^4 s of burn. Between no resistive volt seconds for the burn and up to 10^4 s of OH transformer driven burn, the machine weight and stored energy in the TF magnet in the TF system increase by a factor of ~ 3, and the resistive power by a factor of 2.

Table 4.3.7 shows the results of the parametric scan for fixed wall loading ($P_{wall} = 8$ MW/m^2 for $\gamma = 0.93$) for varying the plasma β scaling. The parameter $c_\beta = \beta \times A$ is varied between 0.15 to $c_\beta = 0.30$. As c_β is increased from $c_\beta = 0.15$ to $c_\beta = 0.25$, the stored energy in the magnet decreases by a factor of $\sim$ 4, the weight decreases by a factor of $\sim$ 3 and the resistive power by a factor of $\sim$ 2. The fusion power decreases by a factor of $\sim$ 2.5. Values of c_β lower than 0.15 result in very large machine dimensions. The choice of c_β ($c_\beta \sim 0.25$) is optimistic, resulting in values of beta poloidal close to the aspect ratio.

Table 4.3.8 shows the results of the parametric scan with constant wall loading ($P_{wall} = 8$ MW/m^2 for $\gamma = 0.93$) vs. varying tensile stresses in the throat of the magnet. The size of the machine is strongly affected by the assumed tensile stress in the throat. If $\sigma_{TF} = 240$ MPa, the major radius is under 4m. For $\sigma_{TF} = 150$ MPa (the base case), the major radius increases to under 5m. For $\sigma_{TF} = 115$ MPa, $R \simeq 6.6$ m. The resistive power of the TF magnet does not increase as fast, while the stored energy and weight increases by about a factor of 3.

Table 4.3.1

Constrains for the Parametric Scans

β_TA	0.25
q	2.5
$\kappa = b/a$	1.5
burn pulse lengths (s)	100
σ_{TF} (MPa)	150
σ_{OH}(MPa)	150
δ_i(m)	0.50
δ_o(m)	0.80
T_{eo}	20

Table 4.3.2

Parametric Scan for $\sigma_{TF} = 150$ MPa and

$P_{wall} = 8$ MW/m^2 (at $\gamma = 0.93$)

A	6.11	4.74	4.07	3.64	3.37
R (m)	4.89	4.74	4.89	5.1	5.38
a (m)	0.8	1.0	1.2	1.4	1.6
B (T)	11.5	9.6	8.5	7.73	7.19
I (MA)	6.4	8.82	11.1	13.3	15.4
P (m^2 T^4)	18.9	23.6	28.4	33.0	37.7
P_f (GW)	1.89	2.29	2.84	3.46	4.16
P_{TF}(MW)	860	667	610	590	587
σ_{hoop}(MPa)	0.164	0.153	0.149	0.145	0.144
T_R(GN m)	4.63	3.7	3.65	3.79	4.10
W_{TF}(Gg)	5.47	5.67	6.49	7.53	8.74
E_{TF}(GJ)	22.0	17.8	17.5	18.2	19.8
$W_{blanket}$(Gg)	0.12	0.139	0.167	0.199	0.236
E_{OH}(GJ)	1.45	1.66	1.96	2.38	2.83
P_{OH}(MW)	59.6	56.7	55.2	57.9	58.9
E_{EF}(GJ)	3.53	2.62	2.7	3.01	3.47
P_{EF}(GW)	0.286	0.288	0.298	0.322	0.355
W_{EF}(Gg)	0.812	0.577	0.599	0.649	0.716
MA_{EF}(MA-turn)	31.6	27.6	27.9	29.2	30.9

Table 4.3.3

Parametric Scan for $\sigma_{TF} = 150$ MPa
and $P_{wall} = 4.8$ MW/m^2 (at $\gamma = 0.93$)

A	7.1	4.89	4.03	3.56	3.26
R (m)	4.26	3.91	4.03	4.27	4.56
a (m)	0.6	0.8	1.0	1.2	1.4
B (T)	11.7	9.07	7.79	7.0	6.44
I (MA)	4.15	6.45	8.55	10.6	12.5
P (m^2 T^4)	8.51	11.3	14.2	17.0	19.8
P_f (GW)	0.74	0.91	1.17	1.49	1.85
P_{TF}(MW)	729	488	437	428	429
σ_{hoop}(MPa)	0.158	0.141	0.137	0.135	0.134
T_R(GN m)	2.98	2.04	1.88	1.98	2.15
W_{TF}(Gg)	3.8	3.67	4.25	5.02	6.09
E_{TF}(GJ)	14.6	9.76	9.31	9.87	10.83
$W_{blanket}$(Gg)	0.0853	0.0974	0.12	0.148	0.179
E_{OH}(GJ)	0.912	1.07	1.28	1.55	1.88
P_{OH}(MW)	58.2	58.7	55.9	55.2	55.3
E_{EF}(GJ)	3.13	1.63	1.64	1.85	2.18
P_{EF}(GW)	0.308	0.215	0.22	0.241	0.27
W_{EF}(Gg)	0.6	0.428	0.44	0.483	0.541
MA_{EF}(MA-turn)	32.7	24.7	24.8	26.1	27.9

Table 4.3.4

Parametric Scan for $\sigma_{TF} = 150$ MPa and

$P_{wall} = 11.2$ MW/m^2 (at $\gamma = 0.93$)

A	7.86	5.49	4.55	4.03	3.68
R (m)	6.29	5.49	5.46	5.64	5.88
a (m)	0.8	1.0	1.2	1.4	1.6
B (T)	14.2	11.2	9.78	8.85	8.18
I (MA)	5.99	8.78	11.3	13.6	15.9
P (m^2 T^4)	26.5	33.1	39.7	46.3	52.9
P_f (GW)	3.39	3.71	4.45	5.34	6.37
σ_{hoop}(MPa)	0.192	0.169	0.161	0.157	0.154
T_R(GN m)	10.8	6.48	5.47	5.78	6.04
W_{TF}(Gg)	8.62	7.43	8.01	9.1	10.5
E_{TF}(GJ)	49.4	30.3	27.5	27.4	28.9
P_{TF}(MW)	1536	967	820	764	746
$W_{blanket}$(Gg)	0.153	0.16	0.186	0.218	0.256
E_{OH}(GJ)	1.84	2.0	2.34	2.75	3.25
P_{OH}(MW)	56.9	55.6	55.7	55.5	56.9
E_{EF}(GJ)	9.37	4.12	3.73	3.97	4.44
P_{EF}(GW)	0.595	0.377	0.36	0.379	0.41
W_{EF}(Gg)	1.16	0.749	0.723	0.762	0.826
MA_{EF}(MA-turn)	43.8	31.4	30.3	31.0	32.4

Table 4.3.5

(a) Parametric Scan vs. P_{wall} for $\gamma = 0.93$, $\sigma_{TF} = 150$ MPa

P_{wall} (MW/m^2)	12.8	10.4	8.0	6.4	4.8
A	3.84	3.93	4.07	4.05	4.03
R (m)	6.14	5.5	4.89	4.45	4.03
a (m)	1.6	1.4	1.2	1.1	1.0
B (T)	8.64	8.58	8.5	8.19	7.79
I (MA)	16.0	13.6	11.1	9.84	8.55
P (m^2 T^4)	60.5	43.0	28.4	20.8	14.2
P_f (GW)	7.58	4.83	2.84	1.89	1.17
σ_{hoop}(MPa)	0.159	0.154	0.149	0.142	0.137
T_R(GN m)	7.23	5.23	3.65	2.71	1.88
W_{TF}(Gg)	11.4	8.7	6.49	5.28	4.25
E_{TF}(GJ)	34.2	25.0	17.5	13.0	9.3
P_{TF}(MW)	830	720	610	522	437
$W_{blanket}$(Gg)	0.266	0.213	0.167	0.142	0.12
E_{OH}(GJ)	3.39	2.67	1.96	1.65	1.28
P_{OH}(MW)	54.5	56.8	55.2	58.6	55.9
E_{EF}(GJ)	4.95	3.71	2.7	2.13	1.64
P_{EF}(GW)	0.437	0.364	0.298	0.257	0.22
W_{EF}(Gg)	0.88	0.733	0.599	0.517	0.44
MA_{EF}(MA-turn)	33.1	30.6	27.9	26.3	24.8

(b) Values of γ for Constant P_{wall}

P_{wall}(MW/m^2)	8	8	8	8	8
γ	0.89	0.91	0.93	0.95	0.965
$1-\gamma$	0.11	0.09	0.07	0.05	0.035

Table 4.3.6

Parametric Scan vs. Burn Time of

for $P_{wall} = 8\ \mathrm{MW/m^2}$ ($\gamma = 0.93$), $\sigma_{TF} = 150$ MPa

t_{burn}(s)	0	100	1000	10000
A	4.0	4.07	4.06	4.06
R (m)	4.8	4.89	5.48	8.72
a (m)	1.2	1.2	1.35	2.15
B (T)	8.43	8.5	8.24	7.33
I (MA)	11.2	11.1	12.1	17.2
P ($\mathrm{m^2\ T^4}$)	28.4	28.4	31.9	50.8
P_f (GW)	2.79	2.84	3.58	9.06
σ_{hoop}(MPa)	0.145	0.149	0.168	0.229
T_R(GN m)	3.51	3.65	4.59	12.01
W_{TF}(Gg)	6.36	6.49	8.08	20.1
E_{TF}(GJ)	16.9	17.5	21.3	51
P_{TF}(MW)	597	610	681	1082
$W_{blanket}$(Gg)	0.165	0.167	0.206	0.485
E_{OH}(GJ)	1.86	1.96	3.56	16.8
P_{OH}(MW)	58.1	55.2	57.1	58.9
E_{EF}(GJ)	2.66	2.7	3.09	6.04
P_{EF}(GW)	0.295	0.298	0.327	0.519
W_{EF}(Gg)	0.594	0.599	0.659	1.05
MA_{EF}(MA-turn)	28.1	27.9	27.5	28.1

Table 4.3.7

Parametric Scan vs. $c_\beta = \beta \times A$ for
$P_{wall} = 8\ \mathrm{MW/m^2}$ ($\gamma = 0.93$), $\sigma_{TF} = 150$ MPa

c_β	0.15	0.20	0.25	0.3
A	3.97	3.93	4.07	3.93
R (m)	7.54	5.89	4.89	4.33
a (m)	1.9	1.5	1.2	1.1
B (T)	9.66	8.83	8.5	7.8
I (MA)	18.8	14.4	11.1	9.97
P (m^2 T^4)	44.9	35.4	28.4	26.0
P_f (GW)	6.94	4.26	2.84	2.30
σ_{hoop}(MPa)	0.168	0.156	0.149	0.141
T_R(GN m)	12.3	6.07	3.65	2.48
W_{TF}(Gg)	18.9	10.3	6.49	4.99
E_{TF}(GJ)	70.9	31.5	17.5	11.3
P_{TF}(MW)	1260	812	610	480
$W_{blanket}$(Gg)	0.378	0.242	0.167	0.139
E_{OH}(GJ)	4.99	3.0	1.96	1.58
P_{OH}(MW)	58.0	56.7	55.2	56.2
E_{EF}(GJ)	6.99	4.04	2.7	2.13
P_{EF}(GW)	0.558	0.389	0.298	0.257
W_{EF}(Gg)	1.12	0.781	0.599	0.516
MA_{EF}(MA-turn)	35.4	30.9	27.9	26.9

Table 4.3.8

Parametric Scan vs. σ_{TF} for Fixed Wall-Loading

$P_{wall} = 8$ MW/m^2 ($\gamma = 0.93$)

σ_{TF}(MPa)	210	150	100
A	4.07	4.07	4.12
R (m)	3.86	4.89	6.59
a (m)	0.95	1.2	1.6
B (T)	9.02	8.5	7.96
I (MA)	9.31	11.1	13.7
P (m^2 T^4)	22.5	28.4	37.9
P_f (GW)	1.78	2.84	5.12
σ_{hoop}(MPa)	0.205	0.149	0.107
T_R(GN m)	2.37	3.65	6.53
W_{TF}(Gg)	4.09	6.49	12.2
E_{TF}(GJ)	11.2	17.5	31.9
P_{TF}(MW)	548	610	741
$W_{blanket}$(Gg)	0.111	0.167	0.285
E_{OH}(GJ)	1.35	1.96	3.29
P_{OH}(MW)	55.5	55.2	57.7
E_{EF}(GJ)	2.2	2.7	3.91
P_{EF}(GW)	0.258	0.298	0.385
W_{EF}(Gg)	0.515	0.599	0.778
MA_{EF}(MA-turn)	30.2	27.9	27.2

4.4 Elongation Tradeoffs

In the previous sections the plasma elongation has been kept fixed at $\kappa = b/a = 1.5$. In this section the elongation is allowed to vary, while keeping the neutronics and magnet engineering constant.

In discrete coil reactor designs, the height of the magnet is determined from the use of D-shape coils [3] or bending free coils [4]. The location of the outer leg of the TF is determined by either ripple or maintenance requirements. The height of the coil is such that increased plasma elongation does not affect the location of the coil.

For a continuous magnet (such as the Bitter magnet that is being considered), the coil contour follows the outer periphery of the blanket/shield reflector. That is, it is located as close as possible to the plasma. Elongating the plasma has a direct consequence on the shape of the TF magnet and on the stresses. In this section a elongation scan is performed to find the optimum plasma elongation. As noted in Chapter 3, the plasma elongation increases the allowable plasma pressure. It is assumed that

$$\beta_T \sim \kappa \frac{1}{A}$$

The machine size is varied while keeping the wall loading and the stresses in the throat of the magnet constant. The stresses are calculated using thick shell theory [5].

Table 4.4.1 shows the results of the parametric scan for $P_{wall} = 8$ MW/m^2 with $\gamma = 0.93$ and $\sigma_{membrane} = 260$ MPa. $\sigma_{membrane}$ are the von Mises membrane stresses in the throat of the magnet. The bending in the throat of the magnet is approximately the same in the three cases. The aspect ratio has been kept approximately the same. As can be seen, the energy and the weight of the TF magnet have increased by $\sim 30\%$ when the elongation is decreased from 1.5 to 1.2. The total resistive power (EF plus TF resistive powers) however, has remained approximately constant (908 MW for $\kappa = 1.5$ and 934 MW for $\kappa = 1.2$).

The vertical field system is very significantly simplified by operating with $\kappa = 1.2$. In Table 4.4.1 I_{dipole} and $I_{quadruple}$ represent the currents in the main equilibrium field coil (dipole coil) and the shaping coil (quadruple coil). I_{dipole} and $I_{quadrupole}$ have been calculated using the results from Chapter 3. For $\kappa = 1.2$ the quadruple coil has very little current ($I_{quadrupole} \simeq 1.2$ MA). Furthermore, the dipole current also carries $\sim 25\%$ less current than for $\kappa = 1.2$ than for $\kappa = 1.5$. The total number of Ampere-turns, the stored energy, and the resistive power of the EF system have decreased by a factor of 2, making this system simpler and less expensive.

Figure 4.4.1 shows a schematic view of the TF and EF coils for the cases with $\kappa = 1.5$ and $\kappa = 1.2$. The TF magnet is slightly larger in size for the case $\kappa = 1.2$, while the EF coils have decreased substantially.

The specific tradeoffs between the EF and TF systems are beyond the scope of this report. The energy, weight and resistive power of the toroidal field system decrease with increasing elongation, while the poloidal field system becomes more complex with increasing elongation.

Table 4.4.1

Parametric Variation vs. Elongation

$P_{wall} = 8$ MW/m^2, $\gamma = 0.93$, $\sigma_{membrane} = 260$ **MPa**

κ	1.5	1.35	1.2
A	4.08	4.08	4.0
R (m)	4.89	5.1	5.4
a (m)	1.2	1.25	1.35
B (T)	8.51	8.99	9.41
I (MA)	11.1	10.8	10.9
P (m^2 T^4)	28.4	31.1	35.7
P_j (GW)	2.84	2.92	3.16
T_{TF}(GN m)	3.65	4.40	5.30
W_{TF} (Gg)	6.5	7.06	8.08
E_{TF} (GJ)	17.5	20.5	24.9
P_{TF} (MW)	610.	670.	754.
$W_{blanket}$ (Gg)	0.167	0.17	0.18
E_{OH} (GJ)	1.94	2.02	2.15
P_{OH} (MW)	54.1	56.1	57.9
E_{EF} (GJ)	2.7	1.96	1.35
P_{EF} (GW)	0.298	0.243	0.18
W_{EF} (Gg)	0.6	0.498	0.385
MA_{EF} (MA-turn)	27.9	20.9	13.0
I_{dipole} (MA)	6.62	5.94	5.26
$I_{quadrupole}$ (MA)	-7.31	-4.5	-1.27

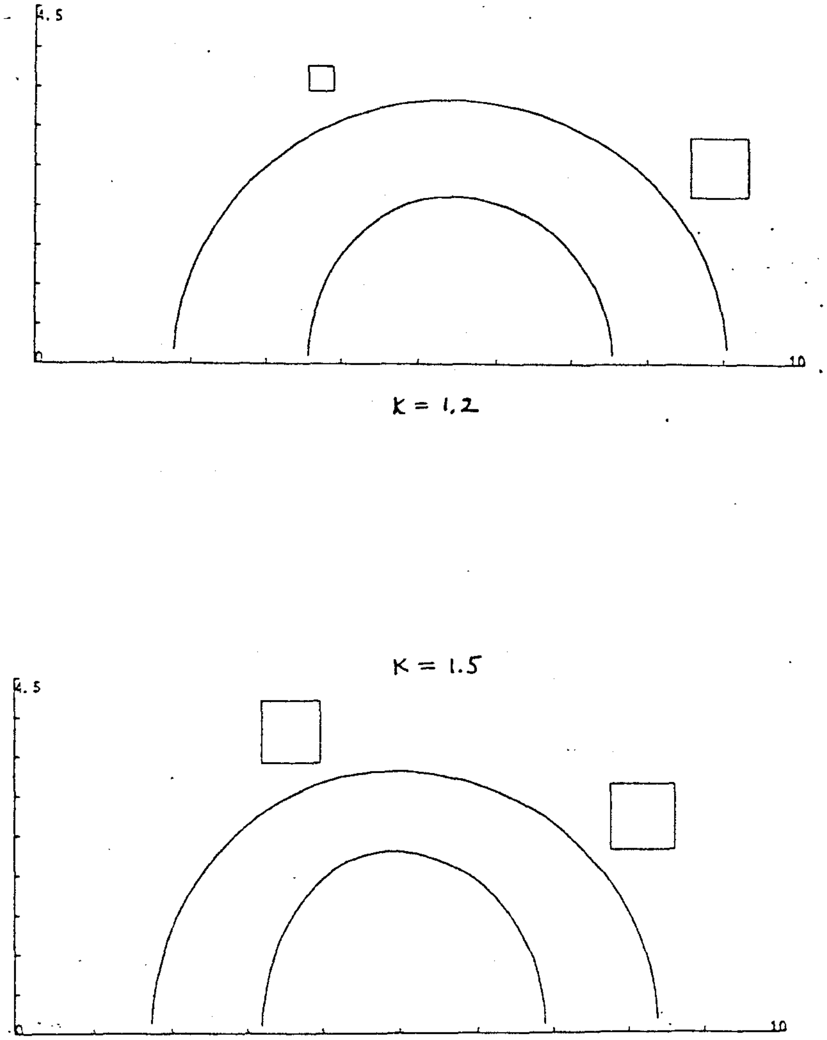

Figure 4.4.1 Schematic View of EF and TF Systems for *AFTR* with $P_{wall} = 8$ MW/m^2 ($\gamma = 0.93$) for $\kappa = 1.2$ and $\kappa = 1.5$.

4.5 Magnet Optimization

In this section, the tradeoffs for the *TF* and *EF* coils for fixed plasma requirements are analyzed.

In section 4.5.1 the toroidal field is analyzed. The height and the thickness of the outer leg of the machine are varied, and the tradeoffs are discussed.

In section 4.5.2 the poloidal field system is analyzed. The location of the *EF* coils and the current density in these coils are varied, and the tradeoffs discussed.

4.5.1 Toroidal Field Magnet

In this section the toroidal field magnet, for fixed plasma conditions, is analyzed. The plasma properties are described in sections 4.1 and 4.3 for the case referred to as base case.

Table 4.5.1 shows the main parameters of the magnet system when the width of the outer leg of the toroidal field coil, t_{out} is varied. The plasma varies somewhat due to the fact that changing the thickness of the outer leg varies the stresses in the throat of the magnet. In order to keep these stresses fixed, the plasma changes slightly. The main consequence of increasing the thickness of the outer leg of the magnet from 1 m to 2 m is that the weight of the toroidal field coil, W_{TF} increases by $\sim 40\%$, the stored energy and fusion power increase by $\sim 10\%$ while the resistive power of the toroidal field coil decreases by $\sim 15\%$. The detailed tradeoffs between increased capital costs (increases in E_{TF}, P_f, and W_{TF}) and decreased operating costs (decreased P_{TF}) is beyond the scope of this work.

Table 4.5.2 shows the main parameters of the magnet system when the height of the toroidal field coil is varied. The main variations occur in the weight of the magnet and the resistive power dissipation. Increasing the height of the magnet by 5% increases the weight of the magnet by 7% and decreases the resistive power of the magnet by 5%, while increasing the power dissipation of the EF system and its weight by 5%.

Table 4.5.1.1

Parametric Scan vs. Thickness of Outer Leg, t_{out}

$P_{wall} = 8$ MW/m^2 ($\gamma = 0.93$), $\sigma_{TF} = 150$ MPa

t_{out}(m)	1.0	1.5	2.0
A	4.0	4.07	3.98
R (m)	4.79	4.89	4.98
a (m)	1.2	1.2	1.25
B (T)	8.42	8.5	8.32
I (MA)	11.2	11.1	11.6
P (m^2 T^4)	28.4	28.4	29.5
P_f (GW)	2.78	2.84	3.01
σ_{hoop}(MPa)	0.152	0.149	0.143
T_R(GN m)	3.4	3.65	3.84
W_{TF}(Gg)	5.49	6.49	7.72
E_{TF}(GJ)	16.3	17.5	18.5
P_{TF}(MW)	656	610	573
$W_{blanket}$(Gg)	0.164	0.167	0.176
E_{OH}(GJ)	1.95	1.96	2.14
P_{OH}(MW)	56.1	55.2	59.6
E_{EF}(GJ)	2.48	2.7	2.98
P_{EF}(GW)	0.283	0.298	0.317
W_{EF}(Gg)	0.567	0.599	0.64
MA_{EF}(MA-turn)	27.7	27.9	28.5

Table 4.5.1.2

Parametric Scan vs. Height of Toroidal Field Coil

$P_{wall} = 8$ MW/m^2 ($\gamma = 0.93$), $\sigma_{TF} = 150$ MPa

h_{TF} (m)	6.33	6.63	6.93
W_{TF} (Gg)	6.05	6.5	6.95
E_{TF}(GJ)	16.6	17,5	18.5
P_{TF}(MW)	645	610	580
E_{EF}(GJ)	2.51	2.7	2.9
P_{EF}(GW)	0.284	0.298	0.313
W_{EF}(Gg)	0.573	0.60	0.63
MA_{EF}(MA)	26.4	27.9	29.3
T_R (GN m)	3.65	3.66	3.65

4.5.2 Equilibrium Field System

In this section, an optimization of the vertical field system for a specific TF design is performed. The geometry of the TF coil used in the optimization studies of the EF system are shown in Figure 3.1.1.

The optimization study has been performed as follows: for a given set of plasma parameters and a boundary for the TF coil, the optimum coil location is determined. When that location is determined, the current densities in the coils are varied. The design point for the illustrative parameters is then chosen.

It would in principle be possible to calculate the vertical field system using an equilibrium field coil for each particular case. [6]. This procedure would be tedious and time consuming. The approach used has been described in chapter 3.

There are four parameters of interest in performing the optimization study of the EF system. These are:

- Resistive losses during the plasma burn
- Energy stored at peak current
- Mass of the coils
- Ampere turns.

Figures 4.5.2.1 through 4.5.2.4 show the resistive loses, at peak conditions for $P_{wall} = 8\text{MW}/\text{m}^2$, the stored energy at peak field, the weight of the coils and the number of A-turns as functions of the locations of the *EF* coils for the TF coil outer envelope shown in Figure 3.1.1. These Figures show contours of constant resistive power, stored energy, weight and MA-turns of the vertical field system as the locations of the main and shaping EF coils are varied. The coordinate h_{main} represents the lowest point of the main EF coil, and the ordinate $R_{shaping}$ represents the point of minimum major radius of the shaping coil (see Figure 3.1.1). It is assumed that the current density in the coils is $j_1 = j_2 = 1.2 \times 10^7$ A/m^2. In Figures 4.5.2.1 through 4.5.2.4 it is assumed that the major radius of the main coil, R_1 and the height of the shaping coil h are such that the clearance between the TF coil and the poloidal field coils is 0.1 m. The coil locations are then self-consistently determined from h_{main} and $R_{shaping}$ and the current density in the coils.

As can be seen from the figures, the optimum location of the coils is such that h_{main} is as small as possible, that is, the main equilibrium coil should be as close as possible to the midplane. The parameters of the system do not depend strongly on the location of the shaping coil. h_{main} is determined from access considerations: the coil should clear the access openings in the TF coil, and it should have sufficient clearance. From engineering considerations (described in the structures section), the clearance should be ~ 0.5 m. As the port half height is 0.5 m, then the height of the lowest point of the main EF coil is $h_{main} = 1.0$ m. The location of the shaping coil is such that it clears the inner corner, that is, $R_{shaping} \sim R_a$ (where $R_a = R - a - \delta_i$). Reducing $R_{shaping}$ has the advantage of giving the plasma a significant amount of triangularity without increasing the requirements of the EF system considerably. Access to this area without having to place the coils inside the toroidal field system is one of the advantages of resistive versus superconducting magnets.

Next, the optimum current density in each coil is determined. Figures

4.5.2.5 through 4.5.2.8 show contours of constant peak resistive power, peak stored energy, weight and number of MA-turns as functions of the current densities in the main EF coil (j_1) and in the shaping coil (j_2) for $h_{main} = 1.5$ m. The optimum in this case is not as clear: as the resistive power decreases, the stored energy and weight increase. The point $j_1 \sim j_2 \sim 1.2 \times 10^7$ MA/m^2 has been chosen as a compromise.

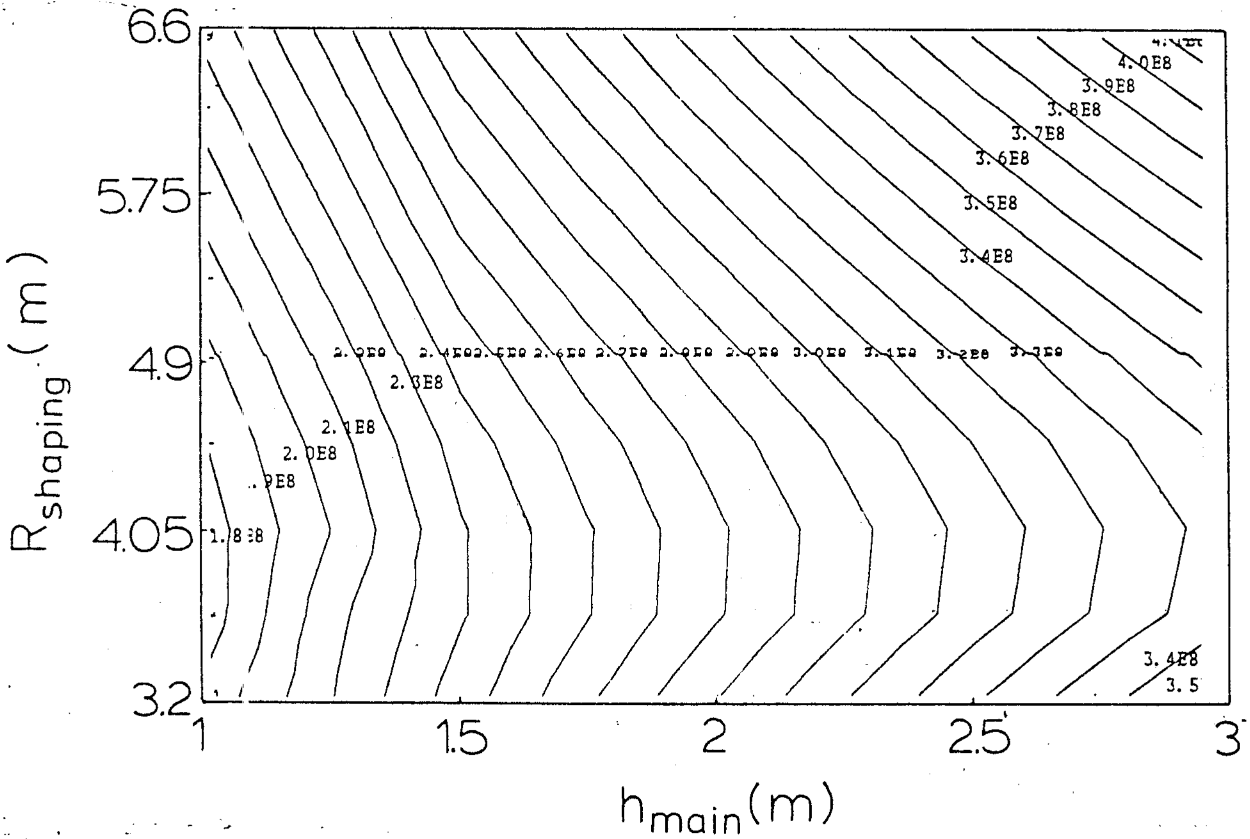

Figure 4.5.2.1 Contours of Constant Resistive Losses in EF Coil vs Locations of Coils for $j_1 = j_2 = 12$ MA/m^2.

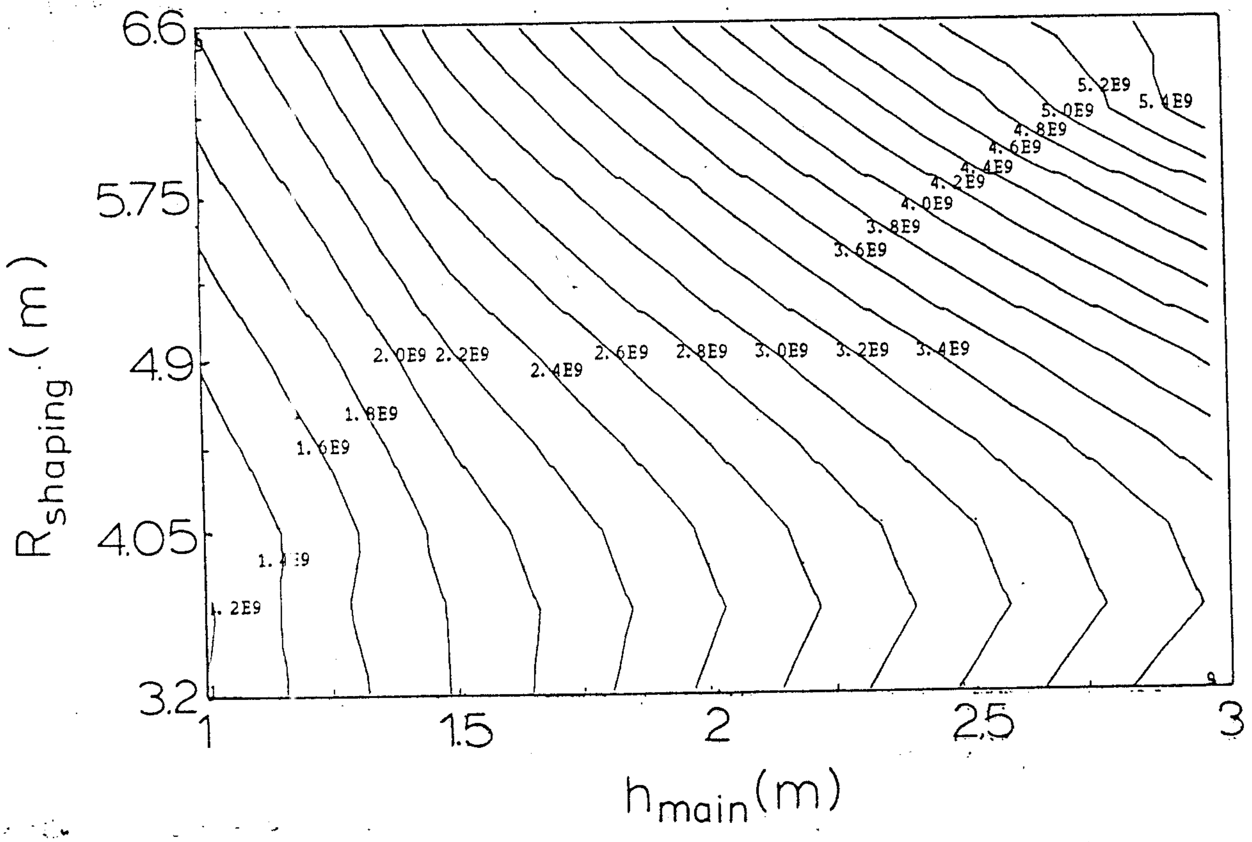

Figure 4.5.2.2 Contours of Constant Energy in EF Coil vs Locations of Coils for $j_1 = j_2 = 12$ MA/m^2.

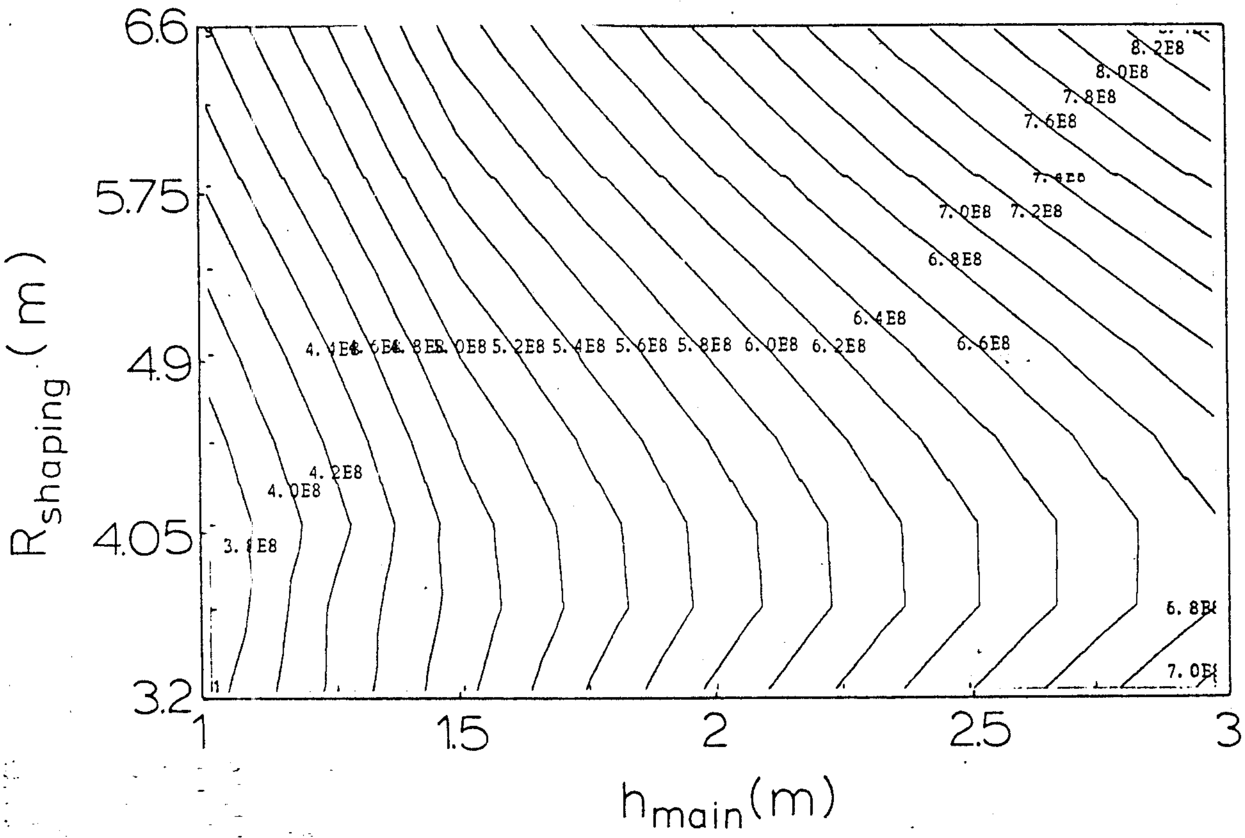

Figure 4.5.2.3 Contours of Constant Weight of EF Coil vs Locations of Coils for $j_1 = j_2 = 12$ MA/m^2.

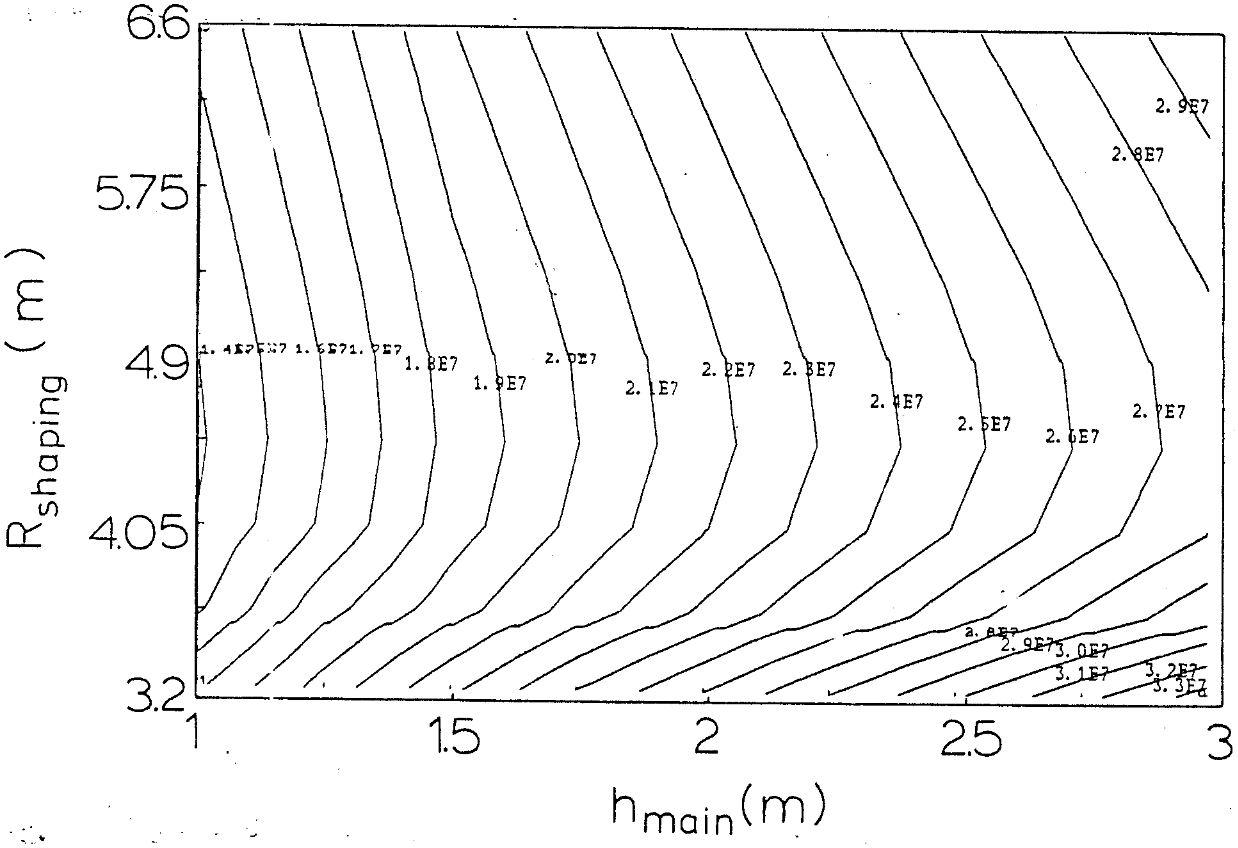

Figure 4.5.2.4 Contours of Constant Ampere-Turns in EF Coil vs Locations of Coils for $j_1 = j_2 = 12$ MA/m^2.

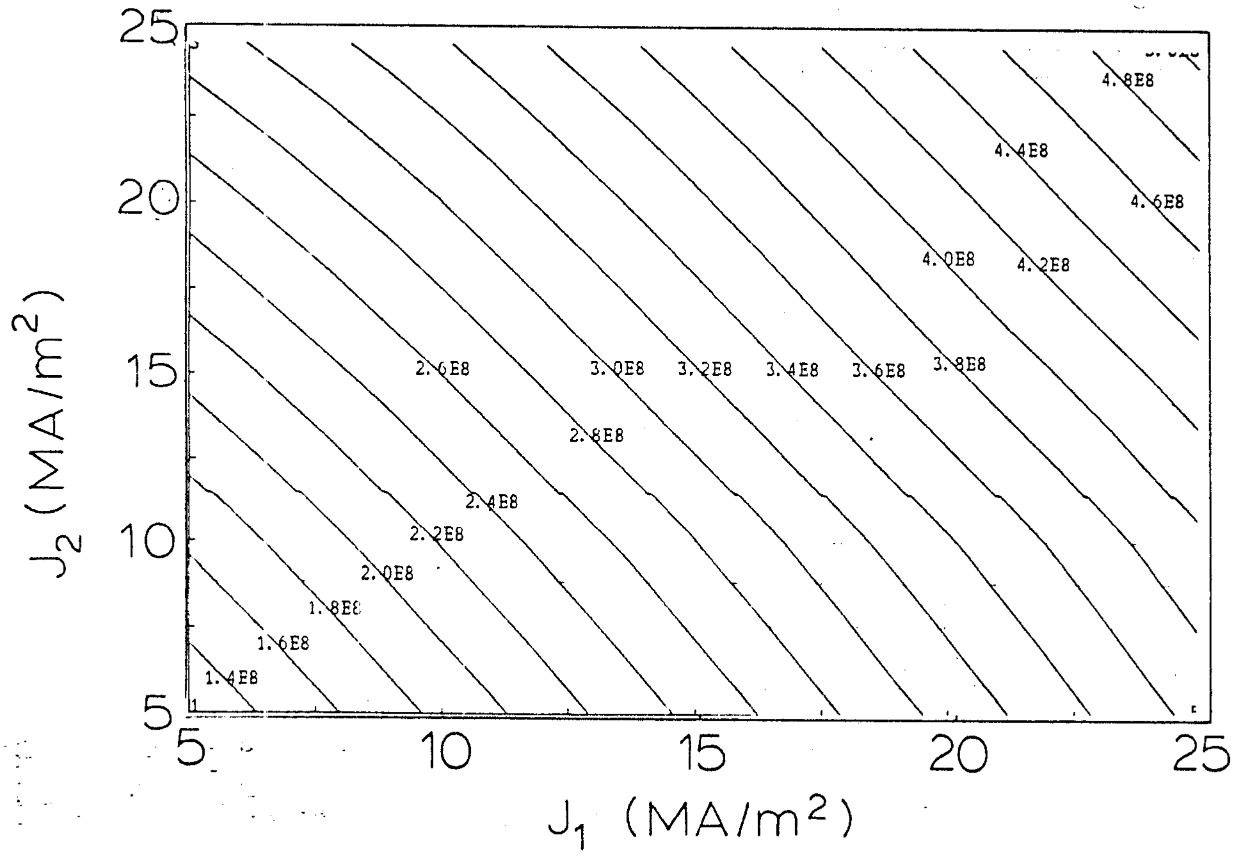

Figure 4.5.2.5 Contours of Constant Resistive Power Losses in EF Coil vs Current Densities in the Coils

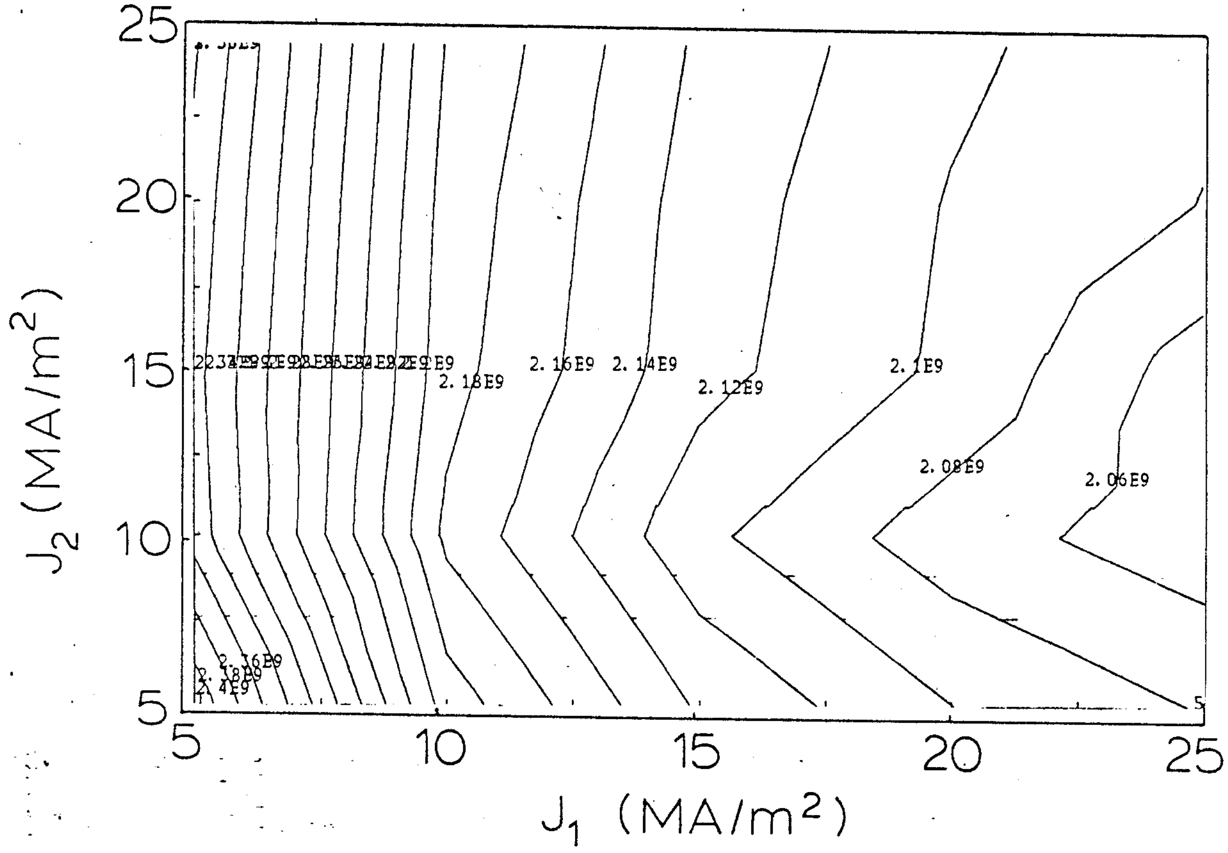

Figure 4.5.2.6 Contours of Constant Magnetic Stored Energy in EF Coil vs Current Densities in the Coils

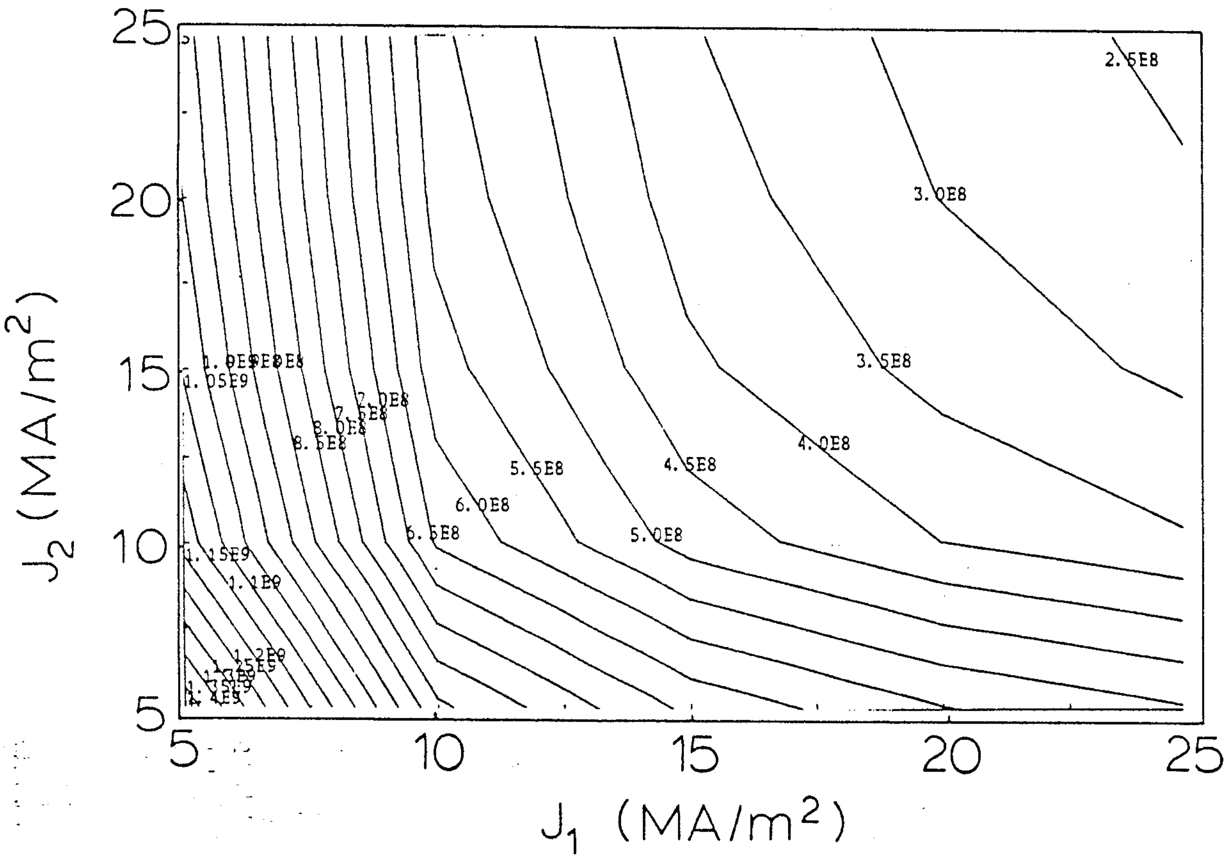

Figure 4.5.2.7 Contours of Constant Weight in EF Coil vs Current Densities in the Coils

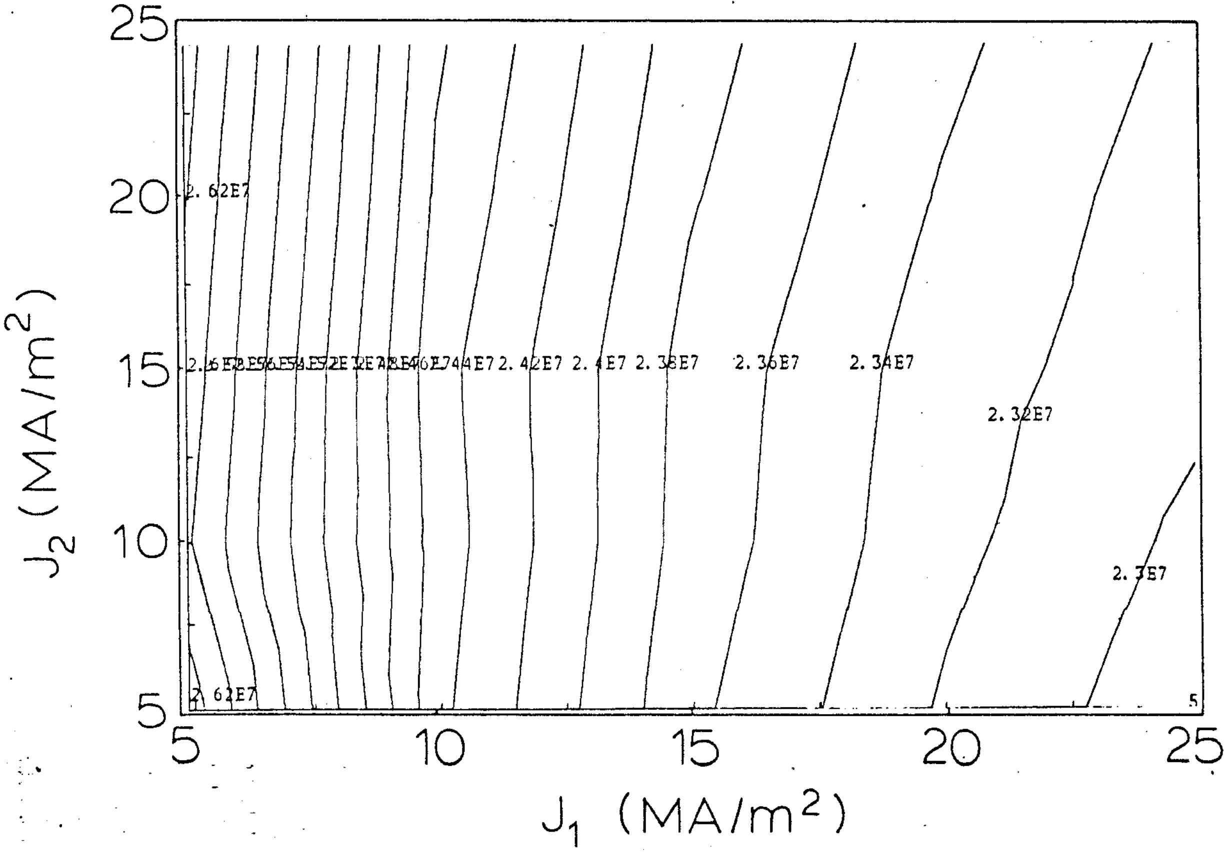

Figure 4.5.2.8 Contours of Constant Ampere Turns in EF Coil vs Current Densities in the Coils

References

[1] BAKER, C. *et al.*, "STARFIRE-Commercial Tokamak Fusion Power Plant Study," Argonne National Laboratory Report ANL/FPP-80-1 (1980)

[2] BECKER, H., MIT Plasma Fusion Center, private communication (1982)

[3] FILE, J., MILLS., R.G. and SHEFFIELD, G.V., "Large Superconducting Magnet Design for Fusion Reactors", IEEE Transactions of Nuclear Science NS-18 (1971) 277

[4] WELCH, C.T., "Bending Free Shapes for Toroidal Magnet Field Coils with Concentrated Symmetric Reactions", in *Proceedings of the Sixth Symposium on Engineering Problems of Fusion Research* (1976) 410

[5] BOBROV, E.S. and SCHULTZ, J.H., "A Model of Toroidal Magnet Systemsas Orthotropic Shells of Finite Thickness", in *Proceedings of the Ninth Symposium on Engineering Problems of Fusion Research* (1981)

[6] HOLMES, J.A., PENG Y-K.M., and LYNCH, S.J., "Evolution of flux-conseving tokamak equilibria with preprogrammd cross sections," Jour Comput Phys, 36, 35-54, (1980)

5 ILLUSTRATIVE DESIGN

In this section, the base case is described. The purpose of this chapter is to summarily describe the engineering aspects of an illustrative design of a resistive magnet reactor *AFTR* using DD-DT fuel cycle. A thorough analysis of the engineering of this device is outside the scope of this work. However, analysis of the magnet system of a smaller machine with similar characteristics (FED-R2) has been carried out and is reported in reference [1].

In Section 5.1 the base case is illustrated. In Section 5.2, the engineering concepts of the *AFTR* -type device are described.

5.1 Base Case

Table 5.1.1 shows the main characteristics of the base case for the full perfomance (full field). Figure 5.1.1 shows an elevation view of the machine. The main dimension of the reactor are shown in the figure. The poloidal field coils are shown. The port geometry is illustrated. Figure 5.1.2 shows a top view of *AFTR* . There are 16 modules, each with a port. Figure 5.1.3 shows a cross sectional view of *AFTR* . The first wall and the blanket/shield are not shown.

The machine can operate at full performance with $1 - \gamma = 0.07$. Table 5.1.2.a shows the tradeoffs of fusion power, wall loading and $1 - \gamma$ for the case of full performance. Operation at $1 - \gamma < 0.07$ at full field is ruled out due to wall loading limitations. Operation with increased values of $1 - \gamma$ result in lower wall loadings at full field. For $1 - \gamma$ as large as 0.3, the neutron wall loading is $P_{wall} \geq 1.8$ MW/m^2. Alternatively, for $1 - \gamma = 0.07$ the reactor can operate at a neutron wall loading of $P_{wall} = 1$ MW/m^2 by operation at lower plasma Q and reduced field ($B = 5.1$ T). This is shown in Table 5.1.2.b. In this case, the resistive power (TF plus EF resistive powers) is reduced to 320 MW, while the fusion power has been decreased to 350 MW.

Note that the fusion power decreases faster with decreasing magnetic field than the resistive power. This is due to the fact that the fusion power scales with the fourth power of the magnetic field, the resistive power scales as the second power of the magnetic field. Therefore, if the goal is to increase the value of $Q_{TF} = P_f/P_{TF}$, then the highest possible fields should be used.

The peak magnetic field on axis is 8.5 T, the major radius of the machine is 4.8 m, the aspect ratio is 4. The safety factor q is 2.5. The burn pulse in the machine is 100 seconds.

The energy in the toroidal field system is 17.5 GJ. The energy in the equilibrium field system (with small OH fields) is 2.7 GJ. The peak resistive power dissipation in the magnet is 610 MW, not including the vertical field system (another 300 MW).

The plasma TF coil distance is 0.50 m in the inboard side of the machine, while the distance in the outboard is 0.80 m. The space allowed for the plasma scrape-off distance is 0.14 m, leaving about 0.36 m for an inboard blanket, multiplier and the first wall. The outboard blanket can be substantially larger. There is no space in the throat of the magnet for shielding to reduce neutron streaming into the TF coil.

The weight of the machine, inluding TF coil plus blanket/shield, is 6.6 ktonnes. The tensile stresses in the inner throat of the magnet are $\sigma_{TF} = 150$ MPa. The circumferential stresses are $\sigma_{hoop} = 150$ MPa.

The neutron wall loading P_{wall} is 8 MW/m^2. The corresponding fusion power is 2.8 GW. The allowable value of γ is $\gamma = 0.93$ for $P_{wall} = 8$ MW/m^2. Lower values of γ can be obtained by operating at lower values of P_{wall}

Table 5.1.1

AFTR -TYPE DEVICE MAIN PARAMETERS

	PLASMA
MAJOR RADIUS (m)	4.8
MINOR RADIUS (m)	1.2
SCRAPE-OFF LAYER (m)	0.14
PLASMA ELONGATION (m)	1.5
PLASMA TRIANGULARITY	0.2
ASPECT RATIO	4.0
PLASMA TEMPERATURE (keV)	25
$1-\gamma$	0.07
D-T ION DENSITY (m^{-3})	1.8×10^{20}
SAFETY FACTOR	2.5
PLASMA CURRENT (MA)	11.1
EFFECTIVE CHARGE	1.2
PEAK-TO-AVERAGE RIPPLE AT EDGE (%)	0.8
TOTAL BETA (%)	6.2
FIELD ON AXIS (T)	8.5
D-T FUSION POWER (MW)	2800
NEUTRON WALL LOADING (MW/m^2)	8
	PLASMA HEATING (DT)
RF POWER (MW)	50
MODE	$2\omega_{cd}$
FREQUENCY (MHZ)	130
	BLANKET/SHIELD
INBOARD BLANKET THICKNESS (m)	0.29
OUTBOARD BLANKET/SHIELD THICKNESS (m)	0.59

AFTR -TYPE DEVICE PARAMETERS (continued)

	TF COIL
PLATE SIZE (m^2)	6.7×6.6
NUMBER OF TF PLATES	384
NUMBER OF MODULES	16
MAXIMUM TF FIELD (T)	13
MAXIMUM CURRENT DENSITY (kA/cm^2)	0.97
RESISTIVE LOSSES (MW)	610
TF POWER (START-UP) (MW)	800
TF STORED ENERGY (MJ)	17.5
TF WEIGHT (ktonnes)	6.5
TOTAL CURRENT (MA)	200
COIL CURRENT (kA)	520
CHARGE TIME (s)	60

	PF COILS
EF COIL A-TURNS (MAT)	27.9
V-s FROM EF COILS (Wb)	42
V-s FROM OH COILS (Wb)	125
TOTAL V-s FROM PF (Wb)	167
FIELD (OH SOLENOID) (T)	15.1
CURRENT RISE TIME (s)	4
CURRENT DENSITY (EF COILS) (MA/m^2)	12.
PEAK RESISTIVE POWER (EF COIL) (MW)	300
PEAK RESISTIVE POWER (OH COIL) (MW)	70

Table 5.1.2

(a) Peak Performance Trade-Offs

B	8.5T
P_{TF} (MW)	610
P_{EF} (MW)	300

$1-\gamma$	P_{wall}(MW/m^2)	P_f(GW)
0.0 (DT)	25	8.8
0.07	8	2.8
0.2	2.7	0.95
0.3	1.8	0.63

(b) Reduced Performance

$\gamma = 0.93$

B (T)	P_{wall}(MW/m^2)	P_f(GW)	P_{res}(MW)
8.5	8	2.8	900
7.1	4	1.4	636
6.0	2	0.7	450
5.1	1	0.35	320

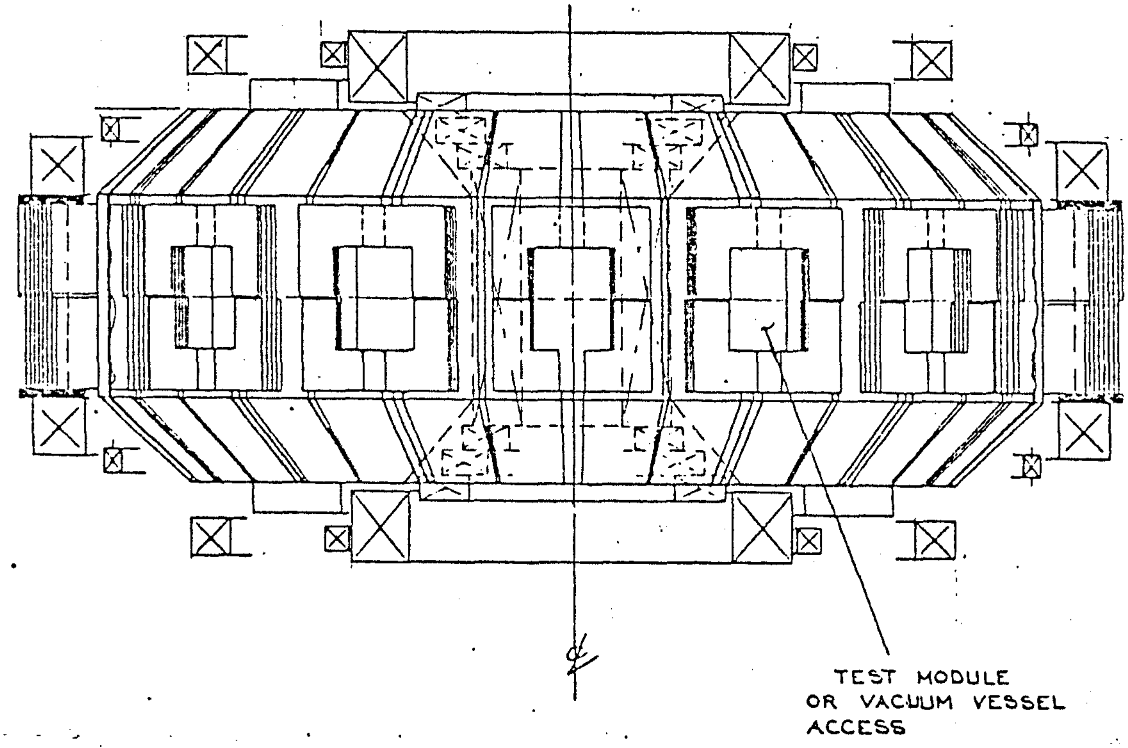

Figure 5.1.1 Elevation View of *AFTR* .

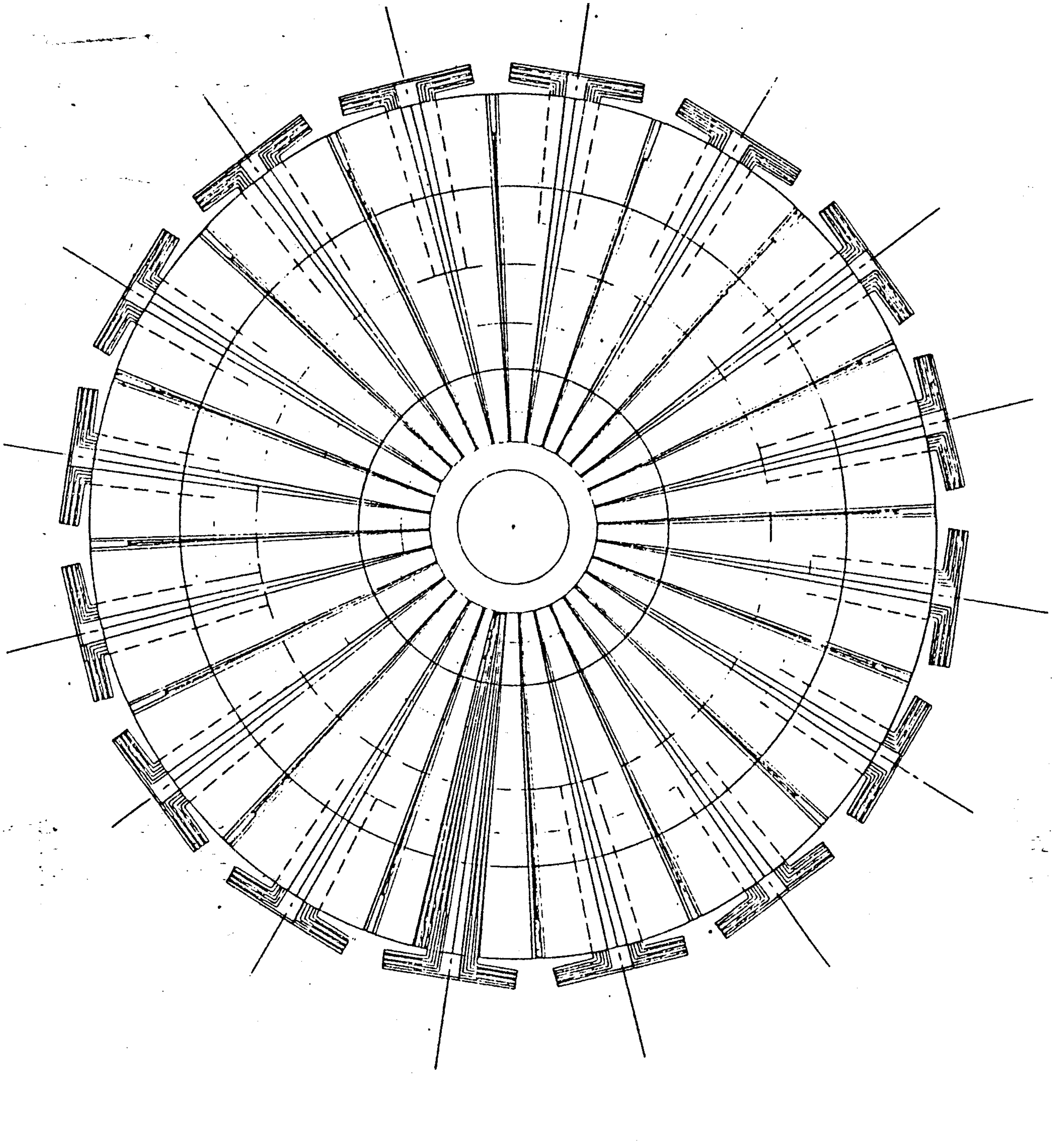

Figure 5.1.2 Top view of *AFTR* .

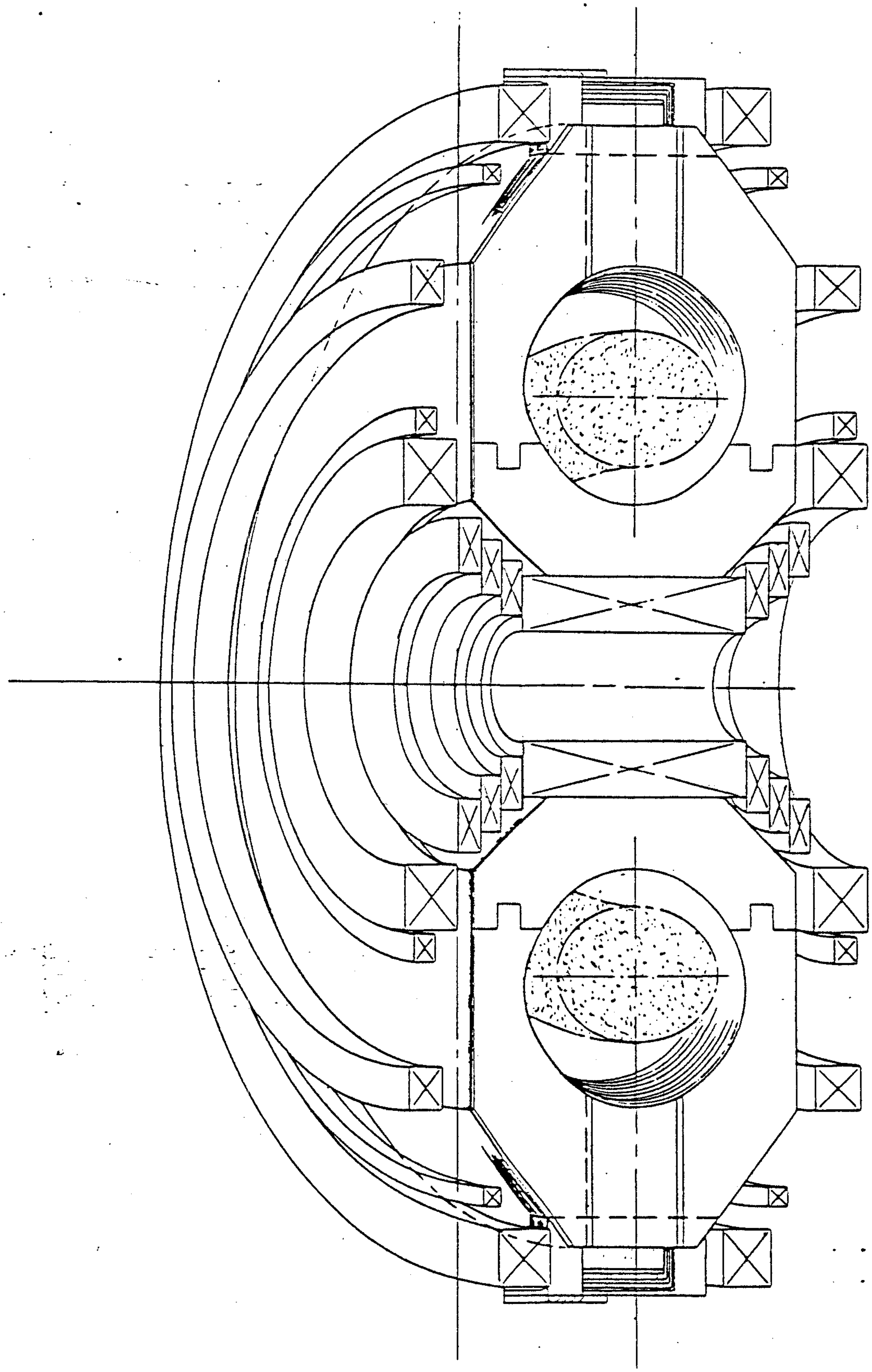

Figure 5.1.3 Cross Sectional View of *AFTR*.

5.2 Engineering Concepts for *AFTR*

The *AFTR* type of tokamak reactor is modeled after Alcator. The basis of the machine is a toroidal field coil made of tapered Bitter plates. But a major difference between Alcator and *AFTR* is the means by which forces generated in the copper plates are transmitted to the reinforcing steel and by which the overturning torque of the vertical field is restrained. In Alcator A these are both accomplished by friction between plates of the TF coil which, in turn, is achieved through adequate circumferential clamping. In Alcator C keying is used additionally. Because of the much higher in-plane and overturning forces in *AFTR* either very high circumferential stress is needed to provide sufficient friction or a positive support for each copper turn is needed. For reasons outlined below, the latter concept is adopted.

The TF coil of *AFTR* is operated continuously and cooled accordingly. Except for pulsed operation, cryogenic cooling provides no net economy over water-cooling. For pulses as short as one minute, liquid nitrogen pre-cooling might result in decreased capital cost. It cannot decrease operating cost however and has not been considered in the present conceptual design.

The choice of structural principle is influenced predominantly by emergencies and maintenance. Modularity has been adopted as a sine qua non of maintenance. It allows the removal of an octant (or possibly smaller unit) of the combined TF coil, blanket, first wall system. In order to fully exploit the advantages of modularity, a simple method of breaking and remaking a vacuum joint in the first wall is needed. The present design assumes that this will be done by means of differentially pumped, unwelded flange seals. This would eliminate the most complicated step in a change-out procedure and is considered to be feasible with some development. It is described below.

The magnetic fields of a tokamak are generated by four current sources; the toroidal field coil, the vertical field coils, the induction coil and the plasma. These fields and currents interact to produce Lorentz forces of which by far the most significant are the in-plane and overturning torque in the TF coil. The design of the TF coil system to withstand these forces dominates the conceptual design and is therefore considered exclusively in the present study.

5.3 The Toroidal Field Coil

5.3.1 Forces and Constraints

It is well known that forces of two rather distinct origins act on a tokamak TF coil system. These forces are characterized by being in-plane or out-of-plane. The in-plane forces arise from the interaction of the toroidal field with the current in the toroidal field magnet, the out-of-plane forces are generated by the interaction of the poloidal fields with the current in the toroidal field magnet and by the lateral reaction to the inward net radial force.

The in-plane forces consist of vertical and horizontal components. The vertical component in the throat combined with the lateral compression dictates the size of the machine, which must be large enough for this combined stress (von Mises or Tresa) to be an appropriately small fraction of the tensile yield stress of the material in the throat. In the outer vertical leg of the TF coil, the copper plates must be slit along the horizontal mid-plane to allow turn-to-turn current flow. This prevents the copper from carrying the vertical load in the outer leg. That force must therefore be transferred from the copper to the reinforcement.

Also, in the outer leg, the Lorentz force is radially outward and the slit prevents the copper from taking any of that loading in bending. Therefore that load also must be transferred to the reinforcement.

The general arrangement of the plates and the direction of forces is shown in figure 5.3.1.

All the in-plane forces are reacted by tensile or compressive stresses, as is the centering force. By contrast, the out-of-plane forces due to the overturning load must be reacted in shear. Figure 5.3.2 shows the disposition of the overturning loads and the shear stresses that react it.

The shear stress in the horizontal mid-plane of the TF coil is reacted by the reinforcement (stainless steel wedges). This mechanism is the same as that in all other Bitter type TF coils, such as Alcator. It is necessitated by the break in the copper in the outer leg where current transfer between turns is effected. Also, because of this break, the vertical load in the outer leg of the copper must also be transferred to the reinforcement. This is mediated by insulated keys, shown schematically in Figures 5.3.2 and 5.3.3. Figure 5.3.2 indicates their disposition and length; Figure 5.3.3 schematically shows their arrangement with respect to the cooling channels. These keys also serve to transmit vertical and horizontal shear forces in the vertical plane that are generated by the overturning movement.

The general arrangement of the EF and TF coils, ports and plasma is shown in Figure 5.3.4. An enlarged view of the TF coil plates near the port is schematically shown in Figure 5.3.5. The corners of the plates are removed to decrease their bending stiffness. This prevents large bending moments from being transmitted down the throat of the TF coil. It also offers the advantage of preferred coil placement. Both the induction coil and the vertical field coils need to be located as close to the plasma as possible: the space made available by the removal of the corners of the TF coil can profitably be occupied by those coils.

5.3.2 Cooling

The copper plates of the TF coil are water-cooled to allow steady state operation. The cooling channels are formed close to one surface of each copper plate by a lost wax process. The side chosen for the cooling channels is dictated by the shear forces due to vertical load transfer and overturning movement. These add on one side of the copper plate and subtract on the other. Thus there will be an asymmetry in the keys which react the Shear. The cooling channels will be located on the face of lowest shear load.

The cooling surface area of the channels is distributed throughout the plate in proportion to the thermal dissipation density: about 40% of the heat is generated in the throat region and 60% everywhere else. The channels are disposed so as to remove this distribution of heat with roughly uniform temperature rise in the copper.

5.3.3 Insulation and Electrical Interconnection

The reinforcement between copper plates is fully insulated and at ground potential. This allows the reinforcement to be used as structure for both the TF coil and the blanket or shield and first wall. The insulation between the copper plates and reinforcement is in the form of plane sheets in all locations. Inorganic or organic based insulatin may be used, such as mica or glass polyimide, depending on the as yet unresolved compromise needed between mechanical toughness and radiation resistance.

It is useful to note that deterioration of the insulation proceeds radially outward from regions closed to the plasma, the rate of deterioration decreasing by a factor 10 for each 15 cm of distance through the TF coil. More is said about the properties of the insulation under neutron irradiation in section 3.3.

The copper plates are split at the outer mid-plane to allow current transfer (see figures 5.3.2 and 5.3.3). The interconnector is shown in Figure 5.3.6. Conduction cooling alone limits the temperature of the interconnector.

The copper plates and reinforcement are specifically shaped to span the various flange openings. Two effects result from these spaces, TF field ripple and vertical load reaction. (The latter is described above).

5.3.4 Topology

The copper plates, insulators and reinforcements consist of standard and non-standard units according to their positions in the 22 1/2° modular sub-unit. The standard copper plates, reinforcement and keys are shown in plan view in Figure 5.3.7.

Each module is a 45° sector containing a central port flange and two end flanges. The latter form the vacuum seals by which the vacuum vessel is linked. Each half-flange mates to the corresponding half-flange in the adjacent module. The method of closure of these flanges is either by external welding or by demountable metal seals, differentially pumped to give the required quality of vacuum in the vessel. The module thus consists of two sub-modules which are mirror images in the central port flange. This is shown in Figure 5.3.8.

Each sub-module is in turn divided into parts in which the copper plates are either left or right handed. The left and right handedness of the plates arises from the method of fabrication (see Figure 5.3.7). Recourse to higher strength is needed in the throat, and the copper in that region is work-hardened to an appropriate degree by cold rolling. This process restricts plate size. Consequently the plates are manufactured in three parts. The throat section is machined to the required taper and electron beam welded to top and bottom sections of constant thickness and of softer grade as shown in Figure 5.3.4. One face of the tapered section is in line with one of the other faces of the other sections. Hence the left and right-handedness. Half way between a closure flange and a port flange the orientation of the copper plate is reversed by means of a double steel reinforcement (see Figure 5.3.7). This results in the juxta position of a plane copper face to the adjacent flange face. This, together with the double reinforcement, reduces toroidal field ripple to a very low level.

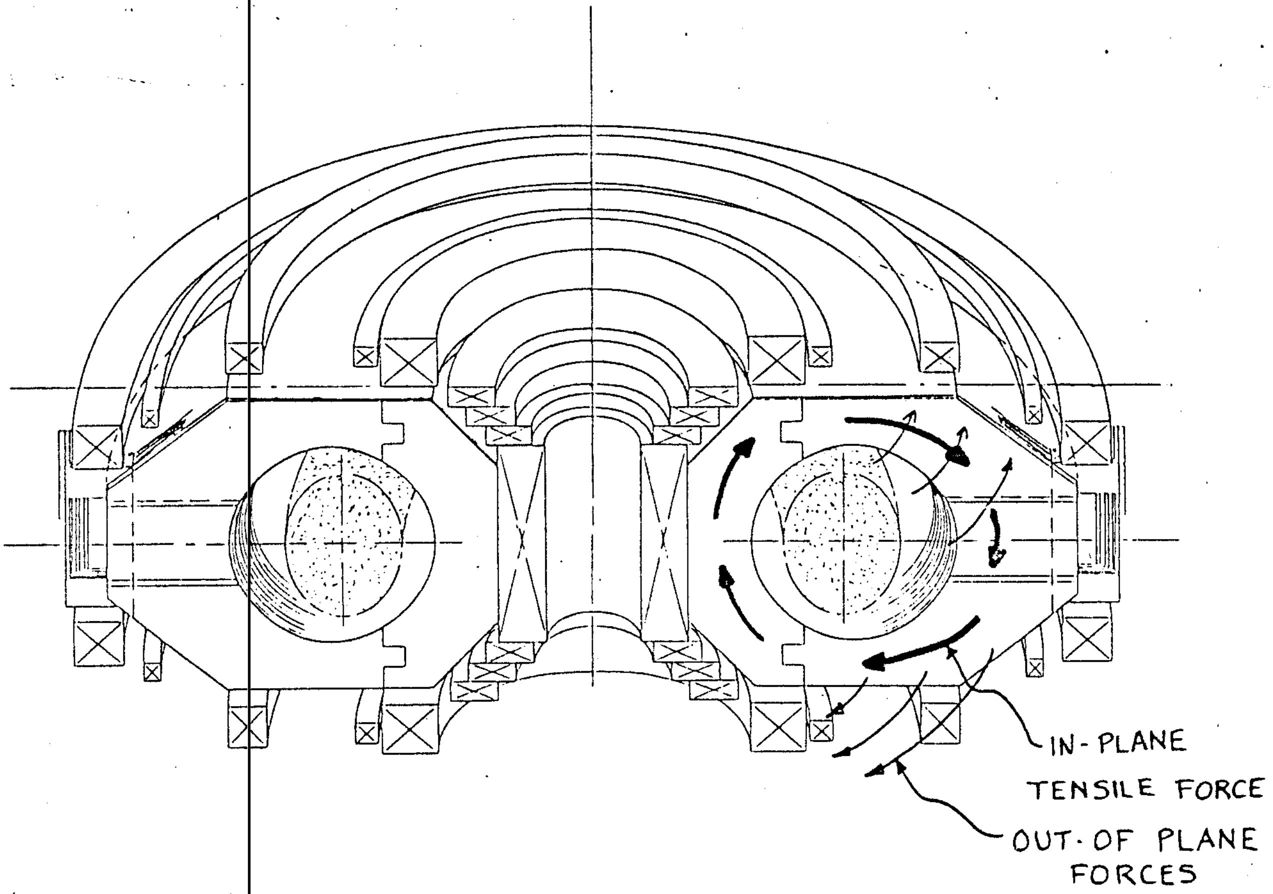

Figure 5.3.1 Direction of Applied Forces in *AFTR*

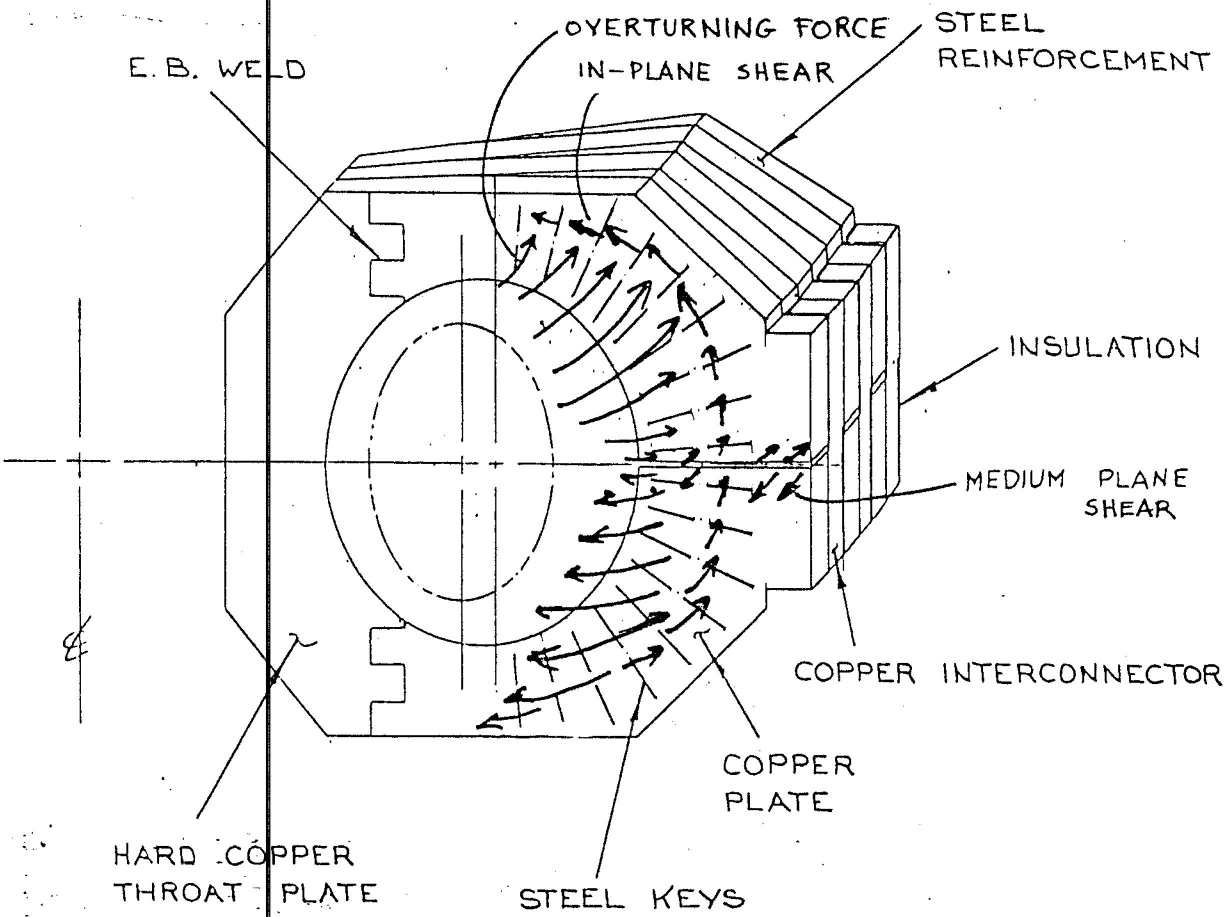

Figure 5.3.2 Applied Torsional Forces and Reacting Shear in the BITTER Plates.

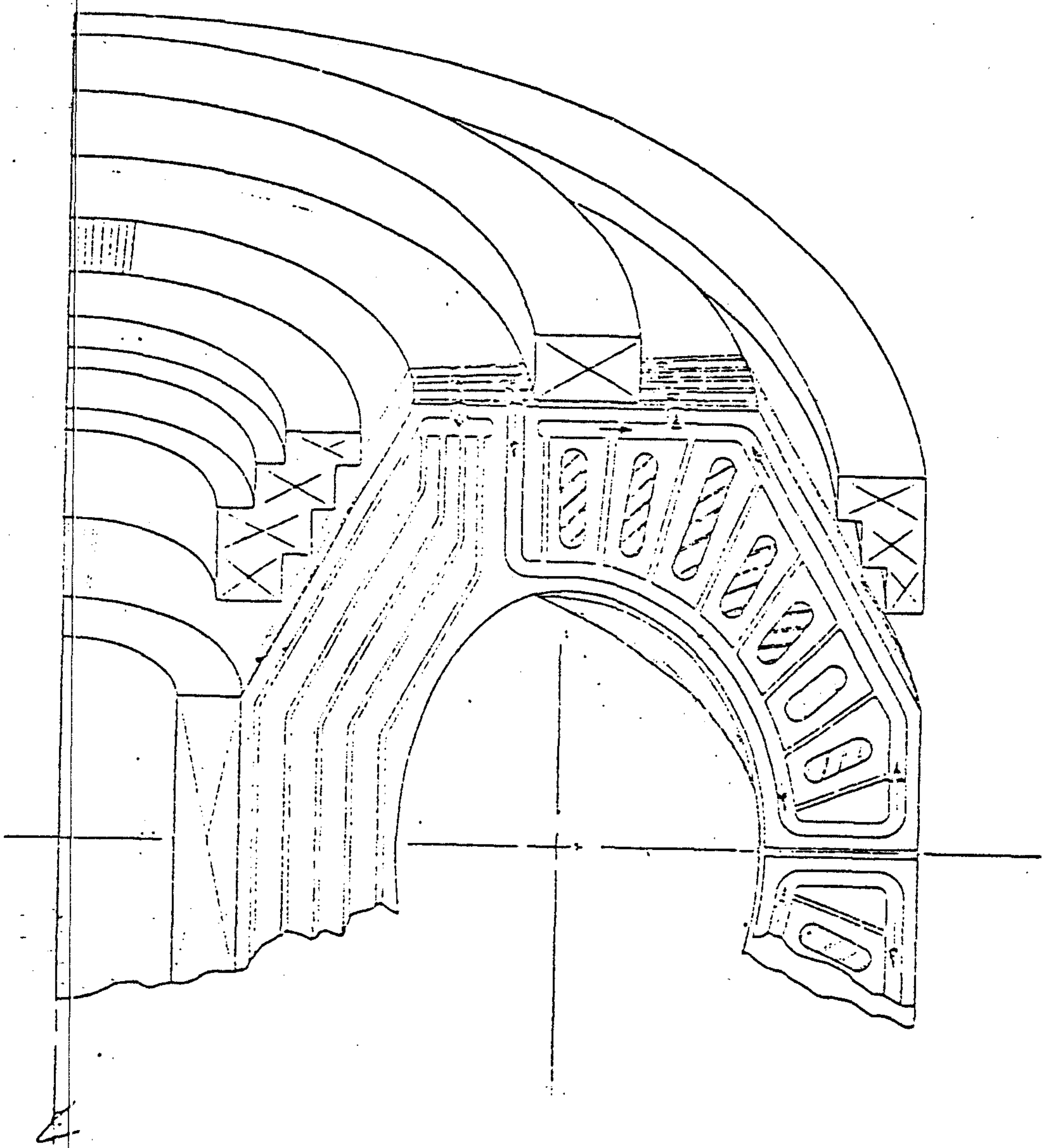

Figure 5.3.3 Schematic Arrangement of Keys and Cooling Channels in the BITTER plates of *AFTR* .

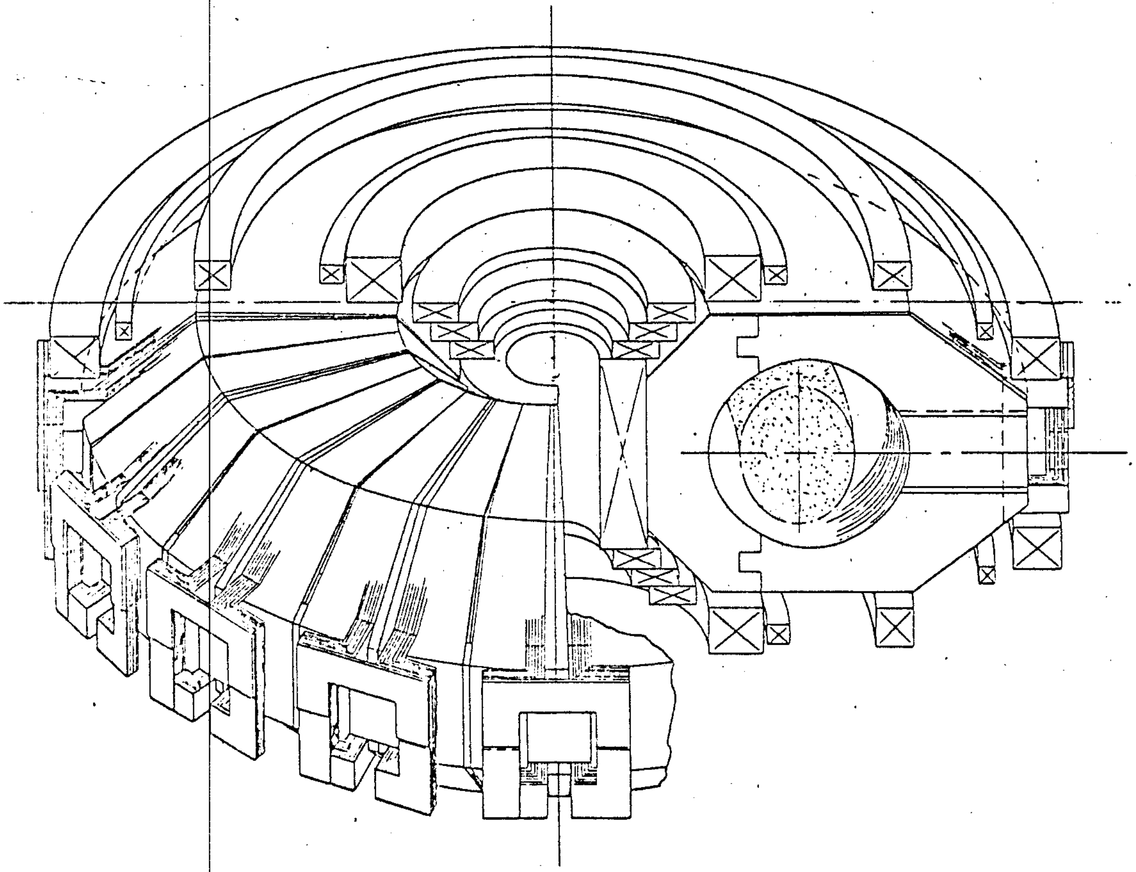

Figure 5.3.4 General Arrangement of the TF and EF Coils, Ports and Plasma in *AFTR* .

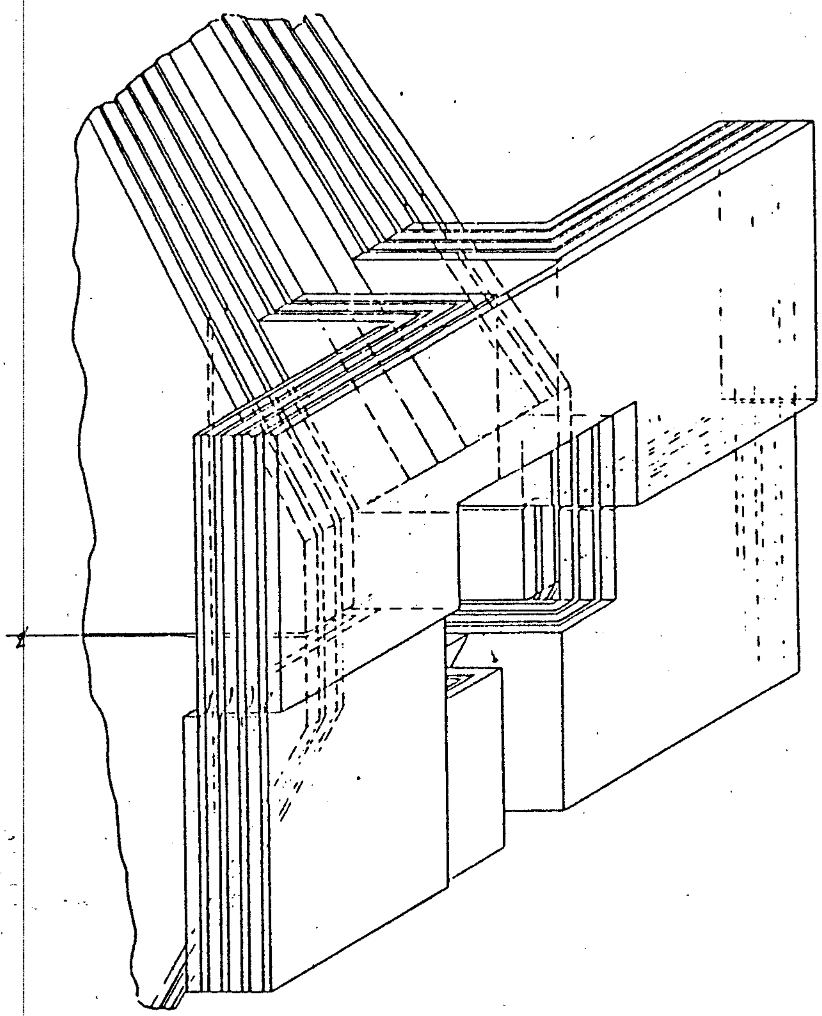

Figure 5.3.5 Schematic Diagram of the Plates of the BITTER TF Coil in the Vecinity of a Port.

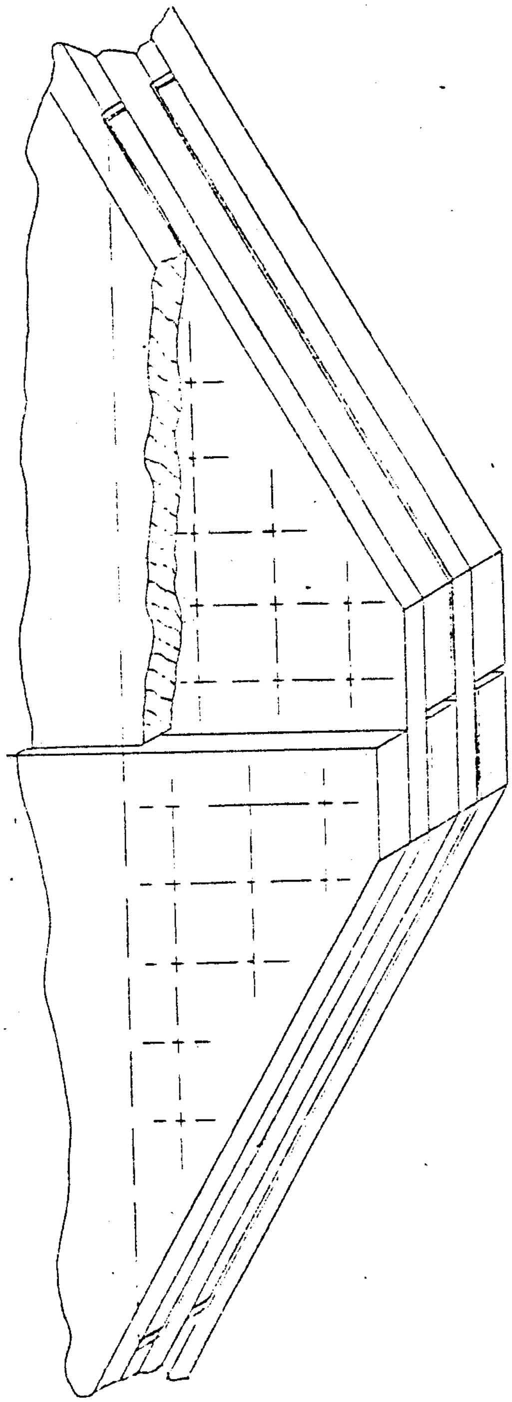

Figure 5.3.6 Connector for Plate-to-Plate Transfer of Current.

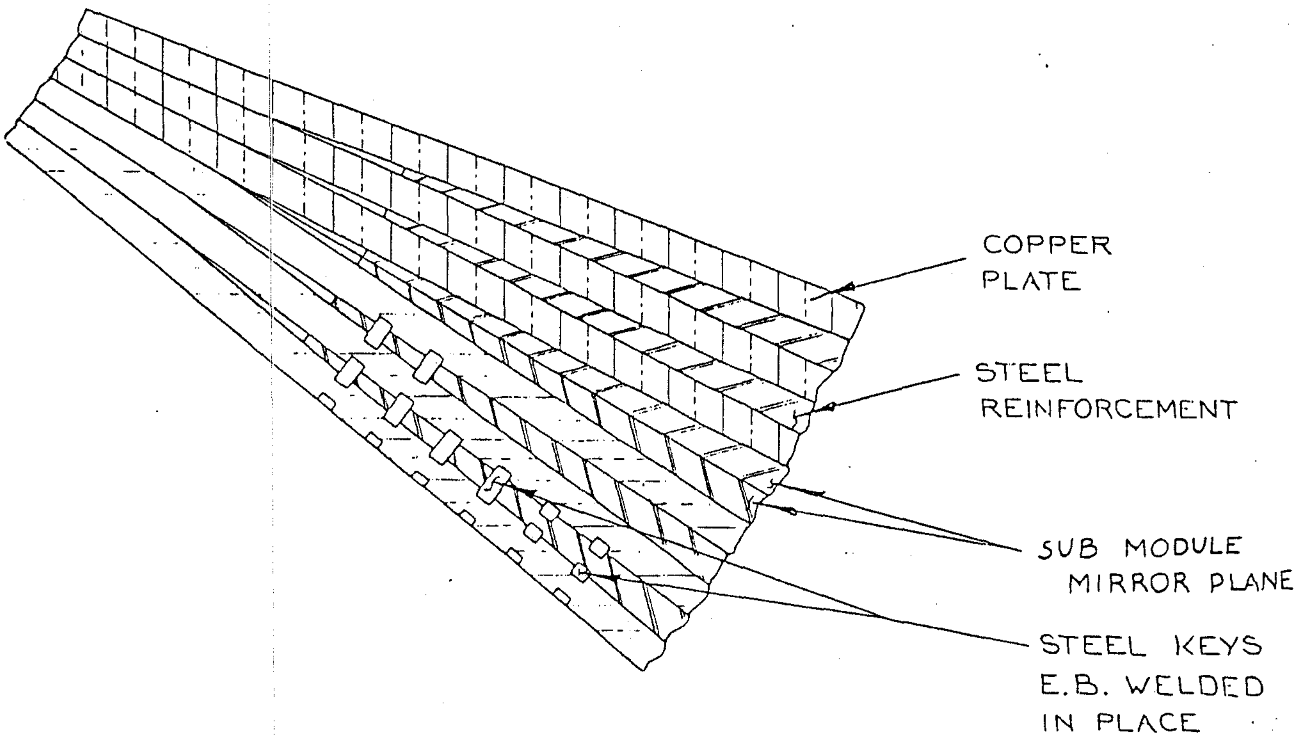

Figure 5.3.7 Sub-module Arrangement Showing Double Steel Reinforcement

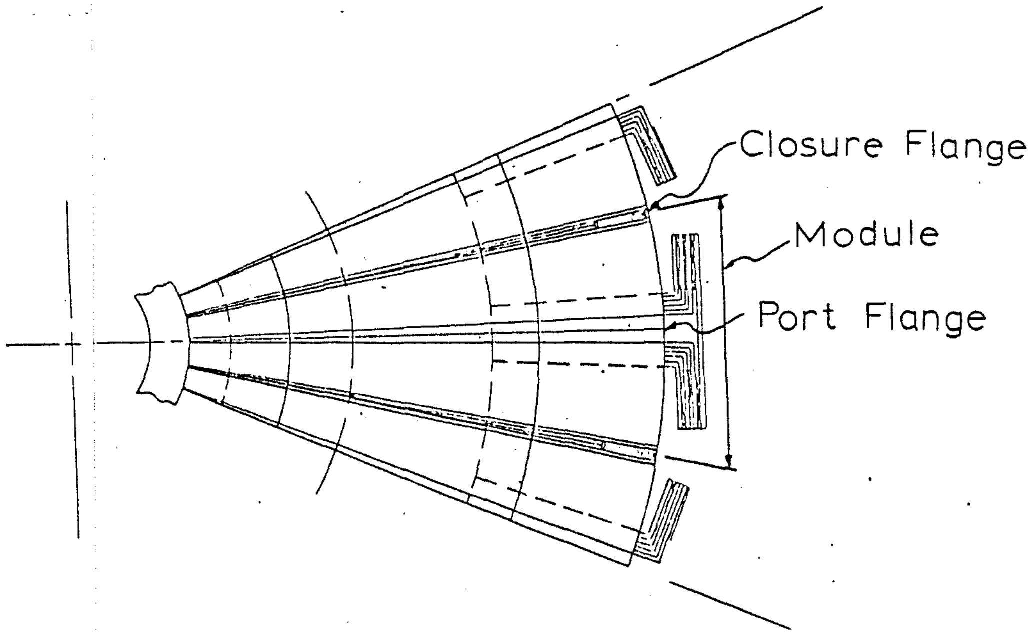

Figure 5.3.8 Module of Toroidal Field Coil. 16 Modules Constitute the BITTER magnet. Plasma Access is Gained through the Middle of the Module.

References

[1] WILLIAMS, J.E.C., BECKER, H., BLACKFIELD, D., BROMBERG, L., COHN, D.R., DIATCHENKO, R., LECLAIRE, R., "FED-R2: Concept and Magnet Design of a Low Cost FED", MIT Plasma Fusion Center Report PFC/RR-82-23.

6 SUPERCONDUCTING MACHINES

Resistive toroidal field coils represent both a high operating cost and, through power conditioning equipment, an appreciable capital cost. Furthermore, in the economics of a fusion reactor devoted to electricity production, recirculating power requirements may represent a significant part of the capital cost and hence drive up the cost per unit of electricity produced. Superconductive toroidal field coils solve or mitigate these disadvantages while presenting others. In order to determine the advantages and problems of superconducting toroidal field coils, a brief parametric study has been undertaken for their applications to *AFCR* (Advanced Fusion Commercial Reactor). This study has been carried out using a simple code, REACTOR, which designs the smallest tokamak reactor consistent with a set of input parameters.

6.1 The REACTOR Program

This code sizes a tokamak from data describing the physics of the plasma and the engineering constraints of conductor and structures.

Input data is the following:

• plasma parameter	$\beta^2 B^4 a^2$
• aspect ratio	R/a
• burn time	τ_{burn}
• first wall, blanket/shield and scrape-off distance	$\Delta_{in}, \Delta_{out}$
• tensile stress allowable in	
toroidal structure	σ_{TF}
bucking cylinder	$\sigma_{buckpost}$
induction structure	σ_{OH}
stabilizing copper	σ_{Cu}
• current density in toroidal and induction winding coils	$j_{TF,c}, j_{OH,c}$
• fraction of copper in the windings	F_{Cu}
• maximum induction coil flux density	$B_{OH,max}$
• number of TF coils	N_{coils}
• beta constant	$c_\beta = \beta R/a$
• plasma elongation	b/a
• peak electron temperature	T_e

Using these, together with a guessed initial value of major radius, the program sizes the toroidal field coils, bucking cylinder and ohmic heating transformer for the smallest possible machine. The output data is the following:

- required induction flux ϕ_{OH}
- major radius R
- minor radius a
- toroidal field, at the plasma and at the TF winding B, B_{max}
- toroidal current I
- induction coil radii R_{OH}
- bucking cylinder inner and outer radii $R_{1,buck}$ and $R_{2,buck}$
- TF coil inner and outer radii of inner leg $R_{1,TF}$ and $R_{2,TF}$
- TF coil, shape factor and inner radius of outer leg
- centering and tensile forces in TF coil
- fraction of cross sections devoted to windings
- average current densities in cross sections j_{TF} and j_{OH}
- length of TF conductor in ampere-meter ℓ_{cond}
- fusion power and wall loading P_f and P_{wall}

The code is simple and short. It is intended for parametric survey. A greater range of input variables than those listed can be achieved by manipulation of the input data. For instance, spacing between TF coils can be simulated by decreasing input stresses and current densities. Resistive OH transformer can be simulated by changing the maximum induction coil flux density. Copper TF coils can be simulated by increasing the copper fraction in the windings to 100% and decreasing the TF structural stress to zero. This even allows copper-stainless steel composites to be simulated.

The program has been used to investigate the probable sizes and parametric dependences of *AFCR* type systems with superconducting toroidal and poloidal field coils. The results are shown in the next chapter.

The assumptions of the code are given in Table 6.1. Some of the parameters shown in Table 6.1 are varied in the scoping study presented in the next chapter.

Chapter 8 describes the engineering features of an illustrative design.

Table 6.1

Assumptions for the Reactor Code

TF ripple on-axis, δ_o	0.1%
number of TF coils, N_{coils}	16
tensile stress in TF structure, σ_{TF} (MPa)	270
tensile stress in OH structure, σ_{OH} (MPa)	300
tensile stress in TF copper, σ_{Cu} (MPa)	135
bucking cylinder compressive stress, $\sigma_{buckpost}$ (MPa)	300
TF winding current density, j_{TF} (MA/m^2)	18
OH winding current density, j_{OH} (MA/m^2)	18
EF winding current density, j_{EF} (MA/m^2)	15
OH field strength, $B_{OH,max}$ (T)	7
fraction of stabilizing copper in TF windings, f_{Cu}	70%
$c_\beta = \beta \times A$	0.25
peak electron temperature, T_{eo}(keV)	35

7 SCOPING STUDIES OF *AFCR*

In this section, parametric scans of the *AFCR* (Advanced Fusion Commercial Reactor) are performed to illustrate the tradeoffs.

The device we are considering, *AFCR* , is an advanced applications commercial reactor. Its goal would be to be a net generator of electricity, coupled with self-substaining tritium production. The reactor could be designed in order to optimize the blanket/shield region and the first wall with self sufficiency in tritium. The blanket/shield and first wall would be optimized in terms of activation (either short term or long term), lifetime of first wall under sputtering or disruptions (which may require thicker walls) or for applications other than direct production of electricity. These applications could be synthetic fuel production, breeding of fissile material or breeding excess tritium production to be used in smaller reactors that do not have tritium self sufficiency.

7.1 *AFCR* with DD-DT fuels

In this section, reactor characteristics of an *AFCR* operating with DD-DT fuels are described. There is a wide range of operation with DD-DT as fuel. Where to operate in DD-DT fuels could depend on the reactor size required for sufficiently large wall loadings. In this section, the main engineering and plasma physics parameters are kept fixed, and the parameter $1-\gamma$ which identifies the regime of operation in DD-DT is allowed to vary. In the following sections of this chapter, specific tradeoffs and parametric studies are performed for fixed $1-\gamma$. There it is found that an aspect ratio $A \sim 4$ optimizes *AFCR* . Therefore in this section it assumed that $A \sim 4$. The other important parameters used in this section are described in Table 7.1.1. A is the aspect ratio, P_{wall} is the average neutron wall loading in the plasma surface, q is the plasma safety factor, $c_{\beta} = \beta \times A$, $\kappa = b/a$ is the plasma elongation, T_e is the electron central temperature, τ_{burn} is the length of the plasma burn, σ_{TF} is the tensile stress in the throat of the TF magnet, $\sigma_{buckpost}$ is the stress in the buckin post, δ_o is the ripple at the plasma edge, N_{coils} is the number of toroidal field coils, and $B_{OH,max}$ is the peak field in the *OH* transformer.

Table 7.1.2 shows the main reactor parameters of an *AFCR* device as a function of $1-\gamma$. The parametric variation is performed assuming the constraints in Table 7.1.1. The wall loading is kept fixed in order to compare reactors with similar problems relevant to the first wall (impurity control, life-time and cooling).

The magnetic field on axis B is varied between 4.0 T and 8.0 T. The corresponding values of $1-\gamma$ vary between 0 and 0.4. The aspect ratio is kept constant at $A \sim 4$. The wall loading is also kept also constant at $P_{wall} = 2.2$ MW/m^2. The value of the plasma performace P defined in chapter 2, increases very fast with increasing value of $1-\gamma$. This is due to the fact that the specific fusion power density $P_f/\beta^2 B^4$ decreases rapidly as the mode of operation moves away from DT.

In Table 7.1.2 R is the plasma major radius, a is the minor radius, I is the plasma current, E_{TF} is the energy stored in the TF coil, ℓ_{cond} is the conductor length times the conductor current for the TF coils, $B_{TF,max}$ is the peak field at the conductor of the toroidal field coil, $W_{blanket}$ is the weight of the blanket/shield, E_{OH} is the energy stored in the magnetic field of the OH transformer when it is up to full field and I_{OH} is its corresponding current, and E_{EF} and W_{EF} are the energy stored and the weight of the vertical field system and MA_{EF} is the Mega Ampere turns in this system.

$1-\gamma = 0$ corresponds to DT operation. (There is a small deviation from $1-\gamma = 0$ for DT, because of the small contribution to the neutron production by the deuterium reactions D(D,n)He$_3$ which produces a neutron and D(D,p)T, which produces a triton; these reactions are present in a 50-50 DT fuel mixture). The machine for $1-\gamma = 0$ (DT operation) is somewhat larger than typical fusion designs which operate on DT. The reason for the larger size is that the pulse length is 3600 s. The pulse length for typical DT reactor designs is a few minutes. The largest machine has a plasma performance $P = 155$ m^2 T^4, which results in $1-\gamma = 0.6$, or about half way between DT and DD in terms of tritium breeding required in the blanket for self-sufficiency in tritium. The operating temperature varies for the different cases in Table 7.1.2. For a fuel mixture close to DT, the fusion power is maximized for $T_i \sim 20$ keV, while for DD-DT operation for $1-\gamma > 0.05$, the temperature for minimizing the value of P required for ignition occurs at higher temperatures. Note, however, that the specific fusion power density does not vary significantly with temperature in the temperature range $25 < T_i < 35$ keV in the range of $1-\gamma$ considered in Table 7.1.2 as shown in Chapter 2.

The OH transformer has a significant consequence on the machine design due to the relatively long pulse length. High temperature is favored by the OH transformer due to decreased resistivity during burn with higher temperatures. The lower temperature in the DT case is a tradeoff between decreased fusion power density and decreased OH drive requirements at the higher temperatures. The lower temperatures result in a more attractive design for DT, while the higher temperatures are favoured by DD-DT operation. This is due to the fact that the specific fusion power density is relatively flat with temperature in the case of DD-DT operation, while the higher temperature reduces the required volt seconds from the OH transformer.

Also shown in Table 7.1.2 are the fusion power and neutron wall loading if the reactors are operated with DT fuel.

From Table 7.1.2, it can be seen that there is a factor of ~ 10 reduction in fusion power for $1-\gamma = 0.2$ due to the lower reactivity of DD-DT relative to that of DT. The equivalent DT wall loading increases very fast with $1-\gamma$, with the consequence that DT operation cannot be used in a reactor desinged to run DD-DT, unless the reactor is underrated (the magnetic field or the plasma β can be dropped to decrease the fusion power).

The results in Table 7.1.2 are shown in Figures 7.1.1 through 7.1.3 as a function of $1-\gamma$. Figure 7.1.1 shows the normalized values of the plasma parameters P, I, R, P_f and B as functions of $1-\gamma$. Figure 7.1.2 shows the parameters of the toroidal field system E_{TF}, $B_{TF,max}$ and ℓ_{cond} as functions of $1-\gamma$. Figure 7.1.3 shows the parameters of the vertical field system as functions of $1-\gamma$. There are large increases in the main parameters of the reactor as the fuel mixture moves away from DT towards SCD.

The value of $1-\gamma$ for operating an electricity producing reactor is the value necesary to obtain tritium self sufficiency. The tritium breeding ratio is determined by the neutronic characteristics of the blanket. Therefore, the overall tritium breeding ratio is determined by both $1-\gamma$ and the blanket.

Although the reactor increases in size, it is interesting to note that the availability of excess neutrons (neutrons not required for tritium breeding) increases as fuel mixture moves away from DT. The number of excess neutrons (see chapters 2 and 4) scales as

$$R_n \sim 3.6 \times 10^{20}(k-\gamma)P_f$$

where R_n is the excess neutron rate in neutrons per s, k is the effective breeding ratio of the blanket and P_f is the fusion power in GW. Due to the fact that P_f increases with increasing $1-\gamma$ while γ decreases, R_n increases. The question is whether the increase in R_n is large enough to compensate for the increase in machine size. Figures 7.1.4 and 7.1.5 show the ratios R_n/E_{TF} and R_n/ℓ_{cond} as function of $1-\gamma$ for k varying from 0.9 through 1.1. The use of the *AFCR* device for neutron applications becomes more attractive with increasing value of $1-\gamma$. The ratios R_n/E_{TF} and R_n/ℓ_{cond} increase with $1-\gamma$ for $k < 1.05$. For $k \simeq 1.1$, the ratio R_n/E_{TF} remains approximately constant, while the ratio R_n/ℓ_{cond} increases with increasing $1-\gamma$. However, the device size also increases substantially. The point of operation is a tradeoff between more efficient excess neutron generation rate and increased plant size. This tradeoff has not been analyzed in the work reported here. From the point of view of neutron applications, operation in DD-DT fuels is attractive.

For illustrative purposes, it was chosen to do engineering analysis on the machine with $1-\gamma = 0.8$, that is, $R = 9.6$ m. This machine would be able to produce a substantial amount of excess neutrons, or, equivalently, would be able to be self sufficient in tritium production in a blanket that has been optimized for purposes other than tritium breeding (maybe without an inboard blanket, or with a solid blanket without multiplier).

The remaining of this chapter deals with parametric optimization and scoping of the *AFCR* device. Chapter 8 deals with some engineering issues of the *AFCR* device.

Table 7.1.1

Assumptions for Scoping Study

vs $1 - \gamma$

A	4
P_{wall} (MW/m^2)	2.2
q	2.5
c_β	0.25
b/a	1.5
T_e (keV) (DT)	18
(DD-DT)	35
τ_{burn} (s) ($Z_{eff} = 1$)	3600
σ_{TF} (MPa)	270
$\sigma_{buckpost}$ (MPa)	300
fraction of stabilizing copper in TF windings	70%
δ_o	0.1%
N_{coils}	16
$B_{OH,max}$ (T)	7

Table 7.1.2

Parametric Scan vs $1-\gamma$

for $P_{wall} = 2.2$ MW/m^2

$1-\gamma$	0.005	0.125	0.20	0.275	0.375
A	4.01	4.0	4.0	3.99	3.99
R (m)	6.61	8.4	9.6	10.7	12.3
a (m)	1.65	2.1	2.4	2.69	3.07
B (m)	4.06	6.45	7.05	7.52	8.0
I (MA)	7.4	15.0	18.7	22.4	27.2
P (m^{2}T^4)	2.88	29.8	55.6	90.7	151.
P_f (GW)	1.54	2.34	3.1	3.9	5.2
DT-equivalent operation					
P_{wall} (MW/m^2)	2.2	17.8	29.1	42.3	61.7
P_f (GW)	1.54	18.0	40.7	74.2	141.
E_{TF} (GJ)	13.5	55.9	89.2	131.	206.
ℓ_{cond} (GA m)	7.22	18.6	26.5	35.5	49.3
$B_{TF,max}$ (T)	7.76	11.2	11.9	12.3	12.7
$W_{blanket}$ (Gg)	1.43	2.14	2.69	3.27	4.13
E_{OH} (GJ)	8.03	12.0	17.5	24.2	35.2
I_{OH} (MA)	89.8	113.	125.	137.	152.
E_{EF} (GJ)	2.15	9.12	14.2	20.4	30.7
W_{EF} (Gg)	0.466	1.07	1.4	1.75	2.25
MA_{EF} (MA turns)	16.4	31.2	36.4	41.3	47.2

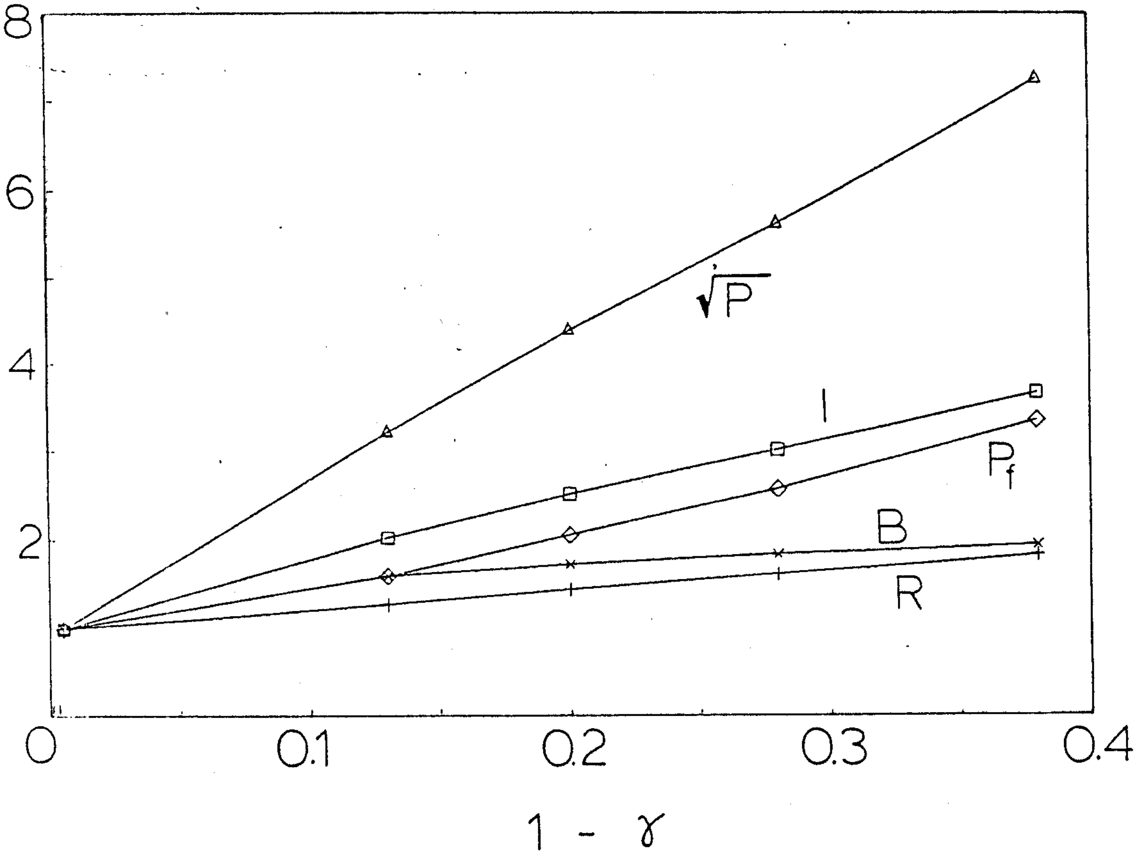

Figure 7.1.1 Normalized Values of P, I, R, B and P_f as Functions of $1 - \gamma$ for *AFCR* Type Devices with $P_{wall} = 2.2$ MW/m^2

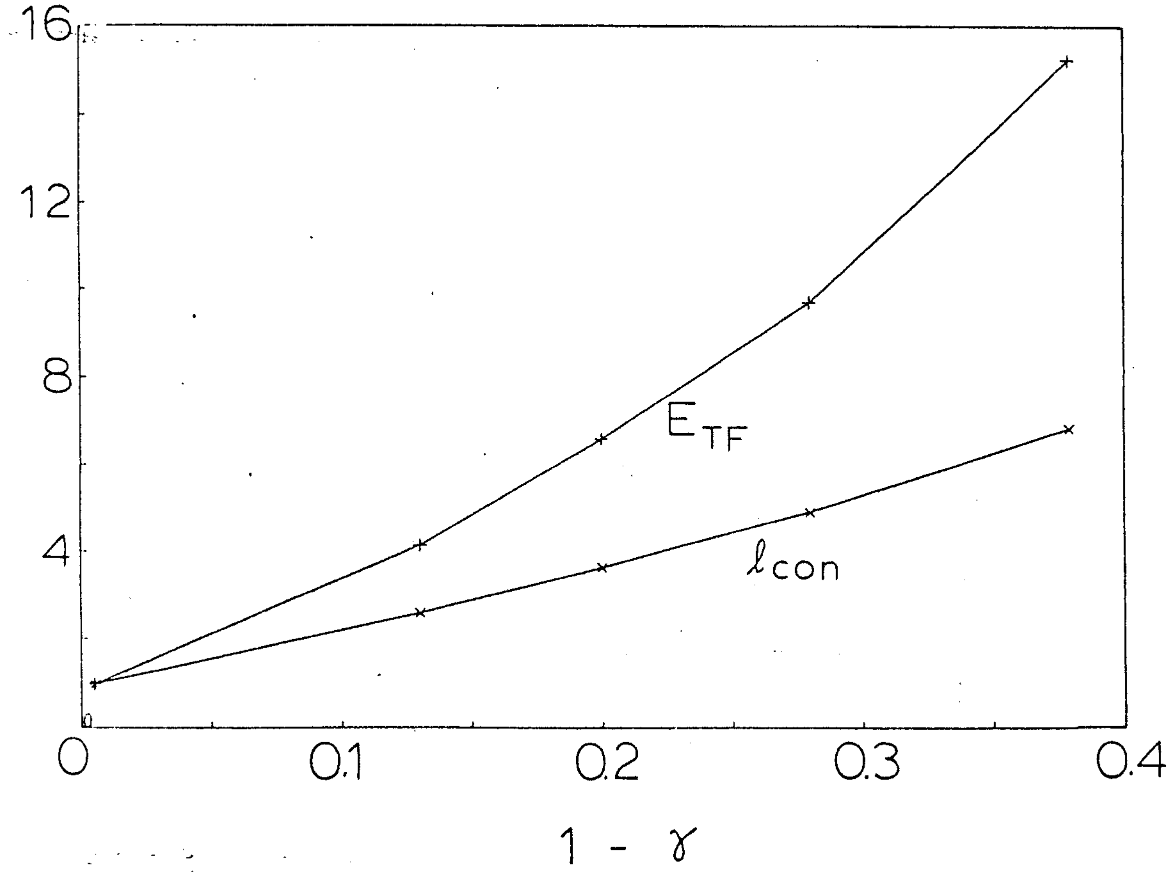

Figure 7.1.2 Normalized Values of E_{TF} and ℓ_{cond} as Functions of $1-\gamma$ for *AFCR* Type Devices with $P_{wall} = 2.2$ MW/m^2

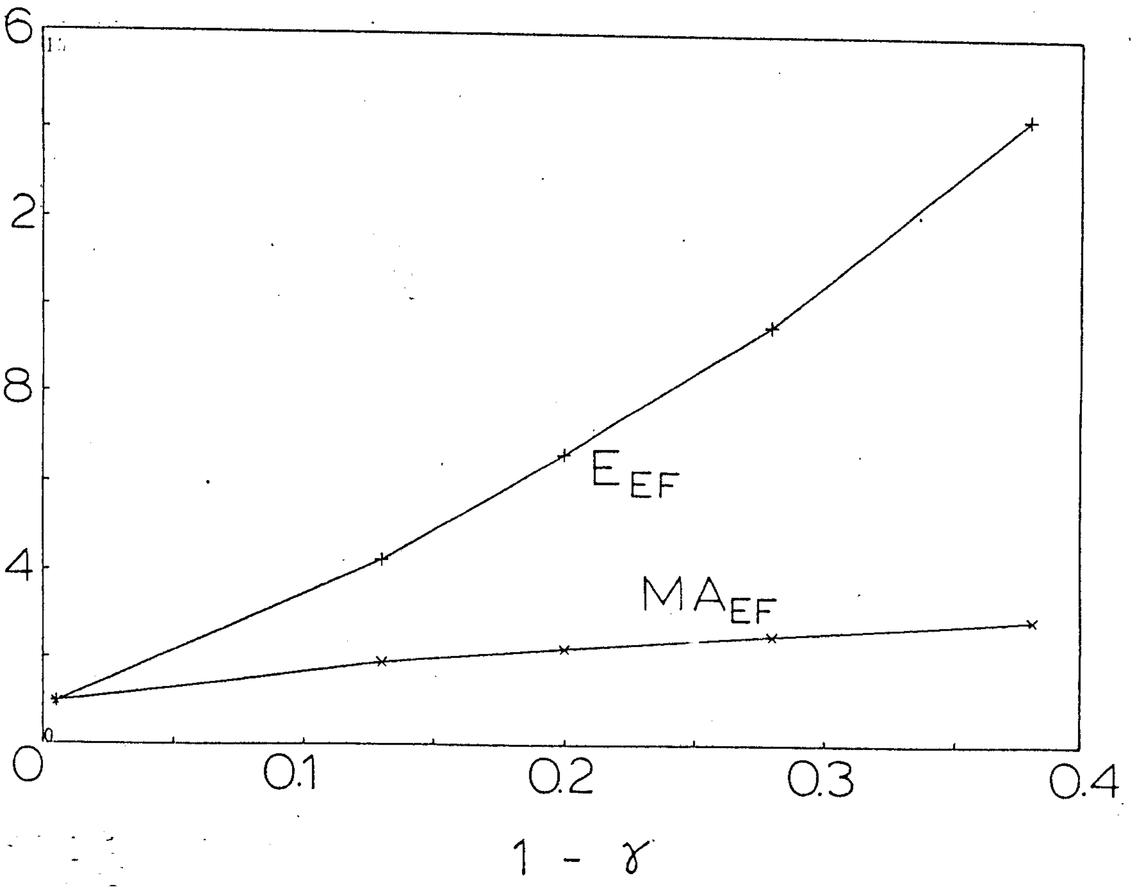

Figure 7.1.3 Normalized Values of E_{EF} and MA_{EF} as Functions of $1 - \gamma$ for *AFCR* Type Devices with $P_{wall} = 2.2$ MW/m^2

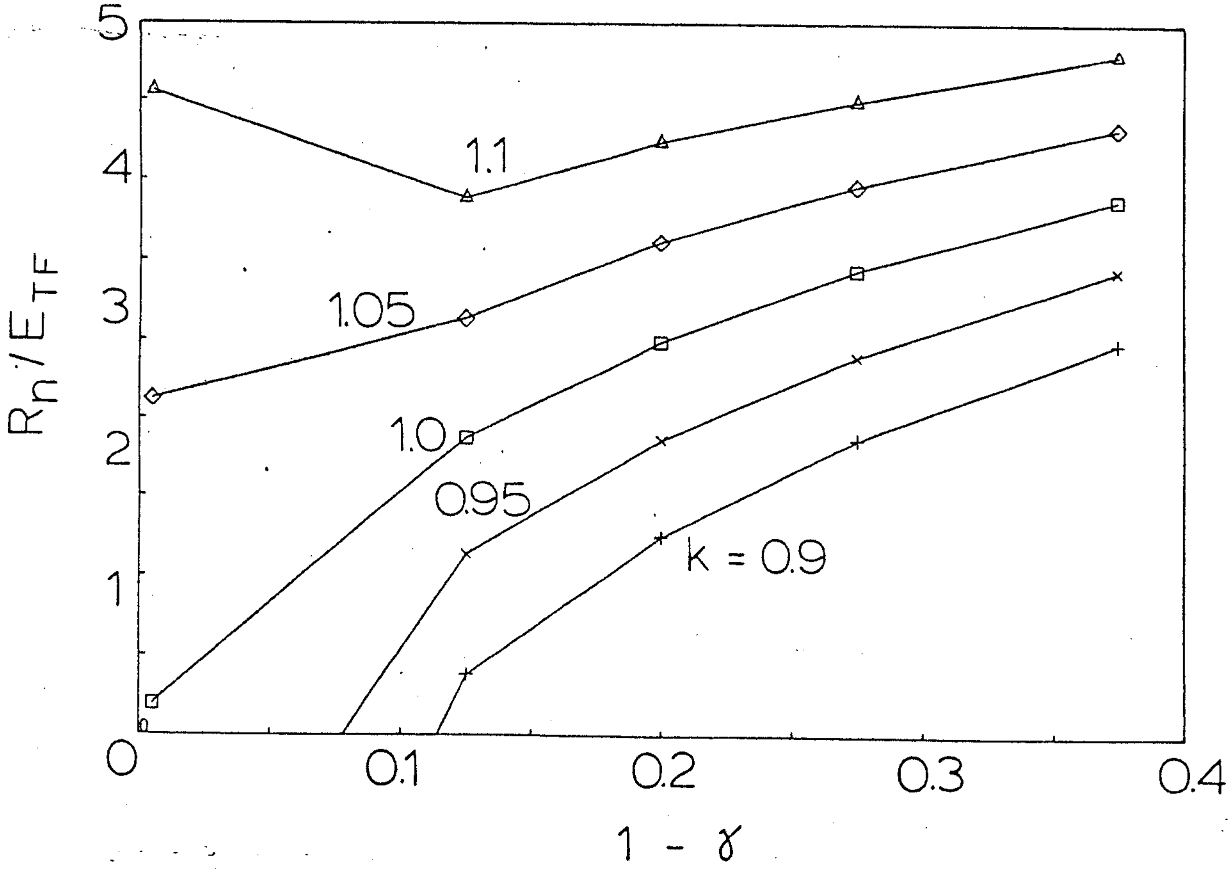

Figure 7.1.4 Ratio of Excess Neutron Generation Rate and E_{TF} as Function of $1 - \gamma$ for *AFCR* Type Devices with $P_{wall} = 2.2$ MW/m^2. *k* is the Effective Tritium Breeding Ratio (arbitrary units)

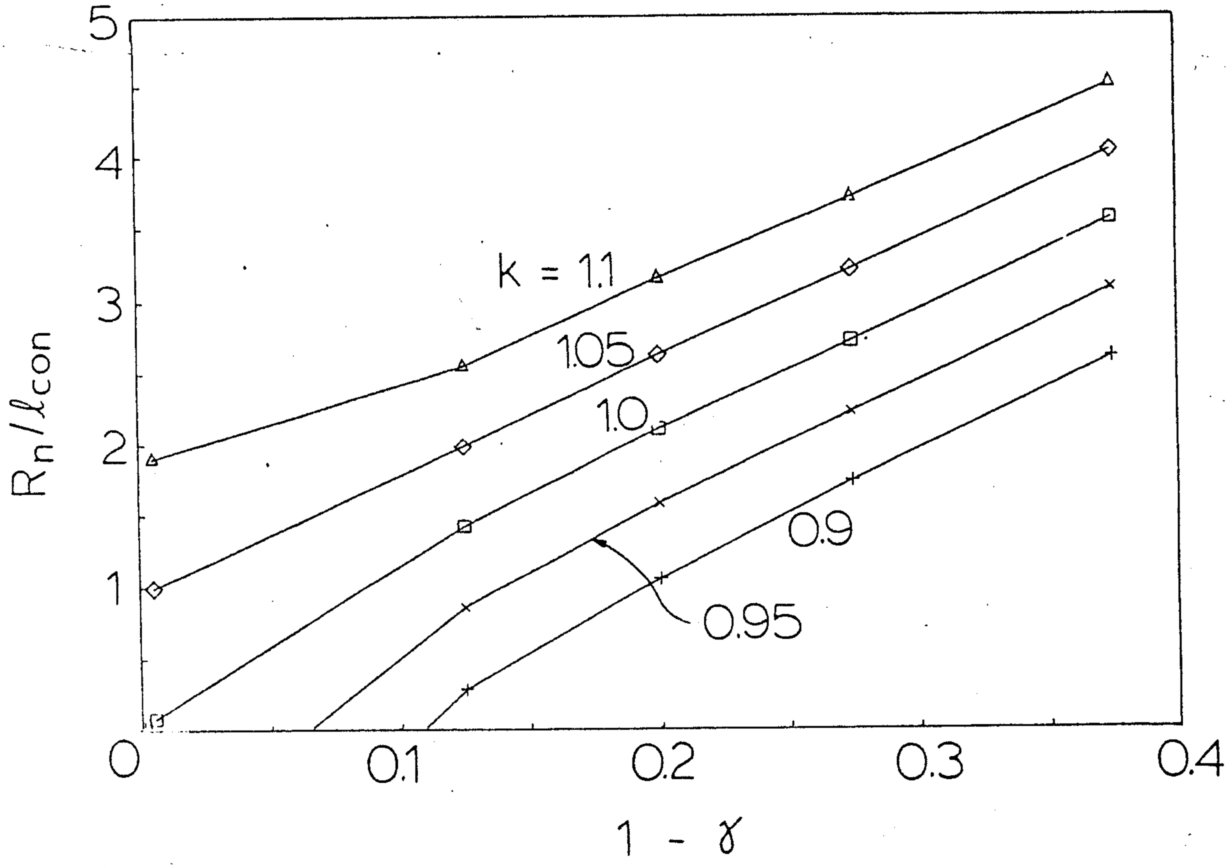

Figure 7.1.5 Ratio of Excess Neutron Generation Rate and ℓ_{cond} as Function of $1-\gamma$ for *AFCR* Type Devices with $P_{wall} = 2.2$ MW/m^2. k is the Effective Tritium Breeding Ratio (arbitrary units)

7.2 Scoping Studies of the *AFCR* Device

In this section, scoping study of the *AFCR* device is performed for a fixed value of $1-\gamma$. $1-\gamma = 0.2$ has been chosen for the illustrative case.

In order to keep the nuclear characteristics of the machine designs constant, the neutron wall loading of the first wall is kept constant in most of the parameterics scans performed in this chapter. The effect of changing the wall loading, however, is also analyzed. The radial build of the blanket/shield region is also varied to study the effect on the main machine parameters.

In order to maximize the burn pulse length, it is assumed that the OH transformer is double swung (the magnetic field in the OH transformer is reversed). The illustrative case has a burn pulse of 3600 s, that is, one hour of operation. The effect of different pulse lengths and the possibility of current drive is analyzed in section 7.4.

The plasma elongation has been chosen to be $\kappa = b/a = 1.5$ and the plasma safety factor $q = 2.5$ at the plasma edge and $q = 0.9 - 1.0$ at the plasma center. For these conditions, it is assumed that the value of the average toroidal beta (β) is determined by

$$\beta = \frac{0.25}{A}$$

The parameters of the equilibrium field system are calculated using the method described in chapter 3.

The distance between the toroidal field coil and the plasma in the midplane in the throat of the magnet, δ_i is assumed to be $\delta_i = 1.50$ m. This allows for 1.2

m of blanket/shielding in the inboard of the magnet, plus 0.10 m for first wall and 0.20 m for the plasma scrape-off region. On the outboard side of the plasma, the distance between the plasma and the toroidal field coil is the larger of 2.0 m or the value required to reduce the ripple in the magnetic field to acceptable levels. The larger distance allows for 1.5 m of blanket/shield modules located between the toroidal field coil and the first wall.

The assumptions in the parametric code are shown in Table 7.2.1. Table 7.2.2 shows the results of the parametric scan vs. aspect ratio for a fixed neutron wall loading of $P_{wall} = 2.2$ MW/m^2. In Table 7.2.2, I is the plasma current, P_f is the total fusion power, ℓ_{cond} is the length of the conductor of the TF coil times its current, E_{TF} is the stored energy in the EF coil, E_{EF} is the stored energy in the EF coils and MA_{EF} is the Ampere turns of the EF coils. $B_{TF,max}$ is the maximum field at the conductor. Table 7.2.2 shows that for a fixed neutron wall loading there is a maximum aspect ratio, above which the peak field at the conductor would be larger than the maximum allowable.

Figure 7.2.1 shows the plasma current I, the magnetic field on axis B, the plasma major radius R, the plasma performance P, and the fusion power P_f as functions of the aspect ratio. The plasma major radius remains approximately constant because of the constraint on the stresses in the throat of the magnet: as the aspect ratio increases, the throat cross sectional area increases sufficiently to balance the increased loads due to the increased magnetic field necessary to keep P_{wall} constant. Furthermore, the thickness of the blanket/shield region remains constant, and this is a significant driver in the size of the reactor. The fusion power, however, increases very significantly. This is due to the constraint of constant wall loading, coupled with the approximately constant major radius, resulting in increased wall area as the aspect ratio is decreased. The plasma current, the peak field at the conductor, the field on the axis and the energy stored in the toroidal field coil are also monotonically increasing with decreasing aspect ratio.

Figure 7.2.2 shows the parameters of the toroidal field coil E_{TF} (stored energy in the toroidal coil), and ℓ_{cond} (length of the conductor in the toroidal field coil times the conductor current) as functions of the aspect ratio. There is a minimum in both E_{TF} and ℓ_{cond} for $A \sim 4$. The minimum is fairly narrow.

Figure 7.2.3 shows the parameters of the equilibrium field system E_{EF} (stored energy), MA_{EF} (Ampere turns) and W_{EF} (weight of the coils of the EF system) as functions of the aspect ratio. The parameters of the vertical system also show a relatively narrow minimum for an aspect ratio of $A = 4$.

For the illustrative design, the case with aspect ratio $A \approx 4$ has been chosen. The optimum is narrow for the toroidal field and vertical field systems. The maximum field at the conductor implies a maximum aspect ratio allowable. Due to the large variation of fusion power with aspect ratio, the maximum allowed fusion power limits the minimum aspect ratio permissible. For the case of $P_{wall} = 2.2$ MW/m^2, these regions (for $P_f \leq 3000$ MW, $B_{TF,max} \leq 12-13$ T for Nb$_3$Sn and optimum toroidal and poloidal systems) are reduced to a region near $A = 4$.

In order to further study the effect of varying aspect ratio, Tables 7.2.3 and 7.2.4 show the results of the parametric study for different neutron wall loadings. Table 7.2.3 is for $P_{wall} = 4.4$ MW/m^2 and Table 7.2.4 is for $P_{wall} =$

1.1 MW/m^2. As for the case of Table 7.2.2 with $P_{wall} = 2.2$ MW/m^2, $A \sim 4$ minimizes the requirements on the toroidal and vertical field systems.

For $A = 4$, the maximum field at the conductor ranges from $B_{TF,max} = 11$ T for the case of low wall loading, to $B_{TF,max} = 12.7$ for the case with high wall loading. The fusion power, on the other hand, has varied from 1.1 GW for the case of low wall loading to ~ 10 GW for the high wall loading case. Therefore, although the minimum in the vertical and toroidal field systems occur at about the same value of aspect ratio ($A \sim 4$), the fusion power output varies widely with varying wall loading. $P_f \sim 3$ GW is reachable in the case of low wall loading with very low aspect ratios $A \sim 2.5$ while it is not accessible with high wall loadings.

The fusion power increases with increasing A in Table 7.2.3 (for $A > 6$) due to the fact that the major plasma radius is increasing. The increase in major radius more than balances the decrease in minor radius for $A > 6$, resulting in an increase in the first wall area and fusion power. For the high wall loading case, the minimum fusion power is about $P_f = 7.25$ GW for an aspect ratio of $A \sim 6$.

Table 7.3.5 shows the results of the parametrics code when the parameter $c_\beta = \beta \times A$ is varied while keeping the wall loading fixed. c_β is varied between 0.15 and 0.35, and corresponds to values of beta that are pessimistic ($\beta = 0.0375$ for $c_\beta = 0.15$) and optimistic ($\beta = 0.0875$ for $c_\beta = 0.35$) for an aspect ratio of $A = 4$. The scaling in the energy of the toroidal field system with c_β is

$$E_{TF} \sim c_\beta^{-2}$$

As c_β increases, that is, the β limits are more optimistic, the energy in the toroidal field system decreases but at a reduced rate ($\Delta E_{TF}/\Delta c_\beta \sim -1/c_\beta$). For the illustrative design in this study, it has been asumed that $c_\beta = 0.25$, corresponding to $\beta = 0.0625$ for $A = 4$.

Table 7.2.1

Assumptions for the Parametric Study

$1-\gamma$	0.2
q	2.5
b/a	1.5
T_e (keV)	35
τ_{burn} (s)	3600
Δ_{in} (m)	1.2
Δ_{out} (m)	1.5
σ_{TF} (MPa)	270
$\sigma_{buckpost}$ (MPa)	300
N_{coils}	16
$B_{OH,max}$ (T)	7

Table 7.2.2

Parametric Scan vs Aspect Ratio for $\sigma_{TF} = 270$ MPa and $P_{wall} = 2.2$ MW/m^2 (at $\gamma = 0.80$)

A	8.0	5.99	4.0	3.0	2.49
R (m)	11.4	9.82	9.6	11.2	14.2
a (m)	1.42	1.64	2.4	3.75	5.7
B (m)	11.4	9.51	7.05	5.46	4.48
I (MA)	8.32	11.1	18.7	31.1	47.6
P (m^{2}T^4)	32.7	38.3	55.6	86.8	132.
P_f (GW)	2.15	2.18	3.09	5.65	10.8
E_{TF} (GJ)	178.	111.	89.2	115.	186.
ℓ_{cond} (GA m)	60.7	37.8	26.5	28.1	36.7
$B_{TF,max}$ (T)	15.3	14.0	11.9	10.2	9.1
$W_{blanket}$ (Gg)	2.19	2.09	2.69	4.49	8.1
E_{OH} (GJ)	11.3	12.0	17.5	34.9	77.8
I_{OH} (MA)	108.	109.	125.	160.	213.
E_{EF} (GJ)	41.5	18.3	14.2	22.3	43.7
W_{EF} (Gg)	2.51	1.58	1.4	1.9	2.95
MA_{EF} (MA turns)	59.7	42.5	36.4	40.9	50.1

Table 7.2.3

Parametric Scan vs Aspect Ratio for $\sigma_{TF} = 270$ MPa and $P_{wall} = 4.4$ MW/m^2 (at $\gamma = 0.80$)

A	7.99	6.0	4.0	3.0	2.5
R (m)	15.6	12.7	12.0	14.2	18.6
a (m)	1.95	2.12	3.0	4.73	7.43
B (m)	12.5	10.6	7.91	6.11	5.0
I (MA)	12.6	15.9	26.3	43.9	69.0
P (m^{2}T^4)	89.4	98.7	138.	217.	345.
P_f (GW)	8.07	7.26	9.56	17.8	37.1
E_{TF} (GJ)	466.	260.	190.	255.	464.
ℓ_{cond} (GA m)	126.	70.6	46.8	50.2	70.1
$B_{TF,max}$ (T)	15.9	14.8	12.7	10.9	9.6
$W_{blanket}$ (Gg)	3.69	3.22	3.97	6.85	13.4
E_{OH} (GJ)	21.0	21.8	33.0	71.6	182.
I_{OH} (MA)	132.	131.	149.	195.	270.
E_{EF} (GJ)	89.9	39.2	29.1	48.0	106.
W_{EF} (Gg)	4.15	2.55	2.18	3.04	5.11
MA_{EF} (MA turns)	71.4	52.7	46.3	53.5	68.3

Table 7.2.4

Parametric Scan vs Aspect Ratio for $\sigma_{TF} = 270$ MPa and $P_{wall} = 1.1$ MW/m^2 (at $\gamma = 0.80$)

A	8.02	6.0	4.0	3.0	2.5
R (m)	8.9	7.98	8.0	9.32	11.5
a (m)	1.11	1.33	2.0	3.11	4.6
B (m)	10.2	8.42	6.2	4.81	4.0
I (MA)	5.83	7.94	13.7	22.8	34.2
P (m^{2}T^4)	13.0	15.4	23.1	36.0	54.2
P_f (GW)	0.668	0.713	1.07	1.94	3.61
E_{TF} (GJ)	80.2	55.2	46.6	57.5	86.9
ℓ_{cond} (GA m)	33.3	22.0	16.1	16.9	21.3
$B_{TF,max}$ (T)	14.4	13.0	11.0	9.5	8.5
$W_{blanket}$ (Gg)	1.48	1.49	1.97	3.21	5.46
E_{OH} (GJ)	7.27	7.57	10.4	19.2	38.9
I_{OH} (MA)	92.7	94.8	109.	137.	177.
E_{EF} (GJ)	22.3	9.82	7.67	11.5	20.8
W_{EF} (Gg)	1.68	1.08	0.965	1.26	1.87
MA_{EF} (MA turns)	51.5	35.2	29.3	32.0	38.3

Table 7.2.5

Parametric Scan vs c_β for $\sigma_{TF} = 270$ MPa and $P_{wall} = 2.2\ \mathrm{MW/m^2}$ (at $\gamma = 0.80$)

c_β	0.15	0.20	0.25	0.30	0.35
R (m)	13.3	10.9	9.6	8.74	8.16
a (m)	3.32	2.73	2.4	2.19	2.04
A	4.0	3.99	4.0	3.99	4.0
B (m)	8.39	7.63	7.05	6.6	6.21
I (MA)	28.3	22.2	18.7	16.5	14.9
P ($\mathrm{m^2T^4}$)	76.8	63.4	55.6	51.4	47.4
P_f (GW)	5.9	4.0	3.09	2.6	2.24
E_{TF} (GJ)	278.	139.	89.2	63.9	48.7
ℓ_{cond} (GA m)	60.8	37.2	26.5	20.5	16.9
$B_{TF,max}$ (T)	13.1	12.5	11.9	11.4	11.0
$W_{blanket}$ (Gg)	4.76	3.36	2.69	2.29	2.04
E_{OH} (GJ)	41.2	24.5	17.5	13.8	11.5
I_{OH} (MA)	163.	139.	125.	117.	110.
(T)	-9.03	-8.57	-8.15	-7.87	-7.54
E_{EF} (GJ)	31.8	19.2	14.2	11.5	9.63
W_{EF} (Gg)	2.38	1.71	1.4	1.22	1.09
MA_{EF} (MA turns)	46.4	40.0	36.4	34.0	32.0

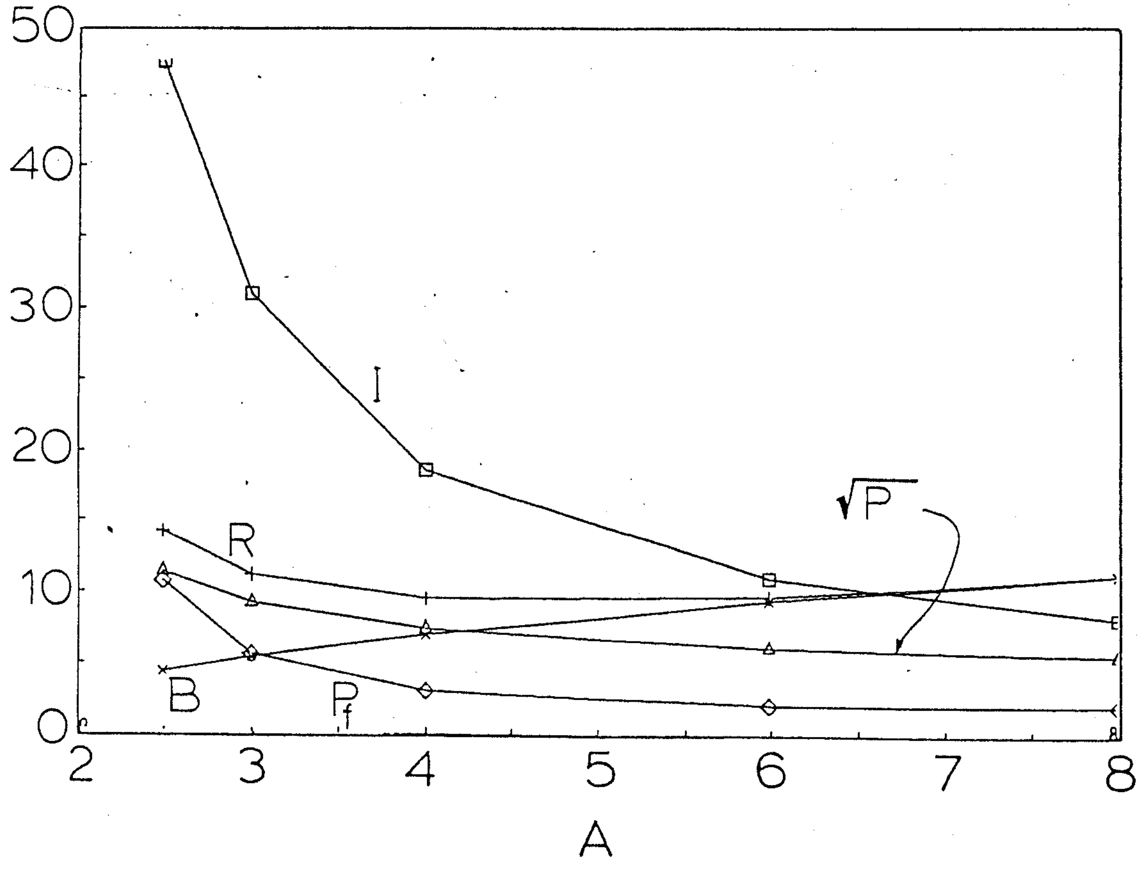

Figure 7.2.1 Values of I, R, B, $\sqrt{P} = \beta a B^2$ as Functions of Aspect Ratio for *AFCR* Type Devices with $P_{wall} = 2.2$ MW/m^2 ($\gamma = 0.80$).

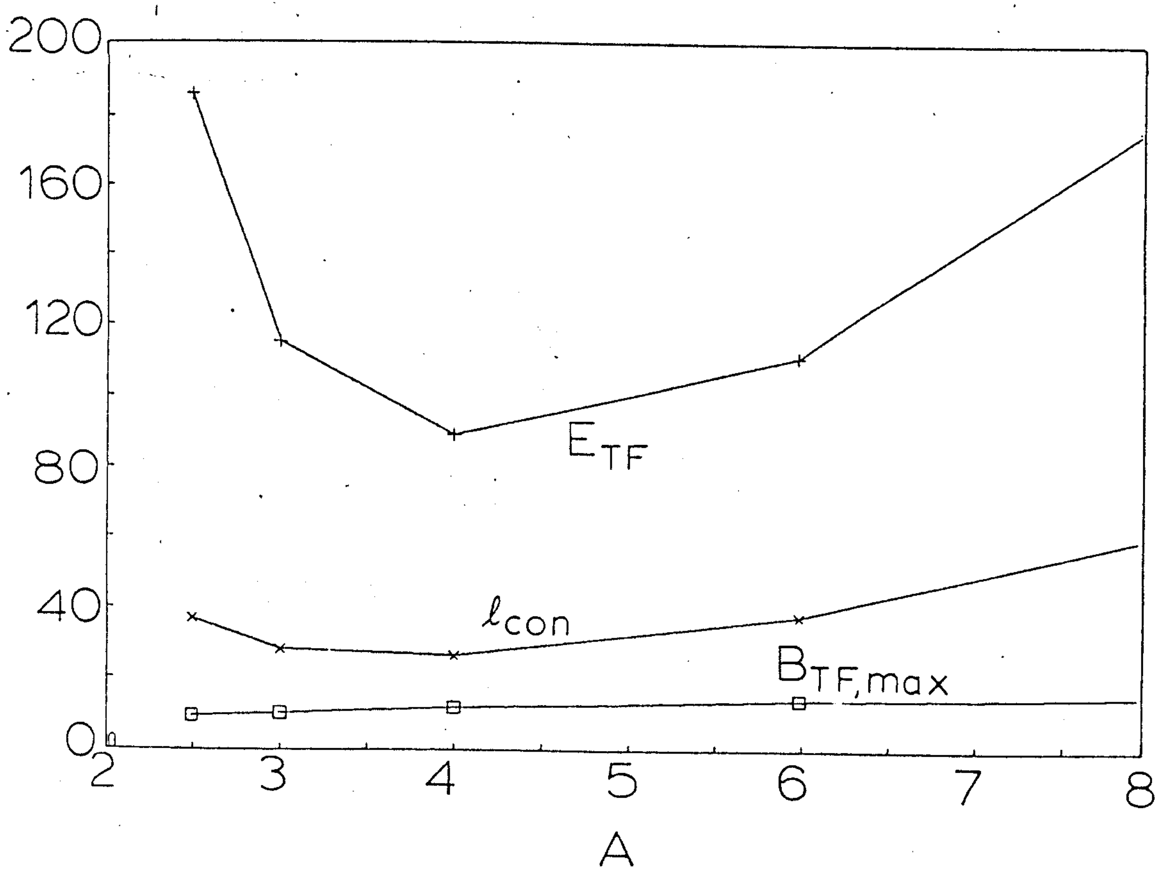

Figure 7.2.2 Values of E_{TF}, ℓ_{cond} and $B_{TF,max}$ as Functions of Aspect Ratio for *AFCR* Type Devices with $P_{wall} = 2.2$ MW/m^2 ($\gamma = 0.80$).

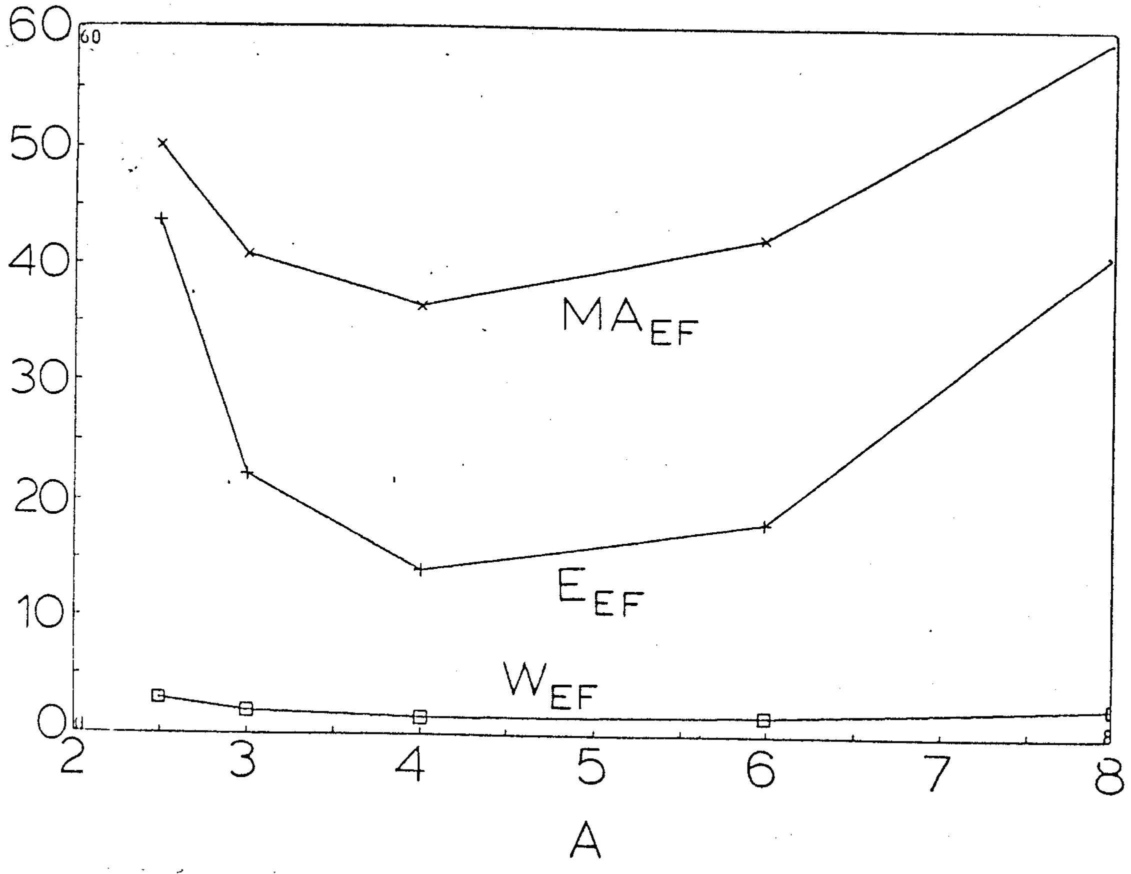

Figure 7.2.3 Values of W_{EF}, E_{EF} and MA_{EF} as Functions of Aspect Ratio for *AFCR* Type Devices with $P_{wall} = 2.2$ MW/m^2 ($\gamma = 0.80$).

7.3 Optimization of the Toroidal Field Coil

In this section, the effect of varying several parameters of the toroidal field system are analyzed. The parameters in Table 7.2.1 are used in the analysis. The aspect ratio is assumed to be $A = 4$.

Table 7.3.1 shows results of the parametric analysis as the stresses in the toroidal field coil, σ_{TF}, are increased. The stresses are varied from 200 MPa to 350 MPa. Increasing the stresses in the throat of the magnet from 200 to 350 MPa results in a reduction of the plasma major radius of 0.60 m, or about 5%. The main machine parameters do not vary strongly with σ_{TF}, in contrast to the machine with resistive magnets, where the machine size was strongly affected by the stresses in the throat of the magnet (see Chapter 4). It is chosen that $\sigma_{TF} = 270$ MPa.

In the illustrative design discussed in chapter 8 it is assumed that there is a bucking post and that the coils are separated in the throat of the magnet. The reason for this choice is discussed in the next chapter and has to do with maintenance requirements. Table 7.3.2 shows the results from the parametric analysis when the stresses in the bucking post used to carry the centering loads of the TF magnet are varied. The stresses in the bucking post are varied from 150 to 1000 MPa. This last case simulates the absence of a bucking post. In this case, the centering forces would be carried by the legs in the throat of the magnet through wedging, or by the OH transformer directly. The presence and size of the bucking post has a significant consequences on the machine. The plasma major radius increases from 8.1 to 12.5 in the case of no bucking post to the case of one with a bucking post with $\sigma_{TF} = 150$ MPa. Significant increases are also observed in the equilibrium field and toroidal field systems. $\sigma_{buckpost}$ is chosen to be 300 MPa.

Table 7.3.3 shows the results of the parametric code when the thickness of the inboard blanket/shield is varied from $\Delta_{in} = 0.9$ m to $\Delta_{in} = 1.5$ m. The major radius of the machine R increases by approximately 0.8 m for every 0.30 m increments in Δ_{in}. The *AFCR* device is not strongly dependent on this distance (in contrast of the *AFTR* design) due to the large section used in the throat region by the OH transformer. For the illustrative design case, it has been assumed that $\Delta_{in} = 1.2$ m.

Table 7.3.4 shows the main parameters of the *AFCR* device as the ripple requirements on the plasma axis are varied. The main effect of decreasing the allowable ripple is that the outer leg of the toroidal field magnet moves away from the plasma. This has the effect of increasing the equilibrium and toroidal field system requirements. However, removing the outer leg of the magnet away from the plasma increases accessibility for maintenance. For $\delta_o = 0.1\%$, the locations of the outer leg of the coils is determined by the blanket requirements. This ripple requirement has been chosen for the illustrative case and for the rest of the scoping study.

Finally, Table 7.3.5 shows the main machine parameters as the number of coils is varied for fixed ripple on axis. For $N_{coils} = 16$ the outer leg of the coil is determined by the blanket/shield requirements. $N_{coils} = 12$ results in a significant increase in the amount of conductor required for the toroidal field coil, plus increases in both the energies in both the toroidal field system and the vertical field system. The latter effect due to the change in the location of the main equilibrium field coil as the outer leg of the magnet is pushed away from the plasma. A lower number of coils facilitates maintenance operations, at a price of increased coil size. For the study performed here, it is assumed that $N_{coils} = 16$.

Table 7.3.1

Parametric Scan vs σ_{TF} for

$P_{wall} = 2.2$ MW/m^2 (at $\gamma = 0.80$)

σ_{TF} (MPa)	200.	270.	350.
R (m)	9.96	9.6	9.35
a (m)	2.49	2.4	2.34
A	4.0	4.0	4.0
B (m)	7.0	7.05	7.1
I (MA)	19.3	18.7	18.4
P (m^{2}T^4)	58.2	55.6	54.5
P_f (GW)	3.35	3.09	2.95
E_{TF} (GJ)	95.4	89.2	85.5
ℓ_{cond} (GA m)	28.3	26.6	25.3
$B_{TF,max}$ (T)	11.7	11.9	12.0
$W_{blanket}$ (Gg)	2.87	2.69	2.57
E_{OH} (GJ)	18.7	17.5	16.7
I_{OH} (MA)	128.	125.	124.
E_{EF} (GJ)	14.9	14.2	13.8
W_{EF} (Gg)	1.45	1.4	1.37
MA_{EF} (MA turns)	36.5	36.4	36.5

Table 7.3.2

Parametric Scan vs $\sigma_{buckpost}$ for $\sigma_{TF} = 270$ MPa and $P_{wall} = 2.2$ MW/m^2 (at $\gamma = 0.80$)

$\sigma_{buckpost}$ (MPa)	150.	300.	450.	1000.
R (m)	12.5	9.6	8.83	8.14
a (m)	3.12	2.4	2.21	2.03
A	4.01	4.0	4.0	4.01
B (m)	6.6	7.05	7.2	7.34
I (MA)	22.8	18.7	17.6	16.5
P (m^{2}T^4)	71.9	55.6	51.4	46.5
P_f (GW)	5.2	3.09	2.63	2.19
E_{TF} (GJ)	147.	89.2	77.7	67.5
ℓ_{cond} (GA m)	42.4	26.5	22.9	19.8
$B_{TF,max}$ (T)	10.5	11.9	12.4	13.0
$W_{blanket}$ (Gg)	4.27	2.69	2.33	2.02
E_{OH} (GJ)	28.9	17.5	15.2	13.3
I_{OH} (MA)	147.	125.	120.	114.
E_{EF} (GJ)	20.8	14.2	12.9	11.7
W_{EF} (Gg)	1.84	1.4	1.31	1.22
MA_{EF} (MA turns)	37.1	36.4	36.6	36.8

Table 7.3.3

Parametric Scan vs Inboard Blanket/Shield Thickness Δ_{in}
for σ_{TF} = 270 MPa and
P_{wall} = 2.2 MW/m^2 (at γ = 0.80)

Δ_{in} (m)	0.9	1.2	1.5
R (m)	8.7	9.6	10.4
a (m)	2.18	2.4	2.6
A	3.99	4.0	4.0
B (m)	7.21	7.05	6.9
I (MA)	17.4	18.7	19.8
P (m^{2}T^4)	50.4	55.6	59.7
P_f (GW)	2.54	3.09	3.6
E_{TF} (GJ)	71.2	89.2	108.
ℓ_{cond} (GA m)	22.4	26.5	30.6
$B_{TF,max}$ (T)	11.8	11.9	12.0
$W_{blanket}$ (Gg)	2.19	2.69	3.21
E_{OH} (GJ)	14.6	17.5	20.7
I_{OH} (MA)	117.	125.	133.
E_{EF} (GJ)	12.4	14.2	15.8
W_{EF} (Gg)	1.28	1.4	1.52
MA_{EF} (MA turns)	36.1	36.4	36.7

Table 7.3.4

Parametric Scan vs Ripple Requirement on Axis δ_o for $\sigma_{TF} = 270$ MPa and $P_{wall} = 2.2$ MW/m^2 (at $\gamma = 0.80$)

δ_o	.01%	.05%	.1%
R (m)	9.77	9.65	9.6
a (m)	2.44	2.41	2.4
A	4.0	4.0	4.0
B (m)	7.02	7.05	7.05
I (MA)	18.9	18.8	18.7
P (m^{2}T^4)	56.4	55.9	55.6
P_f (GW)	3.19	3.12	3.09
E_{TF} (GJ)	106.	91.8	89.2
ℓ_{cond} (GA m)	31.4	27.9	26.5
$B_{TF,max}$ (T)	11.8	11.8	11.9
$W_{blanket}$ (Gg)	2.77	2.71	2.69
E_{OH} (GJ)	18.1	17.7	17.5
I_{OH} (MA)	127.	126.	125.
E_{EF} (GJ)	17.3	14.6	14.2
W_{EF} (Gg)	1.59	1.43	1.4
MA_{EF} (MA turns)	38.0	36.6	36.4

Table 7.3.5

Parametric Scan vs Number of Coils N_{coils} for $\sigma_{TF} = 270$ MPa and $P_{wall} = 2.2$ MW/m^2 (at $\gamma = 0.80$)

N_{coils}	12	16
R (m)	9.78	9.6
a (m)	2.44	2.4
A	4.01	4.0
B (m)	7.01	7.05
I (MA)	18.9	18.7
P (m^{2}T^4)	55.9	55.6
P_f (GW)	3.17	3.09
E_{TF} (GJ)	107.	89.2
ℓ_{cond} (GA m)	31.6	26.5
$B_{TF,max}$ (T)	11.8	11.9
$W_{blanket}$ (Gg)	2.77	2.69
E_{OH} (GJ)	18.1	17.5
I_{OH} (MA)	127.	125.
E_{EF} (GJ)	17.4	14.2
W_{EF} (Gg)	1.59	1.4
MA_{EF} (MA turns)	38.0	36.4

7.4 Pulse Length Tradeoffs

In this section the pulse length of the plasma is varied. The implications for the design of the *AFCR* device and for the requirement for the OH transformer are analyzed.

As discussed previously, the plasma temperature that optimizes the machine design results from a tradeoff between the fusion power density (which is optimized for a temperature of $T_i \sim 20$ keV for DT and for a wide range of temperatures for DD-DT), the requirement for the ohmic transformer (the resistive volt seconds required for the plasma burn decrease with increasing temperature), and the ignition criteria. The ignition criteria for plasmas operating at these temperature and of these sizes cannot be estimated with any degree of confidence. Therefore, in this section, and through most of this report, the important parameters have been wall loading, fusion power density, and, in this section, resistive voltage requirements.

Table 7.4.1 shows the results of the parametric code for varying peak fields in the ohmic heating solenoid (the stresses of the solenoid are kept constant). The peak field is varied from $B_{OH,max} = 7$ to $B_{OH,max} = 11$ T. The machine decreases with increasing $B_{OH,max}$ at the expense of increased energy stored and increased current in the ohmic heating transformer. The illustrative case has a peak field of $B_{OH,max} = 7$ T, as would be the case if NbTi were used for this transformer. The gains in size reduction probably do not warrant going to a higher field ohmic transformer. This conclusion changes if the pulse length is increased beyond the $\tau_{burn} = 3600$ s assumed in Table 7.4.1.

Table 7.4.2 shows the results of the parametric code as the pulse length is varied. The first entry in this Table corresponds to the case of current driven operation, both for the inductive part and for the burn (that is, there is no OH transformer). The other entries refer to the case with an ohmic transformer providing the inductive and resistive fluxes. The last entry in Table 7.4.2 corresponds to a pulse length of half a day (43200 s).

The absense of an ohmic solenoid reduces the size of the machine substantially. Once the solenoid is there to provide the required flux, not much effect on the machine size is experienced as the pulse length is increased from 0 s to 10800 s (that is, 3 hours). Further increases in the burn pulse result in significant increases in the size of the machine.

As a conclusion, it is possible to provide for long pulse lengths (in the order of hours) in reactor devices by slightly increasing the reactor size to accomodate a larger ohmic heating solenoid.

Table 7.4.1

Parametric Scan vs Peak Field in the OH Transformer $B_{OH,max}$ for σ_{TF} = 270 MPa and P_{wall} = 2.2 MW/m^2 (at $\gamma = 0.80$)

$B_{OH,max}$ (T)	7.0	9.0	11.0
A	4.0	4.0	4.0
R (m)	9.6	9.16	8.93
a (m)	2.4	2.29	2.23
B (m)	7.05	7.13	7.19
I (MA)	18.7	18.1	17.7
P (m^{2}T^4)	55.6	52.9	51.8
P_f (GW)	3.09	2.81	2.68
E_{TF} (GJ)	89.2	82.3	79.1
ℓ_{cond} (GA m)	26.5	24.4	23.4
$B_{TF,max}$ (T)	11.9	12.1	12.3
$W_{blanket}$ (Gg)	2.69	2.48	2.37
E_{OH} (GJ)	17.5	20.7	24.1
I_{OH} (MA)	125.	157.	189.
E_{EF} (GJ)	14.2	13.4	13.1
W_{EF} (Gg)	1.4	1.35	1.32
MA_{EF} (MA turns)	36.4	36.5	36.6

Table 7.4.2

Parametric Scan vs Burn Pulse Length τ_{burn}
for $\sigma_{TF} = 270$ MPa and
$P_{wall} = 2.2$ MW/m^2 (at $\gamma = 0.80$)

τ_{burn} (s)	No OH	0	3600	10800	43200
R (m)	6.84	8.71	9.6	10.9	14.4
a (m)	1.71	2.18	2.4	2.72	3.61
A	4.0	4.0	4.0	4.0	4.0
B (m)	7.7	7.23	7.05	6.83	6.36
I (MA)	14.6	17.5	18.7	20.6	25.4
P (m^{2}T^4)	40.2	50.8	55.6	62.9	83.3
P_f (GW)	1.59	2.56	3.09	3.96	6.96
E_{TF} (GJ)	52.0	76.0	89.2	111.	199.
ℓ_{cond} (GA m)	14.6	22.4	26.6	33.1	54.6
$B_{TF,max}$ (T)	14.5	12.5	11.9	11.1	9.8
$W_{blanket}$ (Gg)	1.52	2.28	2.69	3.34	5.53
E_{OH} (GJ)	0.473	10.0	17.5	32.5	102.
I_{OH} (MA)	105.	119.	125.	135.	161.
E_{EF} (GJ)	10.2	12.8	14.2	16.6	26.9
W_{EF} (Gg)	1.1	1.3	1.4	1.57	2.19
MA_{EF} (MA turns)	38.5	36.7	36.4	36.4	38.3

8 ILLUSTRATIVE DESIGN OF *AFCR*

In this chapter, the illustrative design of an *AFCR* device is described.

The purpose of an *AFCR* type device is to be a net electricity producer self sufficient in tritium production. It would do this with a blanket optimized for purposes different from only tritium breeding. The relaxation of the tritium breeding ratio could result in

- blankets that are optimized for safety
- blankets optimized for low activity
- removal of the need of breeding tritium in the inboard region of the reactor
- optimization of the first wall that would result in decreased breeding (such as locating thick armor for disruption protection of the first wall).

Alternatively, the *AFCR* device could be used for breeding fissile material or additional tritium to be used in other fusion reactors that are not tritium self-sufficient.

Section 8.1 decribes the illustrative device.

Section 8.2 describes some of the most salient engineering features of the illustrative design.

8.1 Illustrative Design

Table 8.1.1 lists the main machine parameters for the illustrative *AFCR* device for the full performance operation.

Figure 8.1.1 shows a cross sectional view of the *AFCR* device. The poloidal field coils are located outside the toroidal field coils. The plasma major radius is 9.6 m. The bucking cylinder supports the toroidal field coils against the inward force due to the toroidal field.

Figure 8.1.2 shows a top view of the reactor. There are 16 toroidal field coils. Each toroidal field coil is removable to facilitate remote maintenance. It is not necessary to warm up any of the structure in order to remove a toroidal field coil.

The machine operates with $1-\gamma = 0.2$ and a wall loading $P_{wall} = 2.2$ MW/m^2. The peak ion temperature is 45 keV, while the electron temperature is $T_e = 35$ keV. The high ion and electron temperature are needed not because of the use of DD-DT fuels (lower temperatures result in slighty increased specific fusion power density P_f/β^2B^4), but are used in order to save in the resistive volt-seconds in the OH transformer.

Table 8.1.2 shows the performance of the illustrative design as a function of $1-\gamma$. Very high wall loadings would result if the machine were operated with DT fuels ($1-\gamma \simeq 0$). The advantages of DD-DT are best exploited in the cases where the wall loading in DT operation is beyond what the wall can tolerate. Although the machine can be underrated (reduced field and or reduced β), a machine that has been optimized for DT operation with these constraints would be significantly smaller.

Table 8.1.1

AFCR -TYPE DEVICE MAIN PARAMETERS

	PLASMA
MAJOR RADIUS (m)	9.6
MINOR RADIUS (m)	2.4
PULSE LENGTH (s)	3600
SCRAPE-OFF LAYER (m)	0.20
PLASMA ELONGATION (m)	1.5
PLASMA TRIANGULARITY	0.2
ASPECT RATIO	4.0
PEAK ION TEMPERATURE (keV)	35
$1 - \gamma$	0.2
SAFETY FACTOR	2.5
$1 - \gamma$	0.20
D-T ION DENSITY (m^{-3})	1.2×10^{20}
PLASMA CURRENT (MA)	18.7
EFFECTIVE CHARGE	1.2
PEAK-TO-AVERAGE RIPPLE AT PLASMA AXIS(%)	0.08
TOTAL BETA (%)	6.25
FIELD ON AXIS (T)	7.05
D-T FUSION POWER (MW)	3090
NEUTRON WALL LOADING (MW/m^2)	2.2
	BLANKET/SHIELD
INBOARD BLANKET THICKNESS (m)	1.2
OUTBOARD BLANKET/SHIELD THICKNESS (m)	1.5

AFCR -TYPE DEVICE PARAMETERS (continued)

	TF COIL
NUMBER OF TF COILS	16
MAXIMUM TF FIELD (T)	11.9
WINDING CURRENT DENSITY (MA/m^2)	20
TF STORED ENERGY (GJ)	89.2
TF CONDUCTOR LENGTH (MA m)	26500
TOTAL CURRENT (MA)	340
CURRENT (kA)	520
	PF COILS
EF COIL A-TURNS (MAT)	36.4
V-s FROM EF COILS (Wb)	120
V-s FROM OH COILS (Wb)	480
TOTAL V-s FROM PF (Wb)	600
FIELD (OH SOLENOID) (T)	7
CURRENT RISE TIME (s)	4
CURRENT DENSITY (EF COILS) (MA/m^2)	15
PEAK ENERGY (EF COIL) (GJ)	14.2
PEAK ENERGY (OH COIL) (GJ)	17.5

TABLE 8.1.2

DD-DT TRADEOFFS FOR ADVANCED FUEL COMMERCIAL REACTOR (AFCR) DEVICE

$1-\gamma$	Fusion Power (GW)	Neutral Wall Loading (MW/M^2)	Q_p
0.0 (DT)	40.7	29.1	∞
0.10	5.9	4.3	∞
0.20	3.1	2.2	∞
0.35	1.8	1.3	10.0
0.75	0.72	0.5	2.0
1 (SCD)	0.50	0.36	1.25

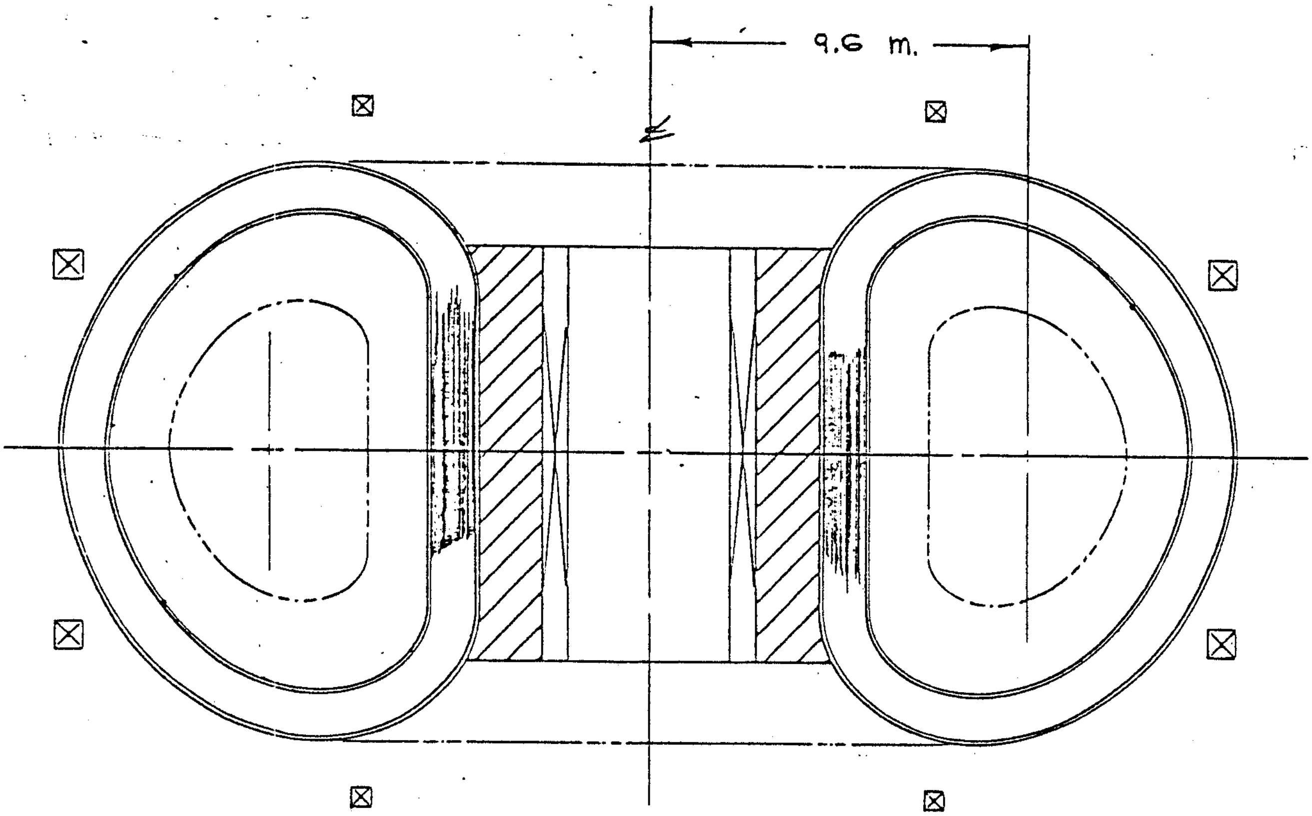

Figure 8.1.1 Cross Sectional View of *AFCR*

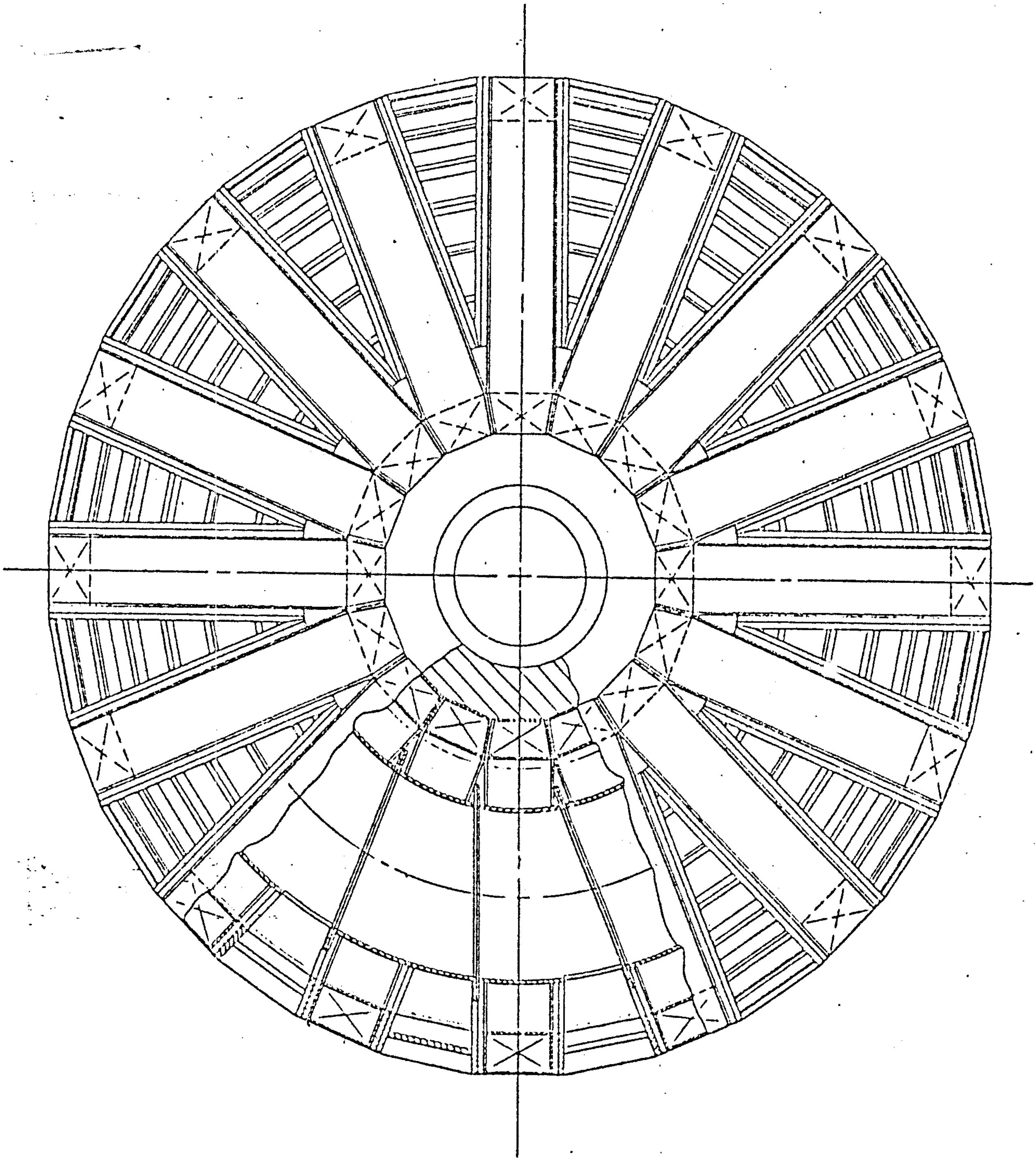

Figure 8.1.2 Top View of *AFCR*

8.2 Reactor Design Principles

The design of the superconducting machine is dominated by the support of the TF coils against the overturning moment of the vertical field and against the centering force, in a manner compatible with modular disassembly of the system.

The key principle for the solution of these problems and other slightly less difficult structural constraints is the use of a compression member of low thermal conductivity between the low temperature region of the coils and room the temperature structure.

Such a material is G-10, a composite of epoxy resin and glass fiber. It can support 200 MPa in compression with adequate margin and has low thermal conductivity integrals, especially at low temperatures. The thermal conductivity integral is $\int_{\theta_1}^{\theta_2} k d\theta$ and for G - 10 it has the values, 0.49 W m^{-1} in the temperature range 20 K to 4.2K, 2.37 (77K to 20K) and 18.4 (300K to 77K).

Figure 8.2.1 shows the principal use of G-10 spaces between heat sinks refrigerated to 20K and 77K in the vacuum space surrounding the TF coil. The plates are 1/2" thick and of sufficient area to limit compressive stresses in the G-10 to 200 MPa. In Table 8.2.1 are compiled the characteristics of the G-10 constraints for the centering and overturning forces.

Table 8.2.1

Effect of G-10 Supports in Thermal Load of TF Coil

	Centering Forces	Overturning Moments
Total Force (GN)	14	—
Total Moment (GN m)	—	17
Required Area (m^2)	71	45
Heat loads		
to 4.2 K (kW)	1.7	2.7
to 20 K (kW)	13.8	21.6
to 77 K (kW)	105	167
Total Room-Temperature Heat Load (MW) †	3.7	5.8

† Assuming 20% of Carnot efficiency.

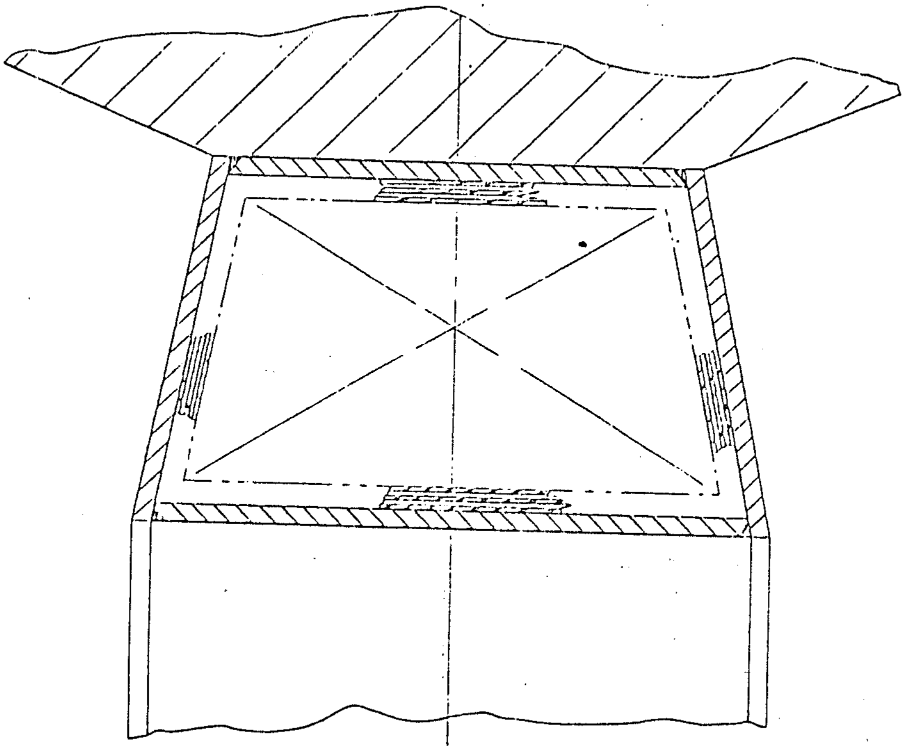

Figure 8.2.1 Cross Sectional View of the Toroidal Field Coil. G-10 Struts are Shown.

8.3 Modularity and Maintenance

The use of G-10 compressive supports obviates the need for cold structure between the TF coils. This is the feature which allows the unfettered removal and replacement of a module consisting of a TF coil, blanket, first wall and vacuum flanges. In order that the matching faces of a vacuum flange should separate freely the line of withdrawal of a module must make a positive angle with the plane of the flange as shown in Figure 8.3.1. Furthermore, no part of a module must interfere with an adjoining flange face as it moves along the line of withdrawal. These conditions limit the positioning of the flanges but nevertheless allow them to be located between an access port and a TF coil so that large ports can be accommodated between TF coils.

The proposed vacuum flange design is shown schematically in Figure 8.3.2. It is a weldless flange, requiring essentially no preparation either for disassembly or reassembly. The principle of the flange is the use of a set of concentric galleries, separately pumped and sealed from adjacent sections. At the inside of the flange in high radiation regions the seals would be metallic; at the outside the seals could be of silicone or other radiation resistant flexible polymer. An important feature of the flange is the use of a gallery close to the outside as a controlled leak of low Z gas such as helium or deuterium. This ensures that any leak inwards past the galleries is of a benign species and not oxygen, nitrogen or other high Z impurity.

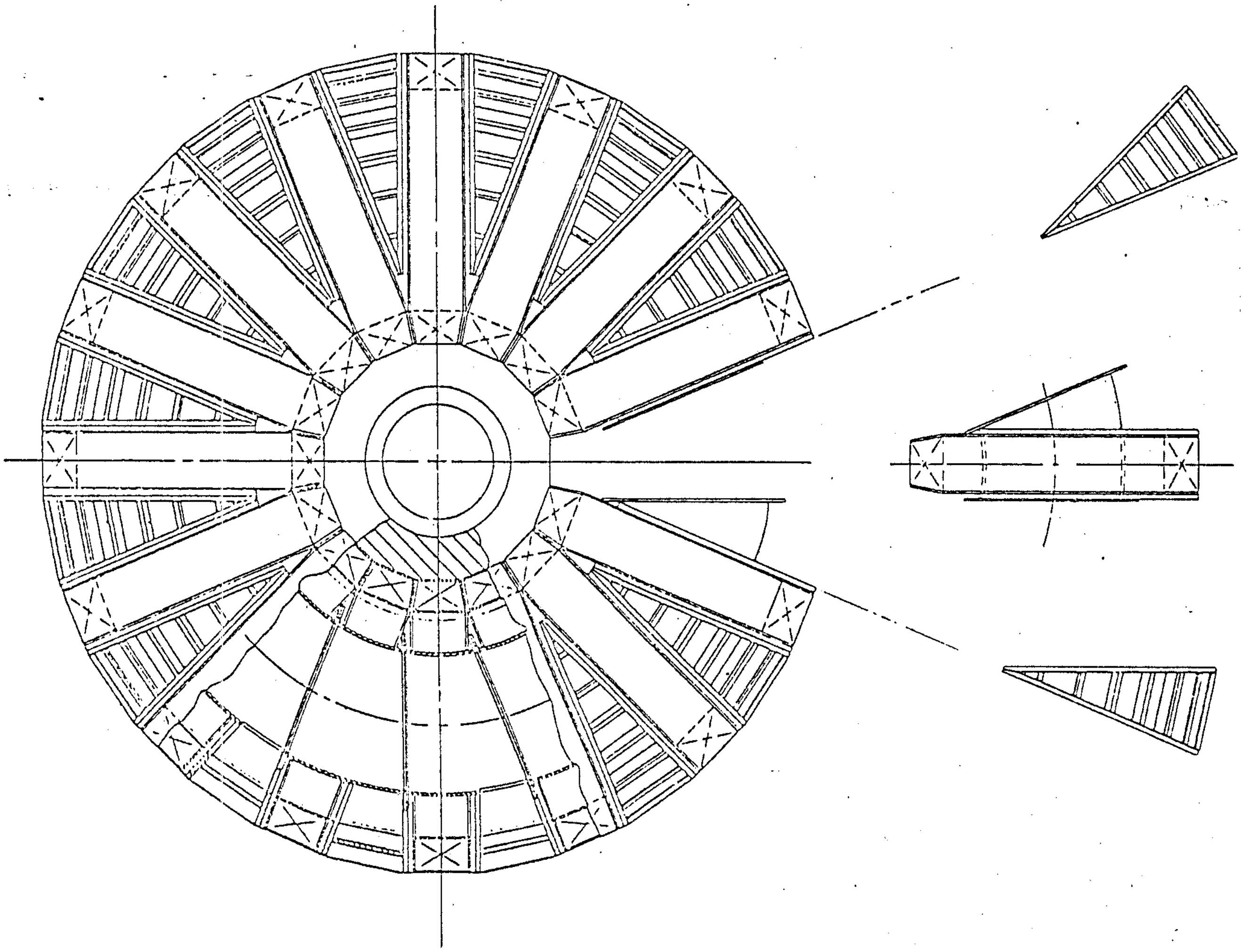

Figure 8.3.1 Modularization Scheme for *AFCR* . Toroidal Field Coil and Shear Pannels of one Module Have Been Removed.

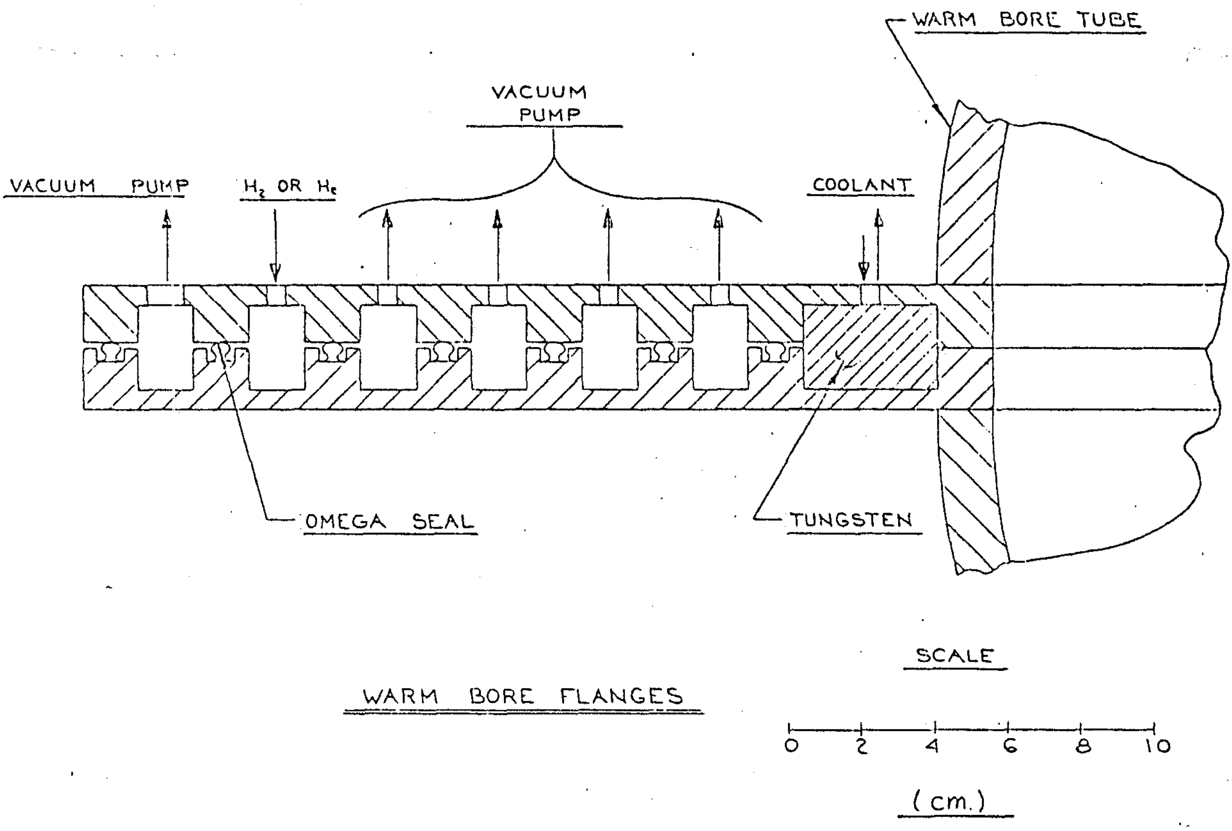

Figure 8.3.2 Scheme for Vacuum Seal.